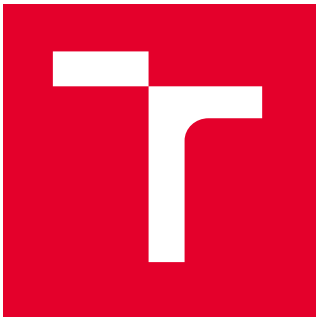

BRNO UNIVERSITY OF TECHNOLOGY

VYSOKÉ UČENÍ TECHNICKÉ V BRNĚ

FACULTY OF MECHANICAL ENGINEERING

FAKULTA STROJNÍHO INŽENÝRSTVÍ

INSTITUTE OF PHYSICAL ENGINEERING

ÚSTAV FYZIKÁLNÍHO INŽENÝRSTVÍ

DEFECT LOCALIZATION AND ANALYSIS IN GAN

LOKALIZACE A ANALÝZA DEFEKTŮ V GAN

MASTER'S THESIS

DIPLOMOVÁ PRÁCE

AUTHOR — **Bc. Richard Gazdík**

AUTOR PRÁCE

SUPERVISOR — **Ing. Petr Bábor, Ph.D.**

VEDOUCÍ PRÁCE

BRNO 2024

BRNO UNIVERSITY OF TECHNOLOGY
FACULTY OF MECHANICAL ENGINEERING

Assignment Master's Thesis

Institut:	Institute of Physical Engineering
Student:	**Bc. Richard Gazdík**
Degree programm:	Physical Engineering and Nanotechnology
Branch:	no specialisation
Supervisor:	**Ing. Petr Bábor, Ph.D.**
Academic year:	2023/24

As provided for by the Act No. 111/98 Coll. on higher education institutions and the BUT Study and Examination Regulations, the director of the Institute hereby assigns the following topic of Master's Thesis:

Defect localization and analysis in GaN

Brief Description:

Materials used in the semiconductor industry require not only high purity but also a low concentration of crystallographic defects. Currently, gallium nitride (GaN) is widely used for the fabrication of high performance chips. GaN production technology does not yet achieve comparable quality in terms of these defects as is the case for silicon crystal production. GaN manufacturers want to minimize the amount of defects to achieve higher performance GaN chips. Minimising the number of defects requires the development of methods and procedures to enable the localisation and subsequent analysis of these defects. The aim of this thesis will be to localize the defects using the ECCI (Electron channelling contrast imaging) method, extract these defects using a focused ion beam and, in collaboration with CEITEC operators, perform their analysis in a high resolution transmission electron microscope.

Master's Thesis goals:

1. Localize defects on GaN layers using ECCI method.
2. Extract defects using a focused ion beam (lamella).
3. In collaboration with CEITEC operators, perform transmission electron microscope analysis.

Recommended bibliography:

HAN, Han. et al. Crystalline defect analysis in epitaxial Si0.7Ge0.3 layer using site-specific ECCI-STEM. Micron [online]. 2021, 150. ISSN 0968-4328 Available at: https://doi.org/10.1016/j.micron.2021.103123

SIMKIN, B. A., M. A. CRIMP. An experimentally convenient configuration for electron channeling contrast imaging. Ultramicroscopy [online]. 1999, 77(1-2), p. 65-75. ISSN 0304-3991 Available at: https://doi.org/10.1016/S0304-3991(99)00009-1

KAMALADASA, Ranga J., Yoosuf N. PICARD. Basic Principles and Application of Electron Channeling in a Scanning Electron Microscope for Dislocation Analysis. Microscopy: Science, Technology, Applications and Education. 2010, Vol. 3, p. 1583-1590.

Deadline for submission Master's Thesis is given by the Schedule of the Academic year 2023/24

In Brno,

L. S.

prof. RNDr. Tomáš Šikola, CSc. Director of the Institute	doc. Ing. Jiří Hlinka, Ph.D. FME dean

Abstract

This master’s thesis is concerned with the localisation and analysis of threading dislocations in GaN epitaxial layers. The thesis is divided into two parts – theoretical and experimental. The theoretical part explains the origin and nature of threading dislocations. Additionally, it lays foundations for a better understanding of perhaps less known techniques, which can be used to study them – electron channeling contrast imaging and defect-selective etching. The experimental part describes the procedures done to carry these techniques, in addition to TEM diffraction-contrast imaging and its associated FIB sample preparation, out. We show that each of the techniques can be used independently to characterize threading dislocations, but that there is a possibility to gain complementary information by combining them.

Keywords

GaN, ECCI, SEM, TEM, FIB, defect-selective etching, threading dislocation, diffraction contrast, invisibility criteria

Abstrakt

Táto diplomová práca sa zaoberá lokalizáciou a analýzou vláknových dislokácií v epitaxných vrstvách GaN. Práca je rozdelená na dve časti - teoretickú a experimentálnu. V teoretickej časti je vysvetlený pôvod a povaha vláknových dislokácií. Okrem toho kladie základy pre lepšie pochopenie možno menej známych techník, ktoré sa dajú použiť na ich štúdium - zobrazovanie elektrónového kanálovacieho kontrastu a selektívne leptanie defektov. V experimentálnej časti sú popísané postupy vykonané pri realizácii týchto techník, ako aj pre TEM zobrazovanie difrakčného kontrastu a s ním spojenej prípravy vzoriek pomocou FIB. Ukazujeme, že každá z týchto techník sa môže použiť samostatne na charakterizáciu vláknových dislokácií, ale že ich kombináciou je možné získať doplňujúce informácie.

Kľúčové slová

GaN, ECCI, SEM, TEM, FIB, selektívne leptanie defektov, vláknová dislokácia, difrakčný kontrast, podmienky neviditeľnosti

GAZDÍK, Richard. *Defect localization and analysis in GaN.* Brno, 2024. Master's Thesis. Brno University of Technology, Faculty of Mechanical Engineering, Institute of Physical Engineering. Supervised by Petr BÁBOR.

I hereby declare that I have written my master's thesis on the topic of *Defect localization and analysis in GaN* independently, under the guidance of my supervisor Ing. Petr Bábor, Ph.D., and using the technical literature and other sources of information, which are all properly quoted in the thesis and detailed in the references at the end of the thesis.

Bc. Richard Gazdík

Acknowledgements

I would like to thank my supervisor Ing. Peter Bábor, PhD. for his guidance and help not only on this master's thesis, but also on my bachelor's thesis, as well as on my Erasmus stay. My thanks also go to doc. Ing. Miroslav Kolíbal, Ph.D. for the discussions concerning this thesis. I am grateful to Ing. Eva Kolíbalová, Ph.D. for her help regarding the TEM sample preparation and work done on the TEM measurements.

I am also thankful to Ing. Martin Čalkovský, Ph.D for instructing me on how to carry out ECCI measurements.

I am thankful to the Institute of Physical Engineering for the instruments provided to me.

Last but not least, I thank my friends and my family, who always believed in me, for their support and for always being there for me during my studies.

CzechNanoLab project LM2023051 funded by MEYS CR is gratefully acknowledged for the financial support of the measurements/sample fabrication at CEITEC Nano Research Infrastructure.

Bc. Richard Gazdík

Contents

Introduction

Gallium nitride (GaN) is an up-and-coming semiconductor in power electronics thanks to its unique properties and the resulting possible applications. However, one big problem with GaN is the large density of threading dislocations in GaN layers, which is caused mainly due to the heteroepitaxial growth of GaN. Threading dislocations can negatively impact the performance, as well as reliability of devices produced from such layers. It is, therefore, desirable to minimize their number in GaN layers. This could be achieved by optimizing the currently used growing methods. To do this, we must be able to localize and characterize the threading dislocations in GaN. To this end, we chose three techniques, which can be used independently but also in combination to obtain complementary information – TEM diffraction-contrast imaging, electron channeling contrast imaging, and defect-selective etching.

TEM diffraction-contrast imaging is a common technique for the characterization of crystal defects in materials. It utilizes invisibility criteria to e.g. find the Burgers vector of a dislocation. Its main disadvantages are the lengthy sample preparation and the inability to observe bulk samples.

Electron channeling contrast imaging is also a diffraction-based technique, but performed in an SEM. It is a promising technique for localizing and characterizing threading dislocations in semiconductors because, in comparison to TEM analysis, it is non-destructive and can image bulk samples with little to no sample preparation. It can differentiate between the different types of threading dislocations but cannot determine their Burgers vector. As such, it can be used, in some cases, as a simpler alternative to more complex TEM analysis.

Lastly, defect-selective etching in molten bases functions by preferentially etching the material at dislocation sites due to their higher energy. Etching temperature and time play a crucial role in determining what kind of information can be obtained from this technique. It is a much faster and less operator-dependent technique than the previous ones. Because of this, it might be the simplest technique to localize and characterize threading dislocations industrially.

The aim of this thesis is to localize and gain complementary understanding of the nature of threading dislocations in GaN by using all of the above techniques. By using this information, the growing methods of GaN could be improved, which could result in better and more energy-efficient semiconductor devices.

The thesis' structure is divided into two main parts: 1. Theoretical part, and 2. Experimental part. The theoretical part includes 4 sections: 1.1 GaN section is concerned with the growing methods of GaN and its defects. 1.2 SEM section describes the signal types in SEM and common types of BSE detectors. 1.3 ECCI section explains the physics behind this technique and its capabilities of imaging defects. 1.4 Wet etching section demonstrates the abilities of various defect-selective etching techniques. The experimental part is divided into 5 sections: 2.1 Equipment section shows the samples we used and enumerates all the equipment we used for the different techniques. 2.2 ECCI measurements section discusses the process of doing ECCI measurements and the results we got from them. 2.3 KOH/NaOH etching section describes process of etching in molten bases and our results. 2.4 Lamella preparation section shows the process of obtaining a lamella by FIB. 2.5 TEM measurement section explains the information we got from performing TEM diffraction-contrast imaging on our lamella.

1 Theoretical part

1.1 Gallium nitride (GaN)

Gallium nitride is a binary III/V semiconductor with a direct bandgap. It is a hard material, and its most stable structure is wurtzite crystal structure, which is shown in Fig. 1.1. The first big breakthrough use of GaN in electronics was the creation of a high-brightness blue light-emitting diode (LED), which was an important step towards allowing us to create white light by combining the blue LED with the already discovered red and green LEDs. Over the last decade, GaN has turned out to also be an amazing material for use in power semiconductor devices, mainly in the fabrication of diodes and transistors. When compared to silicon, GaN-based transistors achieve a lot higher performance, which is caused by several of GaN properties. First, GaN has a wide bandgap E_g = 3.4 eV (Si has E_g = 1.12 eV), which allows its devices to be operated at very high temperatures (multiple times the maximum operating temperature of silicon transistors). Second, GaN layers can be up to 11 times thinner than Si layers to withstand the same applied voltage, which also reduces the resistivity of the device. Third, GaN devices can have very high switching frequencies, meaning they need smaller inductors and capacitors, resulting in smaller size devices. All these properties make GaN an exciting and useful material in the semiconductor industry [1].

However, when compared to Si, GaN is a relatively young material, so there is still a need for further research and development of it. All the possible applications of GaN rely on mass-produced devices, which quality depend on their growth methods. Thus, one major area of improvement is finding the ideal growing method because there are some issues with the currently used ones, which are described in the next section [2].

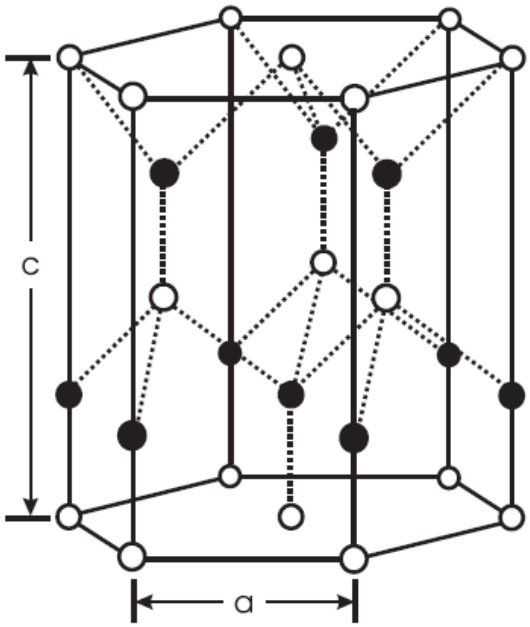

Fig. 1.1: Schematic GaN crystal unit cell – wurtzite structure with its lattice constants *a* and *c*. The structure is formed from two interpenetrating hexagonal close-packed (HCP) sublattices, each made from one type of atoms. Empty and full circles represent gallium and nitrogen atoms respectively. From [2].

1.1.1 GaN growing methods

Due to the high thermal stability of GaN it is impossible to grow GaN by techniques common for other semiconductors like Czochralski or Bridgeman method. As a result, there is a lack of free standing GaN wafers. In the next paragraphs, our focus will be directed to common growing methods, both their advantages and disadvantages, of epitaxial layers of GaN on a foreign substrate, known as heteroepitaxy [2].

Probably the most common epitaxial technique for growing GaN thin films is metalorganic chemical vapor deposition (MOCVD). In this process, a metalorganic precursor gas, typically trimethylgallium (TMGa), and ammonia (NH_3) are introduced into the reaction chamber. This chamber already contains the substrate, normally SiC or sapphire (Al_2O_3), needed for the epitaxial growth. Carrier gases are used to move the precursors over the surface of the substrate. The substrate is, meanwhile, being heated to the desired temperature, which depends on the reactor, of around 1000°C. The temperature is chosen in a way to establish a good ratio between deposition and desorption of GaN. As the precursor molecules move over the heated substrate, they get enough energy for their decomposition. TMGa dissociates to release gallium atoms, while NH_3 decomposes to provide nitrogen atoms. These atoms then react with each other on the substrate leading to epitaxial growth of GaN films. The remnants of the precursors are carried away from the reactor by the carrier gas or adsorb onto the walls of the reactor. At common operating reactor pressure of 50 mbar the achievable growth rate of GaN layers is about 1 μm/h. This rate of growth makes MOCVD viable for most applications of GaN but certainly not for bulk GaN growth. However, there are also some disadvantages, such as the complexity and cost of the MOCVD system, and not having the most ideal control over the grown layers, especially when growing heterostructures of GaN. Finally, susceptibility to formation of defects is a big problem, which can be partly solved by growing an AlN or GaN buffer layer on top of the substrate before starting the growth of the main GaN layer [2].

The second commonly used technique is molecular beam epitaxy (MBE). It is an ultra-high vacuum (UHV) technique for producing very high-quality epitaxial layers of GaN with great thickness control. This process starts again by choosing a suitable substrate, such as Si, SiC, or Al_2O_3 (sapphire). The chosen substrate is thoroughly cleaned and inserted into the MBE chamber, which is then evacuated to typically 10^{-6}-10^{-8} Pa. In contrast with MOCVD, gallium and nitrogen originate from atomic sources in MBE. Gallium is usually sourced from a heated effusion cell containing elemental gallium, which is evaporated into the form of a molecular beam. Nitrogen is typically supplied by an RF nitrogen plasma source, which, likewise, produces a molecular beam of nitrogen. Once the substrate is heated to a desired temperature, both molecular beams are directed at the substrate. When the travelling atoms arrive at the substrate surface, they can diffuse over it and combine with each other to produce GaN epitaxial layers. The layer growth rate is dictated mainly by the material flux of the molecular beams, which depends on temperature of the sources and can be stopped completely by using shutters. In this method, great care is taken of everything that could diminish the quality of the grown films, such as the cleanliness of the substrate, purity of the atomic/molecular sources, and the reactor base pressure. As a result, MBE has great thickness control over the grown layers, the achievable material purity of the layers is very

high, as well as the quality of the interfaces between different layers is significantly better than for other techniques. However, it has a lower yield compared to both techniques mentioned in this section [2].

The third and last technique that will be described here is hydride vapor phase epitaxy (HVPE). The HVPE process starts similarly to above-mentioned techniques by choosing a substrate, usually sapphire (Al_2O_3), and inserting it into a reactor, in this case a heated quartz chamber. The growing process is schematically depicted in Fig. 1.2. The reactants arrive at the substrate in gas phase. Gallium is delivered in the form of GaCl or $GaCl_3$, which in turn was created from the reaction of HCl with molten Ga. Nitrogen is sourced from a hydride, ammonia (NH_3), that is transported to the substrate by a nitrogen carrier gas, which is also the case for the gallium precursor. The substrate is heated to temperatures around 1000 °C, which causes the decomposition of the Ga and N precursors moving over the substrate and facilitates the epitaxial growth of GaN. In comparison with the previously mentioned techniques, HVPE achieves very high growth rates of >100 μm/h, which makes for a lower density of defects in the grown layers. On the other hand, because of the inadequate thickness control, caused by its high growth rate, HVPE may not be ideal for the growth of heterostructures. Finally, perhaps the biggest reason for using HVPE for GaN growth, specifically, is that it can produce free-standing GaN substrates, further improving the quality of GaN layers by allowing the homoepitaxial growth of GaN on such substrates [2, 3].

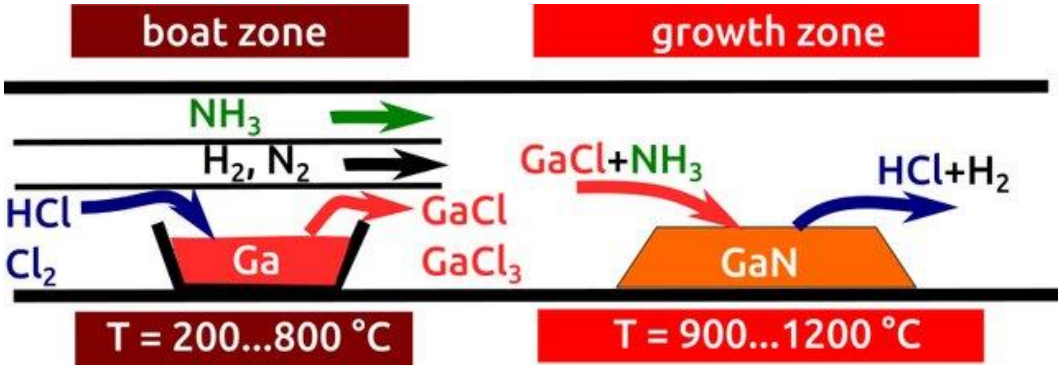

Fig. 1.2: HVPE process and reactor for GaN growth shown schematically. From [4].

In the process of epitaxial growth of GaN by each of these techniques, defects such as threading dislocations, which will further be described throughout the thesis, form inside the growing material. The reason for this is the significant lattice mismatch and the thermal expansion coefficient mismatch between the foreign substrate and GaN. These mismatches cause strain in the growing GaN layers, which can then be relaxed by creating dislocations inside the layers. The dislocations can cause various problems depending on the type of device made from the grown GaN. These problems can range from an increase in the leakage current, reduction in the blocking voltage, and limiting the peak electric field strengths in GaN power switches to reducing the switching frequency and increasing the dynamic ON resistance in GaN transistors [5]. In the case of GaN semiconductor lasers, dislocations can act as non-radiative recombination centres and degrade their associated internal quantum efficiency [6]. Fortunately, there are ways to reduce the density of dislocations in epitaxial GaN layers. One

common technique is to grow an AlN or GaN buffer layer on the substrate before growing the main GaN film [2, 7]. This buffer layer has a smaller mismatch to GaN than the original substrate and so less strain is involved when epitaxy is done on such interface, resulting in lower density of dislocations. The choice of the substrate is also important as some of them are more closely matched with GaN than others. When using sapphire as the substrate, the density of dislocations in GaN are of the order of 10^9-10^{10} cm^{-2} [8]. These values are one order of magnitude lower for SiC. Ideally, homoepitaxy would be utilized so that there is no mismatch at all, but for now it is not cost effective to do so on a large scale as the techniques that can create free-standing GaN are limited and require further development [2]. However, there were recently some advances for MOCVD homoepitaxy on HVPE GaN substrate, where they obtained layers with low density of dislocations, atomically flat GaN surface, and low impurity levels [9].

1.1.2 Defects in GaN

Crystallographic defects are irregularities in the repeating pattern of atomic arrangement within a crystalline structure. These defects can have an influence on various material properties like their mechanical, electrical, optical, and thermal characteristics. There are many different types of defects ranging from point defects (0D) through line defects (1D) to plane defects (2D), and volume defects (3D). In the next paragraphs, focus will be put mainly on defects, which have a sizeable impact on GaN layers and, consequently, on devices made from them.

The first possible type of a crystallographic defect is a point defect. Vacancies (missing atoms), interstitial atoms (extra atoms inserted in-between the lattice points) and impurities (foreign atoms replacing original lattice atoms) are all considered point defects as they interrupt the crystal structure only locally at a single point.

Vacancies occur naturally in every material due to an associated increase in entropy connected to their presence [10]. Additionally, vacancies can be created during the crystal growth. In GaN, there can be two types of vacancies: Ga-vacancy and N-vacancy. Ga-vacancies are common intrinsic defects in n-type GaN and act as acceptors, while N-vacancies are common in p-type GaN and act as donors [2].

Impurities include both intentional doping to change the conductivity of the sample to either n-type or p-type, and unintentional doping – incorporation of unwanted atoms into the sample during the epitaxial growth of layers. To obtain n-type GaN films, silicon and/or germanium can be used as donor impurities [7]. For p-type GaN films, magnesium is a common dopant acting as an acceptor [2, 7]. The most common unintentional donors in GaN layers are silicon and oxygen, both of which act as donors, and carbon that can act both as an acceptor and as a donor depending on the growth parameters [2].

The second possible type of a crystallographic defect is a line defect. Inversion domains (ID), nanopipes, and dislocations fall under the line defect umbrella. In the next paragraphs and throughout this thesis, our focus will be placed mainly on dislocations because they are the most common, and perhaps the most important, type of crystal defect in GaN layers. This fact is signified by the following quote: "*For some time now, the term "defect," when applied to gallium nitride (GaN), has usually denoted a threading dislocation*" [7].

Dislocations can be divided into edge, screw, and mixed type. A model of an edge and a screw dislocation can be seen in Fig. 1.3. An edge dislocation can

be thought of as an insertion of a half-plane of atoms inside the crystal as depicted in Fig. 1.3 b). This new half-plane displaces the faces of the crystal at the ABCD position by one atomic spacing. However, the biggest displacement of atoms from their original positions is very near the dislocation line DC. The distortion of the bonds between atoms decreases as the distance from the dislocation line increases. The second type – screw dislocation can be visualized by cutting a crystal along the ABCD surface and slipping the newly formed faces across each other in the AB direction as shown in Fig. 1.3 c). The DC line is then the screw dislocation and the crystal planes form a helix around it. The combination of an edge and a screw dislocation is called a mixed dislocation [10].

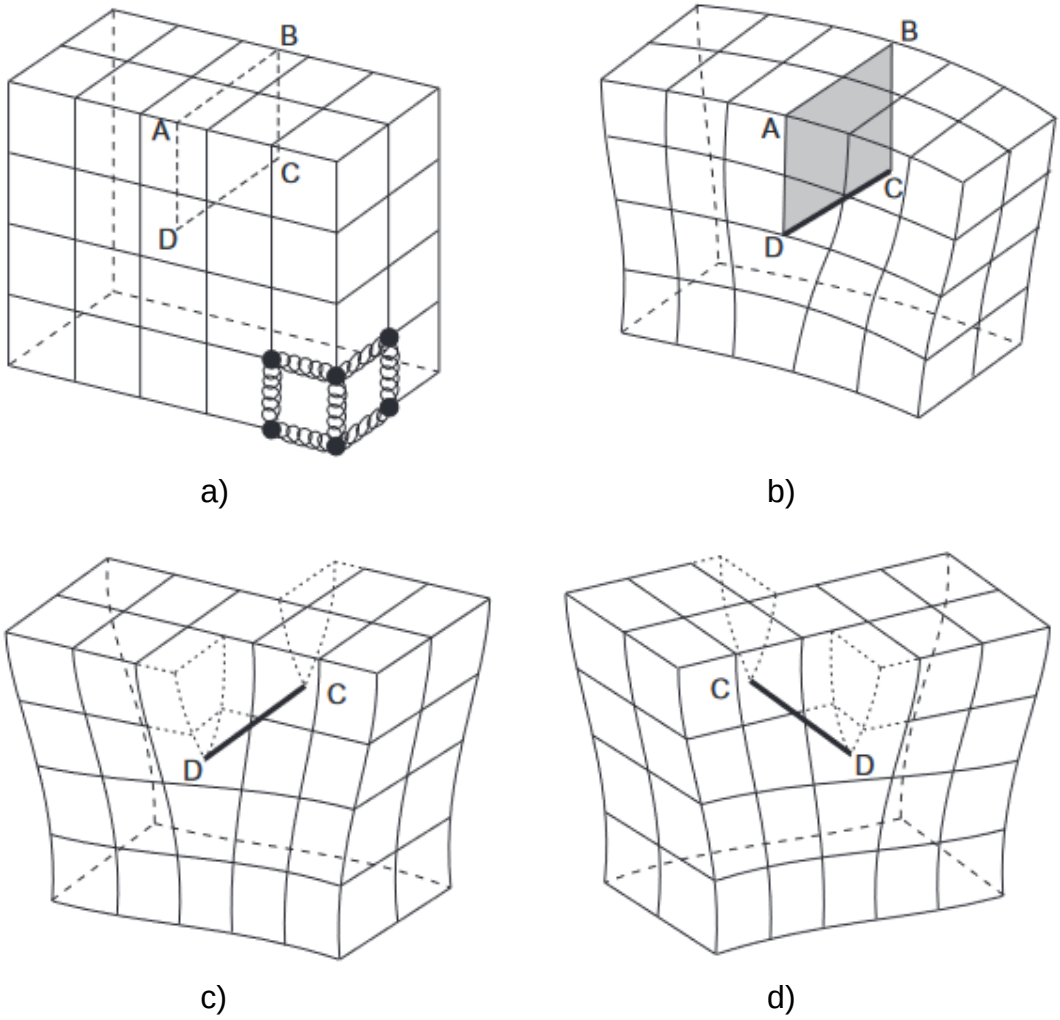

Fig. 1.3: a) Simple cubic lattice model. Atoms are located in the corners of the cubes and the bonds between the atoms are represented by springs depicted only for the bottom right cube. b) Positive edge dislocation DC created by inserting an extra half-plane of atoms in ABCD. c) Left-handed screw dislocation DC formed by displacing the faces ABCD relative to each other in the AB direction, and d) right-handed screw dislocation DC. From [10].

Dislocations cannot begin or end inside a crystal, therefore they must form closed loops, branch into other dislocations, or begin/end at grain boundaries or

surfaces of the crystal [11]. Dislocations are defined by their Burgers vector and the orientation of their dislocation line. A plane containing both vectors is known as the glide plane, and it is a plane along which the dislocations can move through the crystal [12]. The Burgers vector represents the direction and the magnitude of the crystal lattice distortion caused by a dislocation. It can be visualized as a vector that is needed to close a Burgers circuit that is made around a dislocation line when compared to the same circuit made in an undisturbed crystal. The Burgers circuit is just a closed path made atom-to-atom around a chosen area. In our case, MNOPQ is the Burgers circuit, and the closure failure QM is the Burgers vector, as can be seen in Fig. 1.4 a), b) for an edge dislocation and Fig. 1.4 c), d) for a screw dislocation. Based on these definitions, the important consequences are: for an edge dislocation, the dislocation line and the Burgers vector are perpendicular to each other, while for a screw dislocation, these two lines are parallel to each other. Generally, the angle between these two lines is arbitrary, resulting in a mixed dislocation [10].

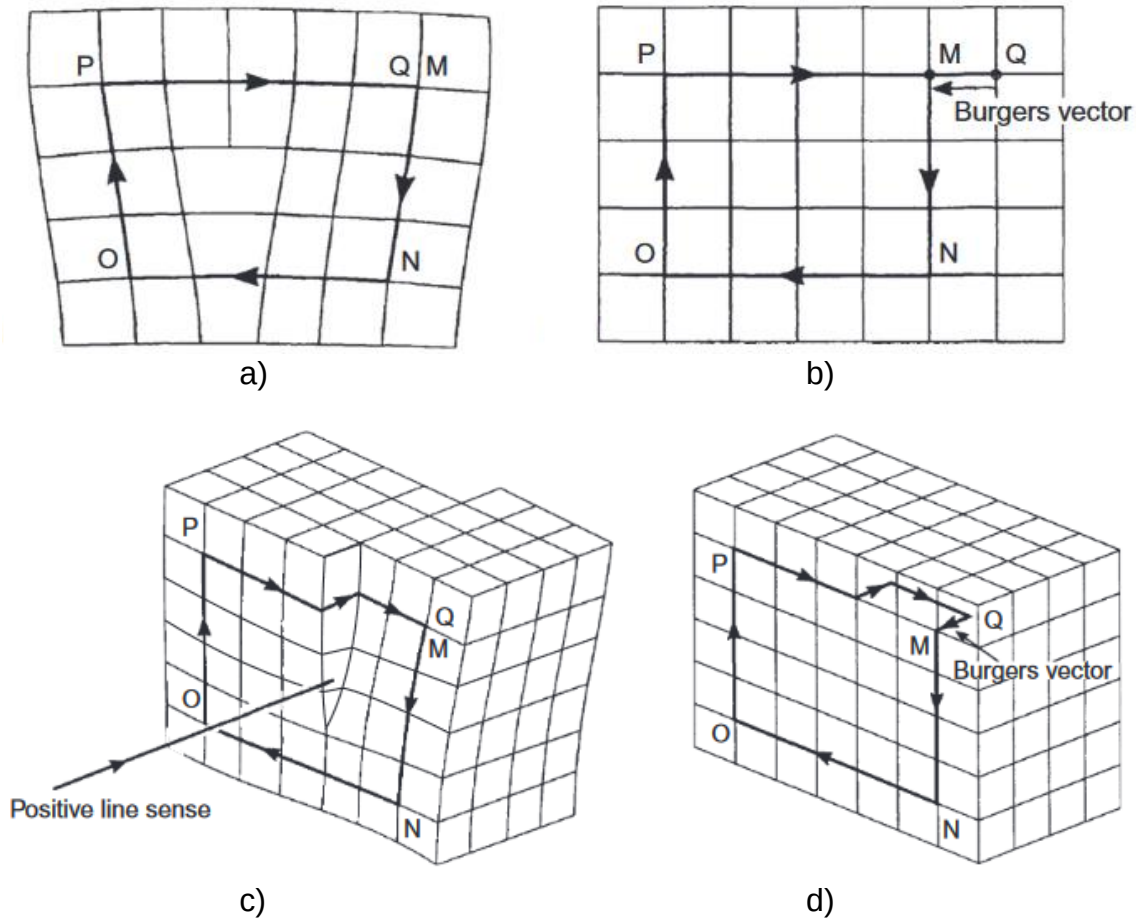

Fig. 1.4: a) Burgers circuit around an edge dislocation, and b) the same circuit for a perfect crystal, where the closure failure QM is the Burgers vector. c) Burgers circuit around a screw dislocation, and d) the same circuit for a perfect crystal, where the closure failure QM is the Burgers vector. Notice that for an edge dislocation, the Burgers vector is perpendicular to the dislocation line, which is pointing into the paper. Meanwhile, for a screw dislocation, the Burgers vector is parallel to the dislocation line. From [10].

The crystal structure of GaN is usually a wurtzite structure as was noted at the beginning of this chapter, especially in Fig. 1.1. It is a hexagonal close-packed structure with two smallest lattice translation vectors: ***a***-type $\frac{1}{3}\langle\bar{1}2\bar{1}0\rangle$ and ***c***-type $\langle 0001\rangle$. These vectors are also the Burgers vectors of unit threading dislocations (TDs), i.e. dislocations parallel to the *c*-axis that extend from the substrate interface throughout the epitaxial layer up to its surface. These TDs are an edge dislocation with a Burgers vector ***b*** = ***a***, and a screw dislocation with ***b*** = ***c***. There can also be mixed dislocations, which are a linear combination of an edge and a screw dislocation, known as (***a***+***c)***-type. Their Burgers vector is then from the following family of vectors: $\frac{1}{3}\langle 11\bar{2}3\rangle$ [2].

1.2 Scanning electron microscope

Ever since the invention of the optical microscope, scientists had to deal with a big problem. This problem is called diffraction, and it occurs when a wave is incident on an object or an aperture with dimensions comparable to the wavelength of the wave. This causes the wave to bend around the edges of the object, and allows the wave to get to places, which should be obstructed by the object. Such wave phenomenon can be well-illustrated by water waves or sound waves. Diffraction can be helpful, e.g. when we stand behind an obstacle, we can still hear the sound coming from behind it because the sound waves curve around the obstacle. However, when it comes to light waves, diffraction can be problematic because it limits the possible resolution of two points illuminated by a light wave if the points are closer to each other than the wavelength of the light. This means that with visible light we can, theoretically, only observe objects with sizes down to an order of 10^2 nm. However, we need a better resolution than this for our experiments, so we must make use of a different technique.

Electron microscopy allows us to image much smaller objects than light microscopy since electrons have a wavelength λ associated with them, which can be calculated from de Broglie's formula:

$$\lambda = \frac{h}{p} = \frac{h}{\sqrt{2mE_k}} = \frac{h}{\sqrt{2meU}}, \tag{1.1}$$

where h is the Planck constant, p is the electron's momentum, m is the electron's mass, E_k is its kinetic energy, e is the elementary charge, and U is the accelerating voltage. The wavelength of an electron accelerated by U = 1 V is then λ ~ 1 nm. In a scanning electron microscope (SEM), the electrons are usually accelerated by potential differences up to U = 30 kV. For such high energies, the special theory of relativity must then be taken into account. Nonetheless, an electron's wavelength is not the ultimate resolution-limiting factor in an SEM. The spot size of an electron beam at the sample determines the resolution of an electron microscope. Spot size is influenced by many factors, only one of which is diffraction. However, in this case it is tied to the electron beam diffracting on the apertures inside the microscope, which are used to limit the probe current, rather than a single electron wave being diffracted.

1.2.1 Signals

When an electron beam is incident on a sample, many interactions may take place. These interactions can be divided into two elementary types: elastic and inelastic scattering. The distinction between them is made based on whether the incident, also known as primary, electrons lose a part of their kinetic energy during the interaction or not. The products of these interactions, which are most commonly used for image formation in an SEM, can be seen in Fig. 1.5.

During inelastic scattering, the primary electron transfers some of its energy to an atomic electron of the sample. This gain in energy of the atomic electron can be high enough to cause it to leave its atom and start moving through the sample as a secondary electron (SE). SEs can have energies up to 50 eV [13].

Realistically, only SEs, which are generated in the top few nm of the sample, known as the escape depth, can leave the sample and are thus detectable, as illustrated in Fig. 1.5. Other SEs inelastically interact with the sample and lose the necessary energy to escape the sample. As a result, SEs can give us only topographical information about the examined sample [14].

During elastic scattering, the incident electron does not lose almost any energy, only its trajectory is changed as a result of the electrostatic interaction with the atomic nuclei of the sample. When an electron has its trajectory changed in this way by more than 90° from its original direction, it is ejected from the sample as a backscattered electron (BSE). The energy of BSEs can range from 50 eV up to the incident electron energy, and they can escape from almost half the penetration depth (tens to hundreds of nm) as illustrated in Fig. 1.5. BSEs give mainly material contrast information because the generation of BSEs is proportional to increasing the atomic number *Z* of a material. However, BSEs can also be utilized to show some topographical information if a detector, which is mounted on the side of the microscope chamber, is used [14].

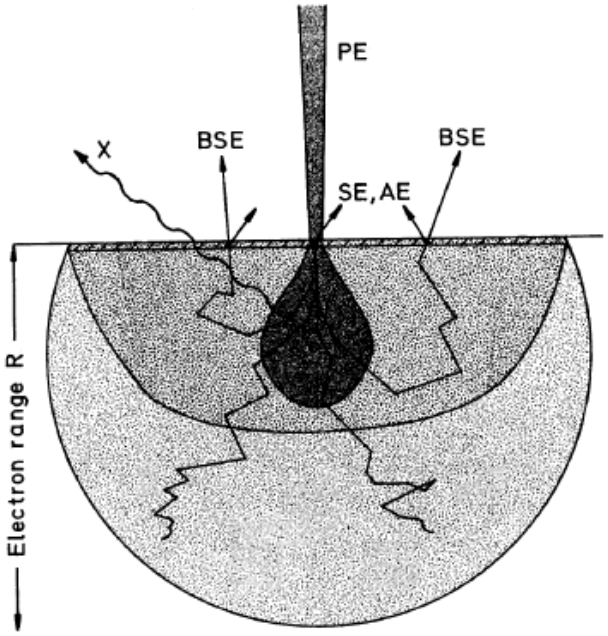

Fig. 1.5: Common products of the electron-sample interaction and their information volumes: secondary electrons (SE), backscattered electrons (BSE), Auger electrons (AE), and X-rays (X) generated by primary electrons (PE). From [13].

1.2.2 BSE detectors

Emitted backscattered electrons need to be collected so that they can provide signal for imaging of the sample. To better understand the physics behind the BSE image formation, two common types of BSE detectors, which are both usable in experiments carried out in this thesis, will be described in the following paragraphs.

The two types of detectors are: a scintillator detector, and a semiconductor detector. Both of these BSE detectors can have a large solid angle of collection. This is due to their sizeable area and position, as they can be located right under the polepiece with a central opening for the free passage of the primary beam. Due to their location above the sample, they give us mostly material contrast information

about the sample. In practice, both detectors can be mounted on a motorized retractable arm so that they do not interfere in imaging when they are not being utilized. In addition, both detectors are passive, which means that no acceleration is applied to the BSEs by these detectors. They can be passive because a considerable fraction of the BSEs created at energies of the primary beam $E_0 > 5$ keV keep most of this energy and thus have approximately straight trajectories. Finally, due to how each of them function (will be explained in the following paragraphs), higher energy BSEs contribute to the signal proportionally more than low energy BSEs [13, 15].

The first type is a scintillator, sometimes also called Robinson, detector. Its schematic can be seen in Fig. 1.6. It is made from an optically active material. This means that the BSEs incident on this detector are converted to photons by cathodoluminescence. On average, around 10-15 photons are generated by a 10 keV electron [13]. This is the cause for the greater influence of the higher energy BSEs on the signal of the detector. Light created in the scintillator then travels by total internal reflections through a light guide to a photomultiplier tube (PMT), which converts the light into an electric signal. From the variations of this signal, as the primary electron beam scans over the surface, the different contrasts in the BSE image are created [15].

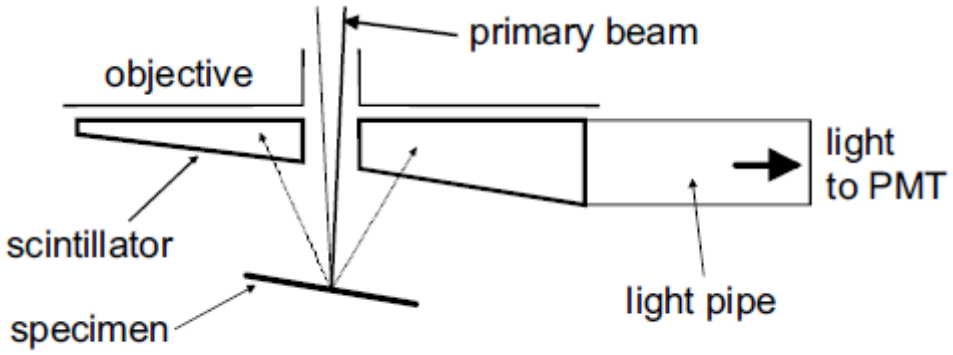

Fig. 1.6: Schematic of a scintillator (Robinson) BSE detector with a large solid angle of collection located between the specimen and the polepiece. From [14].

The second type of a BSE detector is a semiconductor diode, also known as solid-state, detector. Its schematic can be seen in Fig. 1.7. BSEs incident on the semiconductor material can undergo inelastic scattering. One product of the lost energy of the BSEs can be the excitation of the valence electrons of the semiconductor into the conduction band. The excited electron leaves behind a positively charged hole. We call this the creation of an electron-hole pair. These charge carriers can be split up before their recombination by an externally applied electric field (via metal surface electrodes). This creates a current through the diode, which we can measure at a surface electrode. For silicon, the creation of an electron-hole pair requires on average 3.6 eV. This means that a 10 keV BSE incident on the detector creates about 2500 electron-hole pairs. However, there is a threshold energy of the detector, which is normally a few keV, due to the energy loss of BSEs travelling through the front electrode. This is the reason for the bigger contribution of higher energy BSEs to the final signal, as was mentioned at the start

of this section. The main advantage of this type of detector is that it can be segmented into multiple parts, either radially away from the centre, or into quadrants. The signal from the individual parts can then be selected in various combinations, e.g. to find the angular distribution of BSEs, in the case of the concentric segments [13, 15].

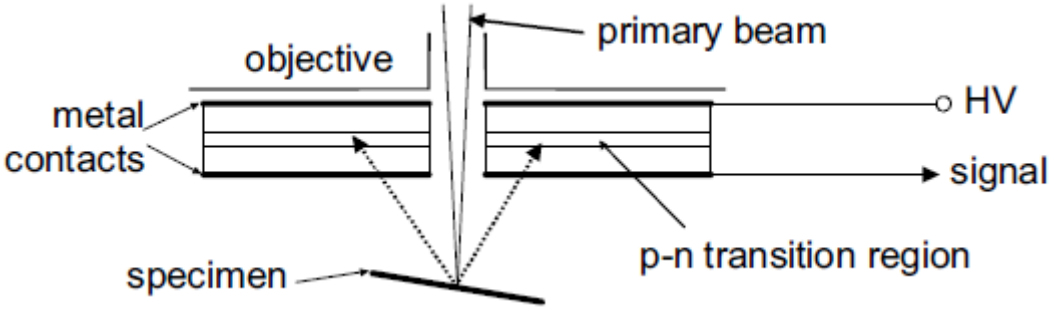

Fig. 1.7: Schematic of a semiconductor (solid-state) detector composition and location relative to the specimen. From [14].

1.3 Electron channeling contrast imaging

In order to improve the properties of semiconductor epitaxial films, precise analysis of their crystallographic defects is of vital importance. This is the case because such defects can considerably lower the performance of the devices made from these films. Probably the most widely known and used technique for such analyses is transmission electron microscopy (TEM). By using TEM, extended defects such as dislocations, stacking faults, or twin boundaries can be imaged and quantified directly with exceptional spatial resolution. However, TEM is by design a low-throughput method due to its time-consuming sample preparation, which can largely slow down the speed of studying these defects. Additionally, TEM sample preparation is destructive, which causes further problems. Among these problems are the inability to image larger areas (usually >100 μm^2, or >10 μm^2 for surface analysis) of the original sample at a time due to the limited size of the prepared lamella. Connected to this is the difficulty of analysing samples with lower dislocation densities (<10^6 cm^{-2}, meaning that dislocations in these samples may be more than microns spaced apart). Lastly, the microstructure or the strain state of the sample may be altered during the sample preparation, possibly leading to unreliable or inconsistent results [6, 16].

Historically, electron channeling had been considered as a possible method for studying crystalline materials ever since its discovery in the SEM micrographs of bulk monocrystalline samples in 1967 by Coates [17]. Not long after, it was becoming clear that electron channeling could be used for both imaging and identifying crystallographic defects by SEM in a comparable manner to that achievable by TEM [18]. Despite being incapable of providing the same spatial resolution as TEM, it was observed that the SEM-based method – electron channeling contrast imaging (ECCI) – can take advantage of some of the contrast mechanisms typically used in TEM. To be more specific, the lattice strain associated with crystallographic defects in a sample could generate contrast in an SEM equivalent to the TEM diffraction contrast. In the past, ECCI was mainly used to study dislocation networks related to metal processing and deformation. However, more recently there have been rigorous studies of individual extended defects even for low defect density specimens such as bulk crystal semiconductors and ceramics [19].

In the case of GaN epitaxial layers, threading dislocations are the prominent defects [7]. They can be studied by ECCI in any modern SEM equipped with a field emission gun, providing adequate probe current and resolution, by using a BSE detector with high collection efficiency, and utilizing a small beam convergence angle (more details in the next sections). ECCI is a diffraction-based imaging technique carried out inside an SEM [20]. When compared to the above-mentioned TEM diffraction-contrast imaging, ECCI is advantageous in terms of being able to image bulk samples, rapidly providing data from multiple areas over the sample, while requiring little to no sample preparation (in the study of epitaxial layers) [21]. Both techniques are similar in terms of having sufficient spatial resolution to image individual dislocations, their information depth (~100 nm [22, 23]), and enabling the imaging of defects under specific diffraction conditions [24]. However, TEM imaging is better for characterizing threading dislocations and it is also less sensitive to misalignments, when choosing the specific diffraction condition, compared to ECCI [20].

1.3.1 Electron channeling pattern formation

As was mentioned in the previous chapter, the first observation of electron channeling in an SEM was made in 1967 by Coates. It was done by simply observing single-crystal samples using backscattered electrons at a low magnification (scanned area of about 4 mm × 4 mm), utilizing a beam of high intensity with a small convergence angle. What was observed is a pattern of overlapping bands, now known as electron channeling pattern (ECP) – seen in Fig. 1.8 – similar in appearance to the Kikuchi pattern known from TEM. In such patterns, each band corresponds to a set of crystal planes in the specimen. This study also established that the width of the Kikuchi-like bands is proportional to the de Broglie wavelength of the incident electrons [17].

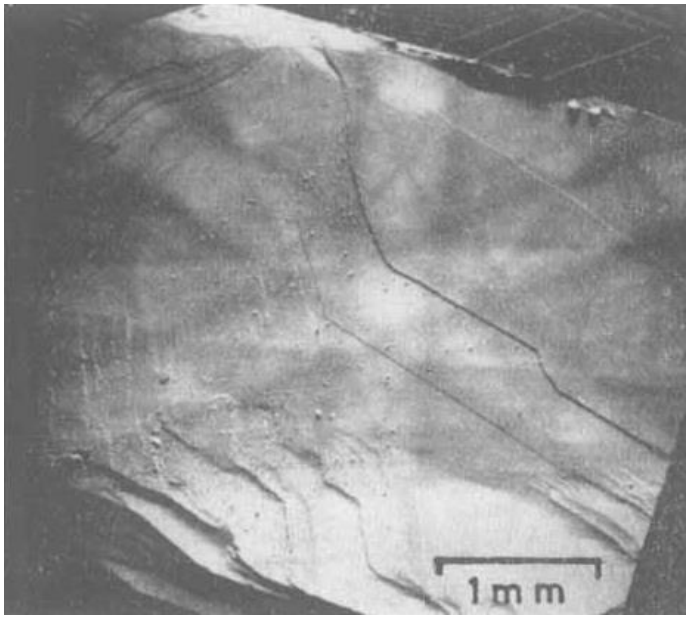

Fig. 1.8: Cleaved (110) face of GaAs with the electron channeling pattern superimposed onto the topographical BSE micrograph of the sample. From [17].

The physics behind the formation of an ECP can be explained quite simply, even though it can be quite complicated to understand all the details, like the intensity of certain bands, of an ECP mathematically. For the purposes of understanding the ECCI measurements carried out in this thesis, it is not necessary to go into full details. The mechanism of ECP formation can be explained in several different ways. Furthermore, there are some analogies to the TEM Kikuchi pattern and electron backscatter diffraction pattern formation. The difference between them is that: "*As opposed to Kikuchi patterns produced via electron backscatter diffraction (EBSD) or TEM, which are formed via outgoing electron diffraction, ECPs are a result of incident electron diffraction/channeling*" [16].

The simplest explanation of ECP formation is by using the particle model of an electron. For amorphous materials, the backscattering intensity is the same for all electron incident angles because the density of atoms of the material is the same in all directions. However, for crystalline materials, some electron incident angles give a lower backscattering intensity. This is the case when an electron moves parallel between the crystal lattice planes. In such cases the density of atoms of the material seems to be smaller because all the atoms are positioned

along a line, resulting in a lower probability of backscattering of the incident electrons. Therefore, we can expect that the backscattering signal from a crystalline sample will be modulated based on the relative orientation of the crystal structure to the incident electron beam as can be seen in Fig. 1.9 a) [25].

An alternative model for ECP formation can be used when thinking of the electron as a wave. It is logical to do this considering that the energies the electrons are accelerated to in an SEM are in the keV range. In this case, the channeling effect can be represented by a diffraction of the electron wave by the crystal lattice. In the wave model, the incident electron flux propagating through the lattice is mathematically equivalent to multiple standing waves, called Bloch waves, having the periodicity of the lattice. Bloch waves are plane waves travelling from the surface through the crystal. Their wavefront is parallel to the surface normal. The probability of an electron being at any point of the wave is given by the square of the Bloch wave amplitude at that point. In the most basic case, only two types of a Bloch wave – type I and type II Bloch wave as depicted in Fig. 1.9 b) – must be considered. The type I Bloch wave has its intensity maxima on the lines of atom sites creating the lattice planes. The type II Bloch wave has its maxima shifted half a wavelength – located halfway between the lattice planes. The electrons in the type I wave have a high probability of interacting with the nuclei of the atoms in the lattice, resulting in strong backscattering. On the other hand, the type II wave is relatively distant from the lattice sites, interacting only weakly with the lattice, thus resulting in weak backscattering. Considering the incident electron flux to be constant, the sum of the intensities of the two Bloch waves is, then, also constant. When the incident angle θ (beam convergence semi-angle) satisfies the Bragg's condition for lattice spacing d such that:

$$2d \sin\theta = \lambda, \tag{1.2}$$

where λ is the electron wavelength, then both waves have equal intensity. However, when the incident angle $\theta < \theta_B$ (where θ_B is the Bragg angle), the intensity of wave I is larger than that of wave II and the total backscattered intensity increases. For the other case, when $\theta > \theta_B$, the intensity of wave I is smaller than that of wave II and fewer electrons are backscattered [25].

Let us consider the situation in Fig. 1.10 where an electron beam is scanned over the flat surface of a monocrystal. During the scanning over the surface, the relative angle of the electron beam to the lattice varies, therefore the backscattered signal will be changing, as was explained in the previous paragraph. At points A and B, $\theta = \theta_B$, meaning that between these two points the beam angle of incidence $\theta < \theta_B$ resulting in increased backscattering. In the other case, to the left of A and to the right of B, $\theta > \theta_B$ and the backscattered signal is decreased compared to the value at A and B. The profile of the backscattered signal as a function of the scan angle will thus look as in Fig. 1.10 with a band of higher signal $2\theta_B$ in width centred at the position where $\theta = 0$. In the case of a full 2D raster, as is common in the SEM, the other sets of lattice planes of the crystal will contribute to the signal and the resultant signal plot – the ECP – formed in this way will contain contrast bands from all sets of planes normal, or almost normal, to the surface. The width of each band will be twice the Bragg angle corresponding to the set of lattice planes, from which the signal originates, and the angle between the bands will be the same as the angle between the respective sets of lattice planes in the crystal [25].

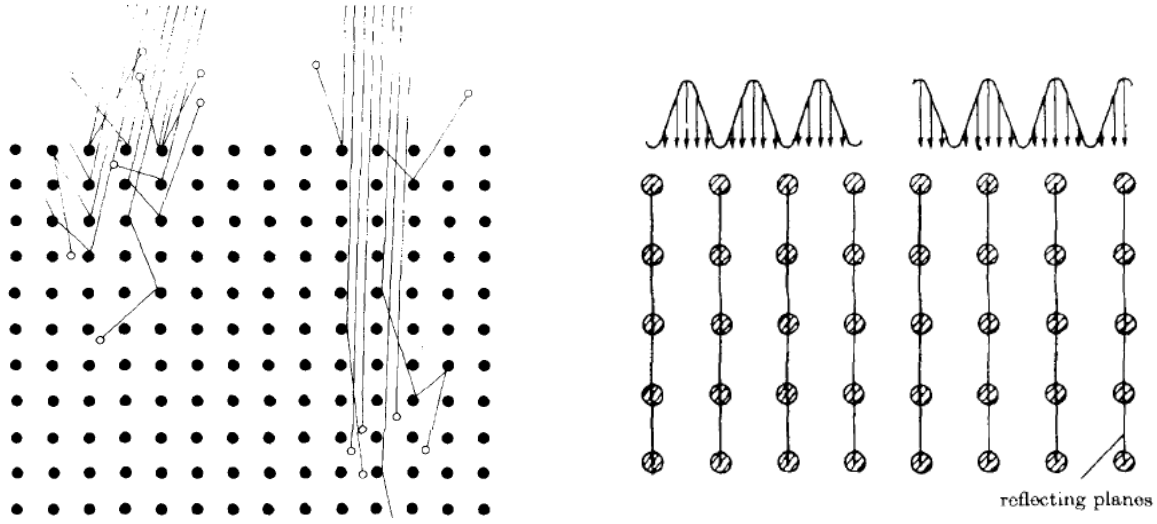

a) b)

Fig. 1.9: a) Particle model of electron channeling for two different incident beam angles relative to the crystal lattice. For the beam on the right that is parallel to a set of planes, backscattering is lowered. b) The Bloch Wave model of electron flux in a crystal. In this simplest case the flux can be expressed by just two components: Bloch Wave II (left), which has its intensity maxima between the planes, and Bloch Wave I (right), which has its maxima on the line of atom sites. From [25].

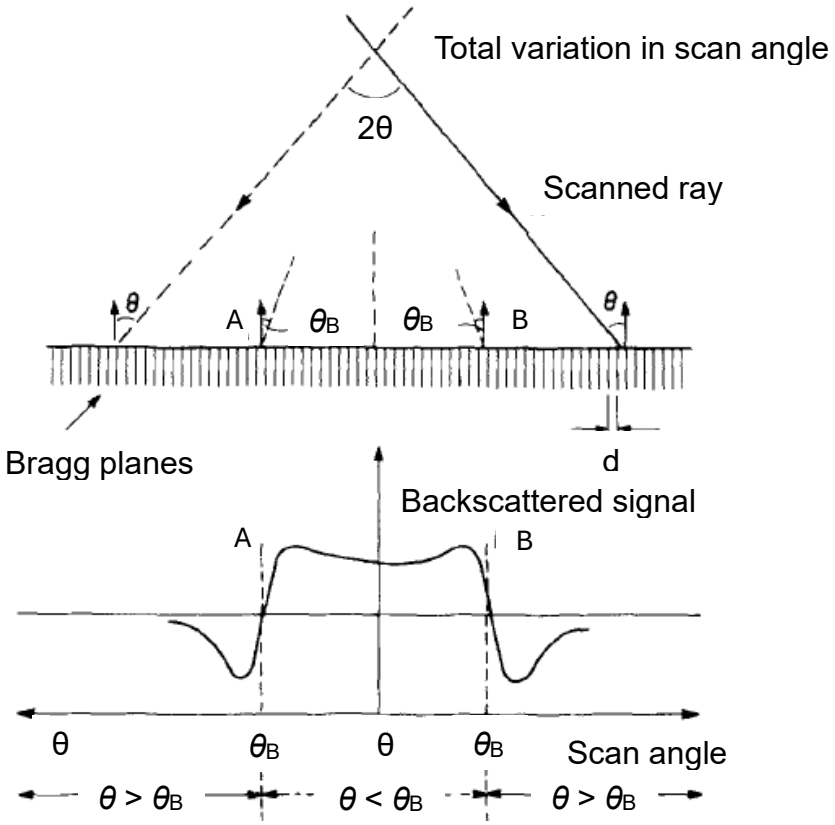

Fig. 1.10: Variations in the incident beam angle during scanning. Throughout every line scan, the incidence angle θ will vary from $\theta > \theta_B$ (θ_B is the Bragg angle) to $\theta < \theta_B$. At two symmetrical positions *A* and *B*, $\theta = \theta_B$. These variations give the changes in the backscattering signal intensity shown below. Adapted from [25].

Having either of the two described models as a basis for explanation, an ECP can be acquired by scanning an electron beam over the specimen surface at low magnification while recording the variations in the BSE intensity. To give an example: at a working distance of 10 mm and for a field of view of 5 mm, the angle between the incident beam and the surface of the sample varies by approximately ±14° during a line scan. Such angles are more than sufficient for the beam to satisfy the Bragg condition for many different sets of crystal planes during the raster (the Bragg angles of the lowest index planes are low units of degrees). The result of this simple procedure is a pattern similar to the one in Fig. 1.8 [25, 26].

For ideal ECP micrographs, the whole scanned area should have identical orientation, the scanning speed should be small (tens of seconds for a scan) to increase the signal-to-noise ratio (SNR), and a beam with a small convergence angle (a few mrad) and a high current (units of nA) is to be used. The angular width of a channeling band depends, among others, on the spacing of the corresponding set of crystal planes, electron wavelength (decided by the used accelerating voltage), working distance (WD), and magnification used to obtain the ECP. The ECP is 'attached' to the crystal orientation and so its shape will not change when moving over an area with identical orientation. An ECP can be obtained from any electron signal (e.g. secondary electrons, specimen current, or even transmitted electrons for thin samples). In addition, many ECPs can be combined to create a channeling map similar to the one Fig. 1.11, which can then be indexed, and it is the same for every sample with the same crystal system [25].

In order to obtain only an ECP, without it being superimposed onto the topography of the sample, a technique called *'rocking beam'* can be used. This technique can be carried out automatically by some SEMs, in which the beam deflection scan systems can be used to 'rock' a thin electron beam about a pivot point on the specimen surface. The resulting image is an isolated ECP (Fig. 1.11 is composed of multiple such ECPs taken for different relative orientations of the beam and the sample) constructed by an angular scan of the sample, in some SEMs up to ± 11° [27].

For polycrystalline samples or materials with significant crystal distortions caused by large amounts of plastic strain, a selected area channeling pattern (SACP) has to be utilized to get similar information as from an ECP [28]. In this case, the *rocking beam* technique must be used so that there is no lateral motion of the beam during the angular scan of the chosen area. In addition, the effect of spherical aberration of the magnetic lenses in the SEM must be corrected for. This is because the spherical aberration of the objective lens causes the electrons which are further away from the optical axis to be focused more than the ones closer to it. As a result, the beam is rocked about a bigger spot rather than about a single point. The minimization of the spherical aberration and the choice of a maximum rocking angle is what ultimately decides the resolution of both an ECP and an SACP. Naturally, in the case of investigating polycrystalline samples, it is necessary to attain a resolution smaller than the size of the studied grain [27, 29].

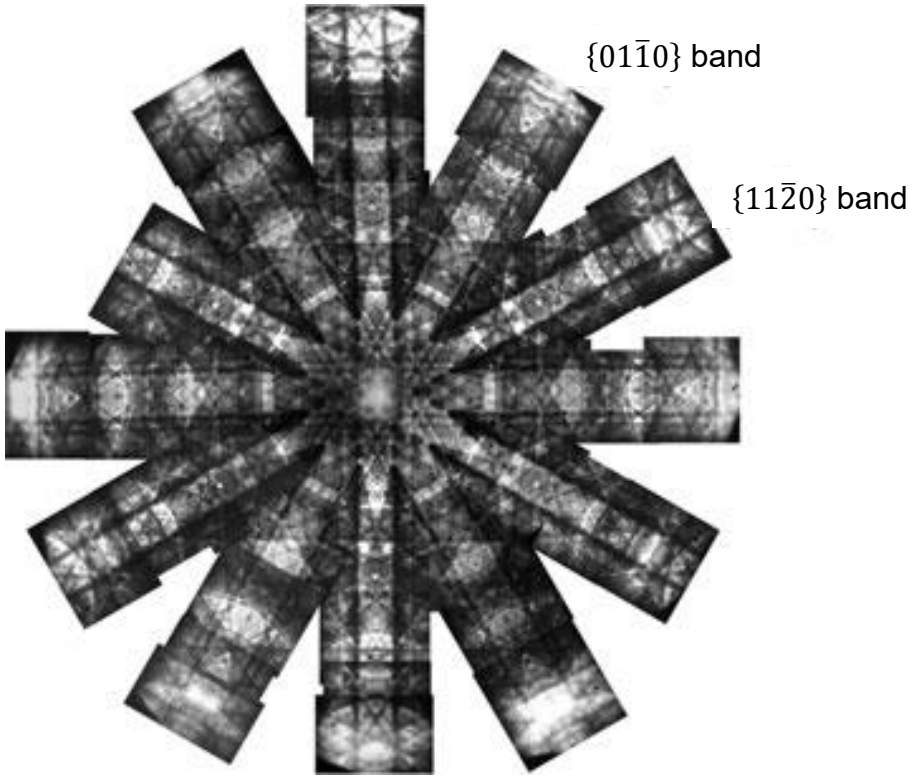

Fig. 1.11: Collection of many ECPs of a MOCVD GaN (0002) thin film. Adapted from [24].

1.3.2 Electron channeling conditions

Not long after Coates [17] observed ECPs formed by electron channeling, Booker et al. theorized that it should be possible to image defects as: "*it was only necessary to orient the crystal at the Bragg position and the local bending of the crystallographic planes where the dislocations emerge at the surface should provide the necessary contrast*" [18]. Today we know that it is, indeed, possible to image crystallographic defects, even individual dislocations using electron channeling. As we already know, electron channeling is a relation between the incident electron beam, crystal orientation and backscattered electron yield.

Now that we know how to utilize the electron channeling mechanism to obtain an ECP, and have successfully done so, we can make further use of it. As was mentioned in the previous chapter, the ECP is 'attached' to the crystal orientation. Therefore, by changing the crystal orientation, by rotation and tilt of the sample, we can move the ECP without moving the electron beam out of our region of interest (ROI). In-plane rotation of the sample results in a rotation of the ECP as shown in Fig. 1.12. Out-of-plane tilt of the sample results in a linear movement of the ECP as shown in Fig. 1.13 (the direction of movement depends on the microscope stage tilt axes) [16]. By using these movements, we can align the optical axis of the microscope with the edge of a single channeling band in the ECP. This alignment corresponds to the un-tilted beam satisfying the exact Bragg channeling condition of a certain set of planes [30]. The set of crystal planes is defined by their normal, using their reciprocal lattice vector ***g***. By following this procedure, we choose the imaging diffraction vector ***g***, which is the normal to the chosen set of planes [20].

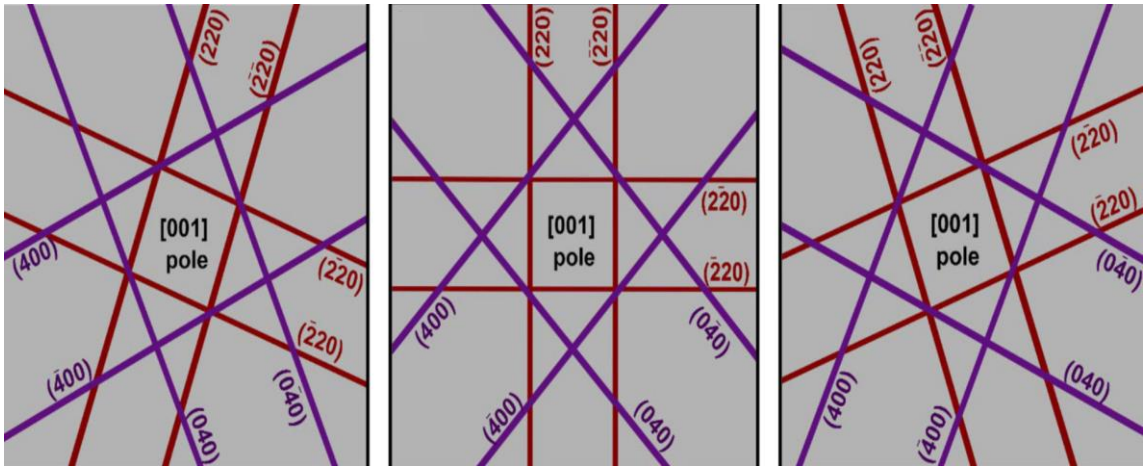

Fig. 1.12: In-plane rotation of the specimen results in a rotation of the ECP (GaP/Si specimen): a) rot = -20°, b) original ECP with rot = 0°, c) rot = 20°. From [16].

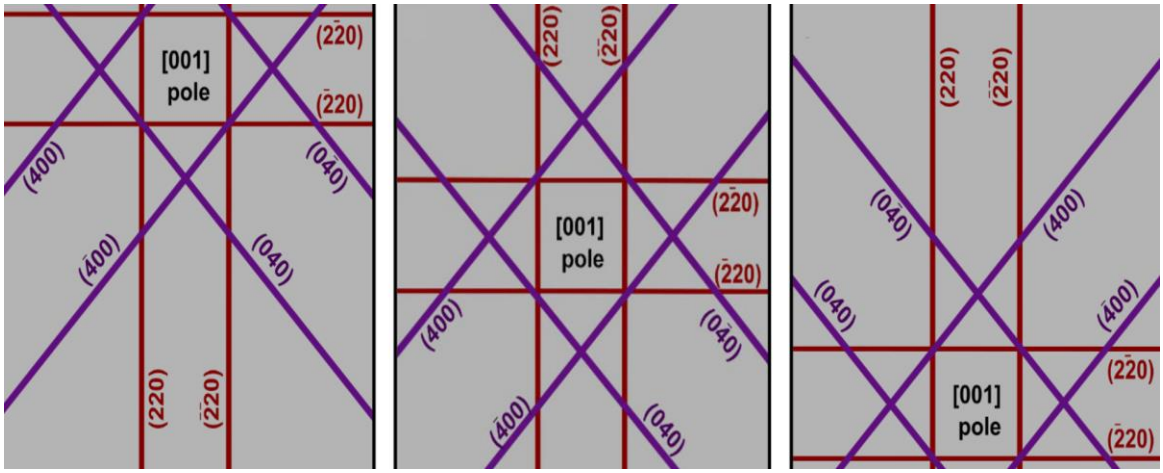

Fig.1.13: Out-of-plane tilt of the specimen results in a linear movement of the ECP (GaP/Si specimen): a) tilt = -4°, b) original ECP with tilt = 0°, c) tilt = 4°. From [16].

After successfully choosing a diffraction condition ***g***, ECCI can be carried out to image defects visible for this condition. To begin, the magnification is increased so that the field of view (FoV) is reasonable based on the size of the defects of interest. At such high magnifications there are two main ideas to consider. First, as shown in Fig. 1.14 a), the incident electron beam angle can be considered constant over the scanned FoV (for usual imaging conditions, the change in beam trajectory is ~1 mrad, which is relatively small compared to the typical beam convergence angle of 5-6 mrad [20]). Second, due to the angular range restriction, only a single 'channel', corresponding to a specific set of planes, is isolated. Hence for a perfect crystal there should be a constant signal [21]. This constant contrast level will only change when there is a change in the lattice orientation of the different regions of the sample relative to the perfect crystal. [25] ECCI can be understood using the particle model of an electron. For example, the presence of even an individual defect, such as a dislocation, can block the chosen channel by locally bending the crystal planes around it, resulting in more electrons being backscattered than for the perfect crystal. Alternatively, the defect can open

a channel and allow electrons to penetrate further into the crystal, decreasing the number of detected BSEs. In both cases we can observe dislocation contrast in BSE intensity caused by electron channeling [21]. The shape of the BSE intensity as a function of the position along a dislocation, seen in Fig. 1.14 b), can also be explained by the Bloch wave model. The incident beam angle θ on the left of the dislocation in Fig. 1.14 a) gives lower backscattering due to the intensity of type II Bloch wave being larger for $\theta > \theta_B$. On the other hand, for $\theta < \theta_B$ on the right of the dislocation the type I Bloch wave is more intense and so the backscattered intensity increases [29].

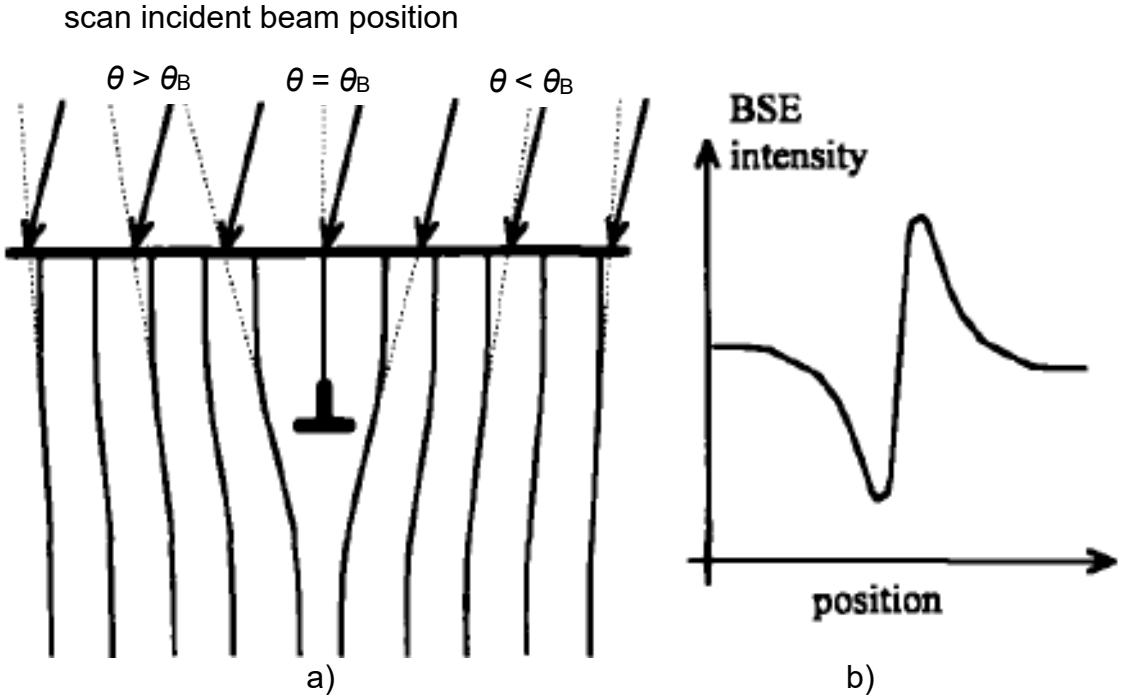

Fig. 1.14: a) Schematic of ECCI showing an almost parallel electron beam incident on a surface of a crystal. The crystal planes are distorted due to the presence of a dislocation. b) The BSE intensity variation caused by the dislocation. Adapted from [29].

ECCI is commonly used for both metals and semiconductors to image various crystal defects such as grain boundaries, subgrain boundaries, twins, dislocation bundles or deformations due to cold working [25, 31]. Even remarkably small differences in orientation and strain are detectable by ECCI, revealing e.g. low-angle tilt and rotation boundaries or atomic steps while also enabling extended defects such as dislocations and stacking faults to be imaged [32, 33].

There are several requirements to be able to obtain good quality micrographs of crystal defects by ECCI. Some things were mentioned as necessary already in the previous section about ECPs, but a more thorough description will be provided here.

Firstly, we will look at the sample preparation necessary to carry out ECCI. To begin, an important fact to consider is that the modulation of backscatter intensity signal caused by electron channeling, as seen in Fig. 1.14 b), accounts for around 5% difference between the maximum and minimum value [15]. To be able to measure such small differences between the two intensities, thus detecting

electron channeling contrast, multiple precautions to increase the signal-to-noise ratio must be taken. In addition, as we already know, the information depth of ECCI covers, at most, the upper 100 nm of the specimen, therefore, oxide layers or mechanical surface damage considerably deteriorate the quality of ECCI micrographs [31]. Consequently, a flat and smooth surface of the sample is desired to eliminate the competing signal from topography caused by surface roughness [25]. For metal samples, the sample preparation usually involves fine grinding, metallographic polishing and electropolishing to get rid of any contamination on the surface [31]. In the case of epitaxial layers, no such sample preparation is usually needed. Another source of contrast in BSE imaging is Z-contrast caused by atoms of different materials being present. Therefore, if possible, it is ideal for the sample to be chemically homogeneous, at least at the region of interest, to also eliminate this competing BSE signal [24].

Secondly, the necessary properties of the SEM components will be discussed. First, there is a strong dependence of electron channeling contrast on the beam convergence angle. The smaller the beam convergence angle is, the smaller changes in crystal orientation can be observed [27]. However, this angle is defined by the radius of the final aperture lens, which cannot be easily changed by the operator of an SEM. Second, due to the need to further improve SNR, a higher number of incoming electrons per unit area of the sample is desired. Therefore, a high brightness electron source is necessary. To this end, a field emission gun (FEG), which also achieves the necessary spot size, is usually used for ECCI [31]. Third, concerning the choice of a BSE detector. It is a fact that the high energy BSEs are the ones responsible for the channeling contrast [15, 24]. To collect as many of these signal electrons as possible, an arrangement with a large solid angle BSE detector (either scintillator or solid-state detector, both were described in the previous chapter) mounted below the polepiece with the sample normal to the beam is ideal. The working distance is chosen as small as possible while allowing for the tilt of the sample so that it does not hit the detector when aligning the sample to a desired diffraction condition [20].

Thirdly, concerning the imaging settings needed for optimal ECCI micrographs. As mentioned above, SNR needs to be increased as much as possible because the number of BSEs carrying channeling contrast information is relatively low. To this end, the signal for a single micrograph should either be obtained over longer periods of time (tens of seconds), or some combination of line and/or frame integration should be taken advantage of. Another important imaging parameter is high voltage (*HV*). Lower values of *HV* (5 kV) can be used, e.g. to image atomic steps [21]. However, usage of higher energy electrons (10-30 keV) is usually desirable. This is the case for two main reasons. First, as was mentioned in the previous paragraph, the higher energy BSEs are responsible for the generation of channeling contrast and, logically, higher energy incoming electrons generate more higher energy BSEs [15]. Second, higher *HV* results in higher resolution, allowing imaging of individual dislocations [21].

Finally, because of the weakness of the electron channeling signal, the contrast and brightness imaging parameters must be well adjusted. This is done by maximizing the contrast and minimizing the brightness parameter to spread the channeling contrast over the full black-to-white range [15].

1.3.3 Defect imaging

Some of the mechanisms behind the shape, size, and contrast of defects in the ECCI micrographs will be explained here. Emphasis will be put on the threading dislocations (TDs) in GaN as those will be analysed later in the experimental part of this thesis. As was already described in the first chapter, TDs are vertical dislocations that extend from the substrate interface throughout the epitaxial layer up to its surface. Under ideal imaging conditions, ECCI reveals TDs as dots with a bright-dark contrast [22]. The sense of the dislocation contrast is influenced by the deviation parameter s, which is defined as positive for $\theta > \theta_B$, negative for $\theta < \theta_B$ and zero for $\theta = \theta_B$, as can be seen for various dislocations in Fig. 1.15. The figure shows that the contrast for dislocations is weak against a bright background for negative s, bright-dark for $s = 0$, and bright against a dark background for positive s [20]. This kind of relation of dislocation contrast with s could be predicted by the Bloch wave model. The directionality of the bright-dark contrast depends on the Burgers vector of the dislocation, i.e. the direction and magnitude of local lattice displacement induced by the dislocation. Furthermore, this directionality changes based on the chosen diffraction condition $\boldsymbol{g}$, and it can be used to characterise the dislocations by their Burgers vector as will be described in the next paragraph [29].

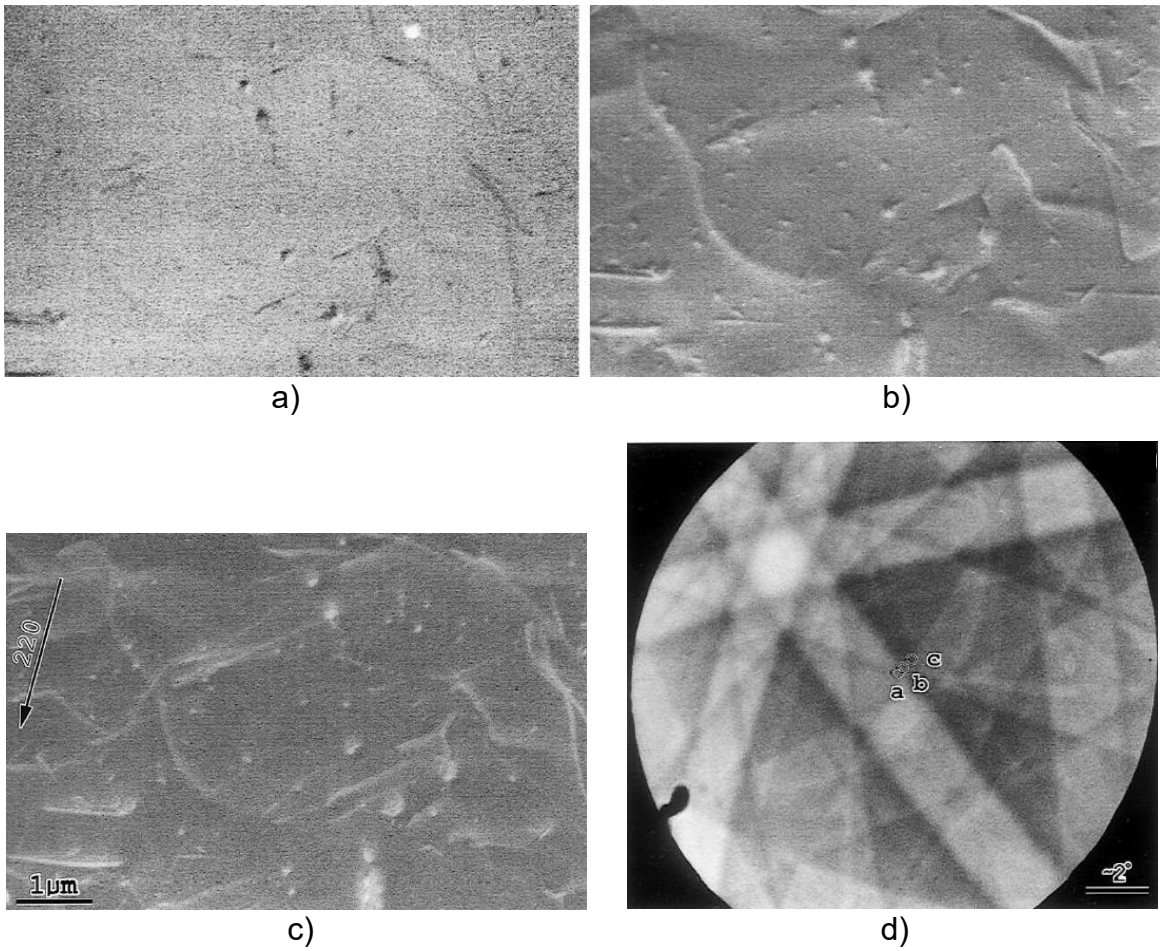

Fig. 1.15: ECCI micrographs taken under differing deviations from the Bragg channeling condition, using $\boldsymbol{g}$ = (220): a) $s < 0$; b) $s \approx 0$; c) $s > 0$. d) Approximate position of the optical axis relative to the ECP for each case. From [20].

Regarding the characterization of defects, the same invisibility criteria are useable in ECCI as are common for TEM diffraction contrast. The defects are invisible if these conditions are satisfied: $\boldsymbol{g} \cdot \boldsymbol{b} = 0$ and $\boldsymbol{g} \cdot (\boldsymbol{b} \times \boldsymbol{u}) = 0$, where $\boldsymbol{g}$ is the diffraction vector, $\boldsymbol{b}$ is the Burgers vector, and $\boldsymbol{u}$ is the dislocation line element [16]. Invisibility of a dislocation under a specific diffraction condition can occur because only the electrons that are diffracted from planes that are distorted by the defect contain the defect information [22]. Usage of the $\boldsymbol{g} \cdot \boldsymbol{b} = 0$ invisibility criterion has been demonstrated in a $SrTiO_3$ (001) sample. It was possible since there were some dislocations that did not penetrate the surface (not TDs). Additionally, for such sub-surface dislocations, their Burgers vector can be established by accessing several diffraction conditions [21]. The need for both invisibility criteria to be met for certain dislocations were shown in the ECCI study of pure edge dislocations in FeAl polycrystals [34].

Threading dislocations are a unique type of defect for ECCI characterisation. They penetrate the surface and cause surface relaxation effects, so they do not go fully out of contrast for any diffraction condition, making it difficult to establish their Burgers vector by the aforementioned invisibility criteria [24].

In ECCI micrographs of GaN, TDs appear as bright-dark spots. Threading screw dislocations (***c***-type) in GaN have the Burgers vector $\boldsymbol{b_c} = \langle 0001 \rangle$ that is about 1.6 times larger than the Burgers vector of threading edge dislocations (***a***-type) $\boldsymbol{b_a} = \frac{1}{3}\langle \bar{1}2\bar{1}0 \rangle$. The magnitude of a Burgers vector tells us something about the local strain field magnitude near the dislocations. Electron channelling contrast is sensitive to local elastic strain variations, and so spatially bigger features in ECCI could be associated with larger magnitude strain fields. Thus, it is thought to be the case that the larger ECCI contrast features are dislocations with a screw-type component while smaller contrast features are pure edge TDs [24]. TD distribution in GaN films usually consists of mostly edge and mixed TDs with only occasional (1%) pure screw TDs [35, 36]. Therefore, we should be able to differentiate mixed/screw TDs from edge TDs in ECCI micrographs [37].

An example of an ECCI micrograph of GaN is seen in Fig. 1.16. The bigger spots are TDs with a screw component (most likely mixed TDs). Since there are two types of Burgers vectors for screw TDs that are rotated 180° with respect to each other, $\boldsymbol{b_c} = [0001]$, and $\boldsymbol{b_c} = [000\bar{1}]$, we can expect two kinds of larger spot features (with an 180° rotation of bright-dark contrast directionality). This is, indeed, the case as can be seen in Fig. 1.16. Note also that the directionality of bright-dark contrast is perpendicular between the spatially bigger spots (~100 nm) corresponding to screw/mixed TDs, and the spatially smaller spots (~60 nm) corresponding to pure edge TDs. This observation is a consequence of their respective Burgers vectors being perpendicular to each other. [21]

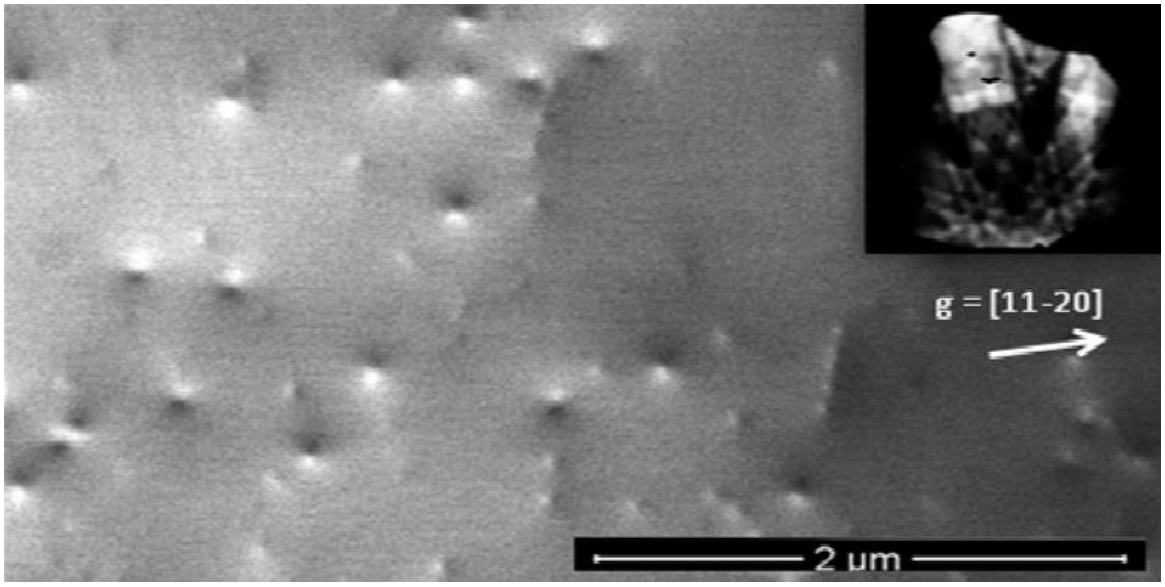

Fig. 1.16: ECCI micrograph of GaN (0002) showing the two distinguishable types of threading dislocations in GaN. The smaller bright-dark spots are pure edge TDs while the bigger spots are screw/mixed TDs. The difference in their sizes is due to the magnitude of their respective Burgers vectors. From [21].

1.4 Wet etching methods

This introductory section is largely inspired by [38].

Generally, wet etching of semiconductors functions by first oxidizing the semiconductor surface followed by the dissolution of the formed oxides. The oxidation reaction requires holes that can be supplied chemically, or by an electrochemical circuit. Wet etching of semiconductors can be divided into two main categories: electrochemical etching (anodic etching, electroless etching, and photoelectrochemical (PEC) etching, and chemical etching including conventional etching in aqueous solutions and defect-selective etching in molten salts.

In anodic etching, the semiconductor sample is connected to the positive terminal, and an inert electrode is connected to the negative terminal of a direct voltage source. Both electrodes are then submerged in an electrolyte, e.g. aqueous potassium hydroxide (KOH). An external voltage source then oxidizes the semiconductor by removing its bonding electrons (injecting holes) from its surface bonds. The formed oxides are then dissolved in the electrolyte.

In electroless etching, the semiconductor is oxidized by the potential of an oxidizing agent in the electrolyte, which removes valence-band electrons from the semiconductor, effectively donating holes. This method is possible only when the redox potential is higher than the potential of the semiconductor sample in equilibrium with its ions in the solution.

In PEC etching, semiconductors are etched under illumination with an energy that is higher than the bandgap energy (E_g) of the semiconductor (for GaN it is ultraviolet (UV) light). The mechanism of PEC etching is following. The semiconductor acts as an anode and a metal counter electrode is used as a cathode. The electrodes are in electrical contact, and they are placed in an electrolyte. Electron–hole pairs are created in the semiconductor by photons from the UV illumination source. The photogenerated holes oxidize the semiconductor surface while the photogenerated electrons are used by a reduction reaction occurring on the cathode. The two competing processes deciding the etch rate in PEC etching are: the amount of absorbed incident optical radiation, which increases the number of holes at the surface of the semiconductor, and the recombination of electrons and holes, which slows down the etching process.

Chemical etching is very different from the above-mentioned methods because no free carriers or electrolyte are used in it. Chemical etching works by exposing the semiconductor surface to a reactive etchant that breaks the chemical bonds of the semiconductor and creates oxides from it, which are then dissolved in the etchant. In the case of GaN, defect-selective chemical etching, which will be further described in the next section, and chemical etching in aqueous solutions have been commonly used for defect characterization, polarity identification, and patterning.

1.4.1 Defect-selective etching of GaN

For nitrides like GaN, the development of defect-selective etching methods lagged behind the use of different methods for its structural characterization (mainly TEM) due to the high chemical resistance, and polarity-dependent strong anisotropy of etching of GaN. Additionally, most grown GaN heteroepitaxial layers have a very high dislocation density (DD) of up to 10^{10} cm^{-2}. There are also many other different

types of defects in GaN like nano-pipes, pinholes, and inversion domains. All of these factors combined make the development of a solid and universal defect-selective etching procedure quite difficult [2].

The main method for obtaining the dislocation density of thin films has been TEM for quite a long time. Unfortunately, TEM is not ideal for routine use due to its time-consuming sample preparation. Defect-selective etching can be used as a possible alternative to TEM for the quick estimation of the defect density of samples [2]. However, GaN is resistant to most acids and bases used at temperatures up to 75˚C [39]. Nonetheless, we will focus on two approaches which were shown to be successful in revealing defects in GaN by selective etching: (i) etching in acids [40, 41] or bases [42, 43] at high temperatures (so-called orthodox method) and (ii) PEC etching in aqueous KOH solutions at room temperature and under UV illumination [44].

The defect-selective etching of GaN in either acids, or bases at high temperatures can be described as orthodox etching because the etching process results in the formation of hexagonal etch pits at the surface positions of threading dislocations as seen in Fig. 1.17. These hexagonal pits reflect the crystallographic symmetry of the GaN lattice (HCP). The commonly used acids include H_2SO_4, H_3PO_4, and their mixture (known as HH etch). The used bases are molten KOH, molten NaOH, and their eutectic mixture (E etch), which has a significantly lower melting point (170 °C compared to >320 °C for both NaOH and KOH separately). This eutectic mixture is sometimes also mixed with MgO (E+M etch) to increase the viscosity of the mixture to allow only local etching. [38] The defect selectivity comes from the fact that e.g. threading dislocations cause a local increase in the surface energy of the crystal, and since the rate limiting step seems to be surface kinetics, etching is significantly more prominent on dislocations than the defect-free surface. [2]. Additionally, it is possible to find out the polarity of a given sample by orthodox etching because e.g. hot H_3PO_4 readily etches N-polar GaN films, resulting in big differences in the surface morphology. On the other hand, only the defect sites in Ga-polar films are etched away by the acid, forming nanometre-scale pits while keeping the defect-free GaN intact [45]. The etch pit density (EPD), under correct etching parameters, has been shown to be consistent with atomic force microscopy (AFM) and TEM measurements of dislocation density [46]. The ideal etching parameters depend on the crystal polarity, defect type and their distribution. [38]

PEC etching forms protruding pillars at the positions of dislocations as seen in Fig. 1.18. These protruding features, often called whiskers, are formed by PEC etching due to the nonradiative recombination of the photogenerated electrons and holes on the dislocation sites mostly in *n*-GaN samples, which prevents the etching of these locations [47]. Meanwhile, the dislocation-free material between the dislocation sites is etched away, resulting in only the whiskers being untouched. This is very convenient for studying these defects as they are left intact and can be studied by different methods. TEM measurements of PEC etched GaN showed that these whiskers really do correspond to dislocations [44]. Because the lateral sizes of these whiskers are usually <100 nm, in large FoV SEM images, they appear as dots. The dislocation density can then be estimated by counting the number of dots and dividing it by the size of the imaged area. The whisker densities estimated by SEM were shown to be comparable to the densities obtained by both AFM [48] and TEM [46] measurements. The characterization of dislocations by PEC etching is not really possible since the whiskers are not distinguishable from

one another, and therefore only the total dislocation density is obtainable from PEC etching [49]. PEC etching does not seem to be dependent on the crystal polarity of GaN [50]. Finally, there is a second possible regime in PEC etching of GaN, which occurs when the concentration of the KOH solution is low (<0.01 M [51]), thus diffusion becomes the rate-limiting step, resulting in polishing-like behaviour and the loss of defect selectivity [2].

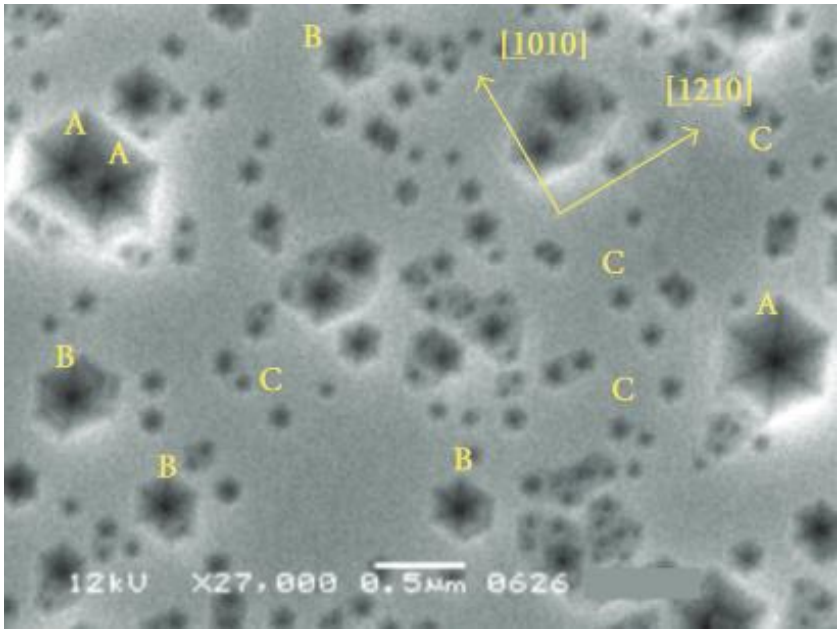

Fig. 1.17: Surface of a HVPE GaN epilayer after 2 min of etching in KOH/NaOH eutectic mixture at 540 °C. The A pits correspond to screw dislocations (their EPD is 2.8×10^7 cm^{-2}), the middle-sized B pits to mixed dislocations (1.2×10^8 cm^{-2}), and the smallest C pits to edge dislocations (8.7×10^8 cm^{-2}). From [52].

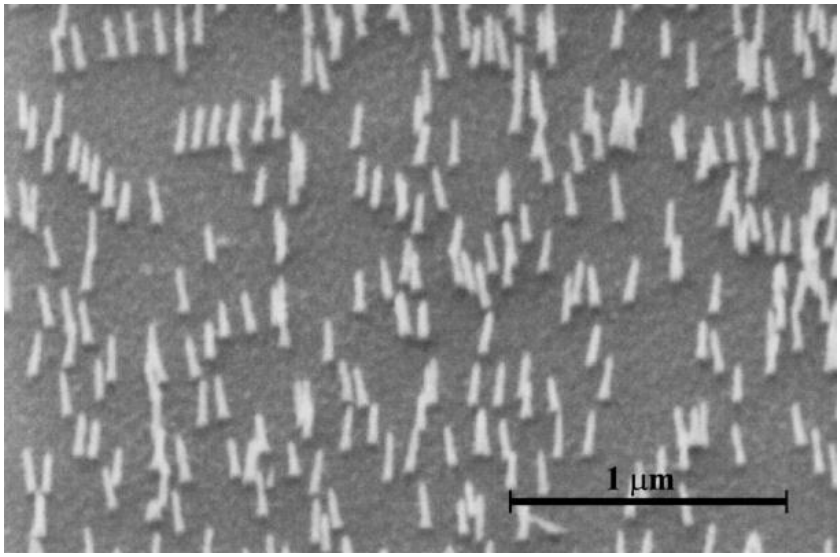

Fig. 1.18: SEM micrograph of a n-GaN surface after 15 min of PEC etching. The white structures are called whiskers, which are formed on dislocations during the etching process. They have typical diameters of 25 nm, lengths of ~150 nm and their density is of the order of 10^9 cm^{-2} – same as for the dislocation density. From [44].

1.4.2 Etch pits in GaN

We will focus mostly on the conventional etching methods, specifically etching in eutectic mixture of KOH and NaOH (E-etching), as it is simpler to do since the equipment needed to perform them is likely available in most chemical laboratories. In addition, by using these methods, it is possible to identify the various dislocations based on the difference in size of the etched features in contrast to PEC etching, which only tells us about the total dislocation density.

As seen in Fig. 1.17, under ideal conditions during E-etching of GaN, three differently sized etch pits, corresponding to the three common types of threading dislocations in GaN, are formed, as was confirmed by TEM [53]. For the etching parameters used in Fig. 1.17, the sizes of these pits are approximately following: the largest pits (screw TDs) are ~750 nm across, medium pits (mixed TDs) are ~375 nm across, and the smallest pits (edge TDs) are <150 nm across. The concrete sizes of the etch pits depend on the etchant, etching temperature, and etching time, so the important takeaway is that the there is a clear difference in the size of the pits, which can tell us which type of TDs were etched. Additionally, there can also be another, even larger, etch pit (several μm across in [52]) formed on nanopipes (open-core screw dislocations) as seen in Fig. 1.19. This difference in the size of the etch pits can be explained by the following line of thinking: "*The thermodynamics of the etching process predicts that the change of the chemical potential during formation of the etch pits is inversely proportional to the energy of the defects; therefore, defects of larger energy (larger magnitude of Burgers vector) will be etched easier (or at lower temperature)*" [54]. As a result, we expect nanopipes and then screw/mixed TDs to be etched more readily (or at lower temperatures), followed by them developing into larger pits, while edge TDs should be more resistant to chemical etching [49]. This was, indeed, seen in some studies conducted at lower etching temperatures, where only etch pits corresponding to nanopipes, which have the biggest Burgers vector compared to the other TDs, were observed [55]. Considering this, a choice of an etching temperature, which is between the temperatures needed to etch different types of TDs, can be made to deliberately choose only which type of TDs will be etched. Indeed, this was observed, when etch pits were formed on nanopipes and mixed dislocations, while leaving edge dislocations intact [50].

However, there is one seemingly unexpected observation in Fig. 1.17, in which the largest pits, excluding nanopipe etch pits, do not correspond to mixed dislocations, as would be expected, but rather to screw dislocations, which have a smaller Burgers vector and thus smaller elastic energy than mixed dislocations in wurtzite GaN. This inconsistency could be possibly resolved by considering that the decoration of TDs by point defects such as impurities, doping atoms and/or native defects can result in a strain release and a drop in elastic energy of the TDs. The extent of decoration is expected to be dependent on the edge component of the Burgers vector. Therefore, by taking this effect into consideration, we can explain the formation of larger sized pits on screw than on mixed TDs as well as the small size of pits formed on edge TDs [53].

Finally, the etch pit density does not always correspond to the threading dislocation density (TDD). This can be, among other factors, caused by the merging of neighbouring pits known as overetching. Overetching can be caused either due to etching under a higher temperature, or for a longer time. Therefore, overetching can lead to the underestimation of TDD due to the fact that merging of

many etch pits decreases the EPD, which is used as the estimation parameter. Additionally, overetching might cause difficulties when estimating the density of individual types of dislocations as they may be indistinguishable from each other when merged into a larger pit [49].

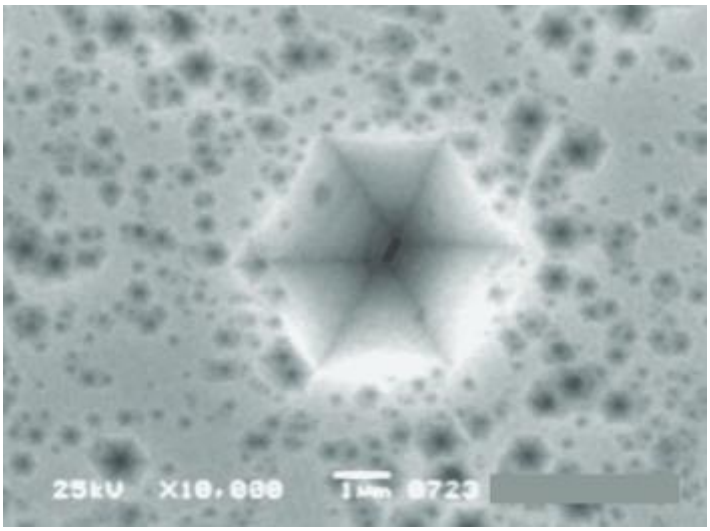

Fig. 1.19: Etch pit corresponding to a nanopipe (open-core screw dislocation) in HVPE GaN epilayer after 7 min of etching at 580 °C in EI-flux (E-etch with <5 mole% level of NaCl). The submicron-scale opening (open core) is seen at the bottom of the etch pit. From [52].

2 Experimental part

From the theoretical part, we know about the importance of studying threading dislocations in GaN epitaxial layers, and the techniques that can be used to study them. In this chapter, the process of carrying out three such techniques – ECCI, defect-selective etching, and TEM diffraction-contrast imaging – in addition to FIB lamella preparation, will be discussed along with their experimental results.

2.1 Samples and equipment used

For most experiments, we used a sample originally from onsemi, a lamella of which, illustrating its composition, is seen in Fig. 2.1. It was said to be composed of Si substrate, 200 nm buffer layer of AlN and 800 nm heteroepitaxial layer of GaN.

ECCI micrographs made by me were taken with SEM MIRA3 XMU (TESCAN) at CEITEC. The ECCI micrographs in Fig. 2.4 were taken in cooperation with Ing. Martin Čalkovský, Ph.D from TFS on their Apreo 2 SEM. Etching in molten bases was done in a chemical laboratory in A2/518 at the IPE FME BUT campus. FIB lamella preparation was done with dual-beam FIB/SEM FEI Helios NanoLab 660 at CEITEC. Finally, TEM micrographs were taken with FEI Titan Themis 60-300 cubed at CEITEC by Ing. Eva Kolíbalová, Ph.D.

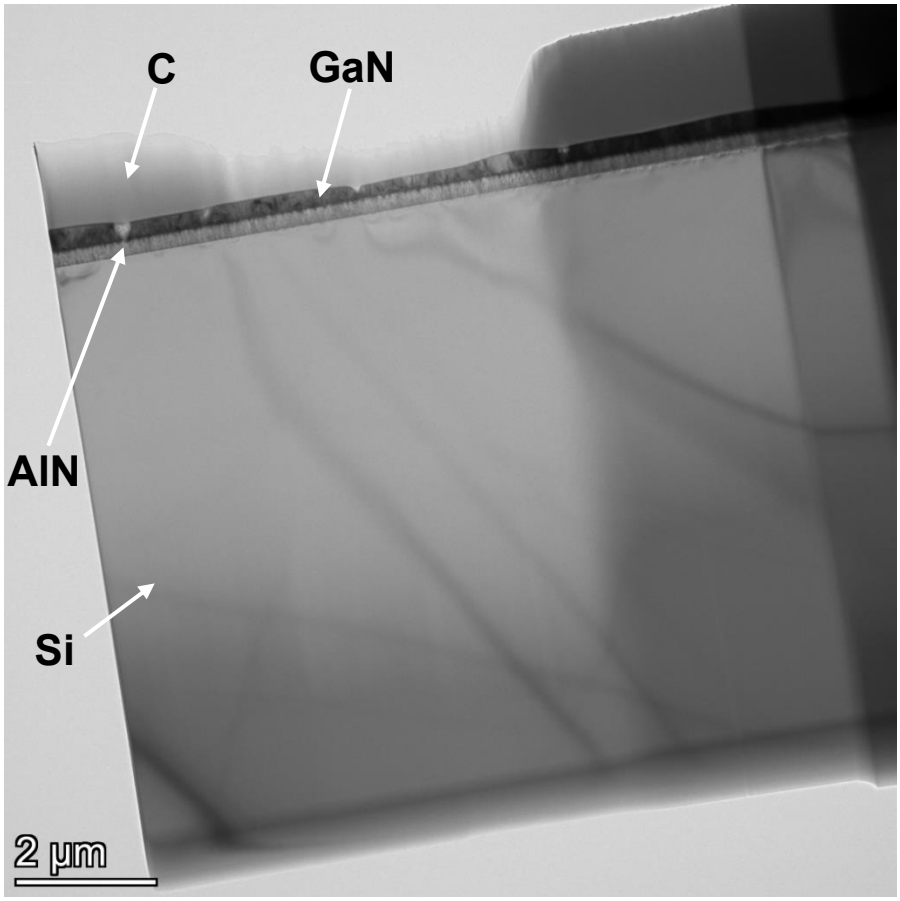

Fig. 2.1: TEM micrograph of a lamella from our sample with clear layer separation from top to bottom: carbon (deposited during lamella preparation), GaN epitaxial layer, AlN buffer layer, Si substrate. The lines in the Si substrate are bend contours.

2.2 ECCI measurements

First, an establishment of the ideal *HV*, based on the appearance of the ECP in *channeling mode* available on MIRA as shown in Fig. 2.2, was made. The best detail, sharpness of the bands, and extent of the ECP is observed for *HV* = 20 kV.

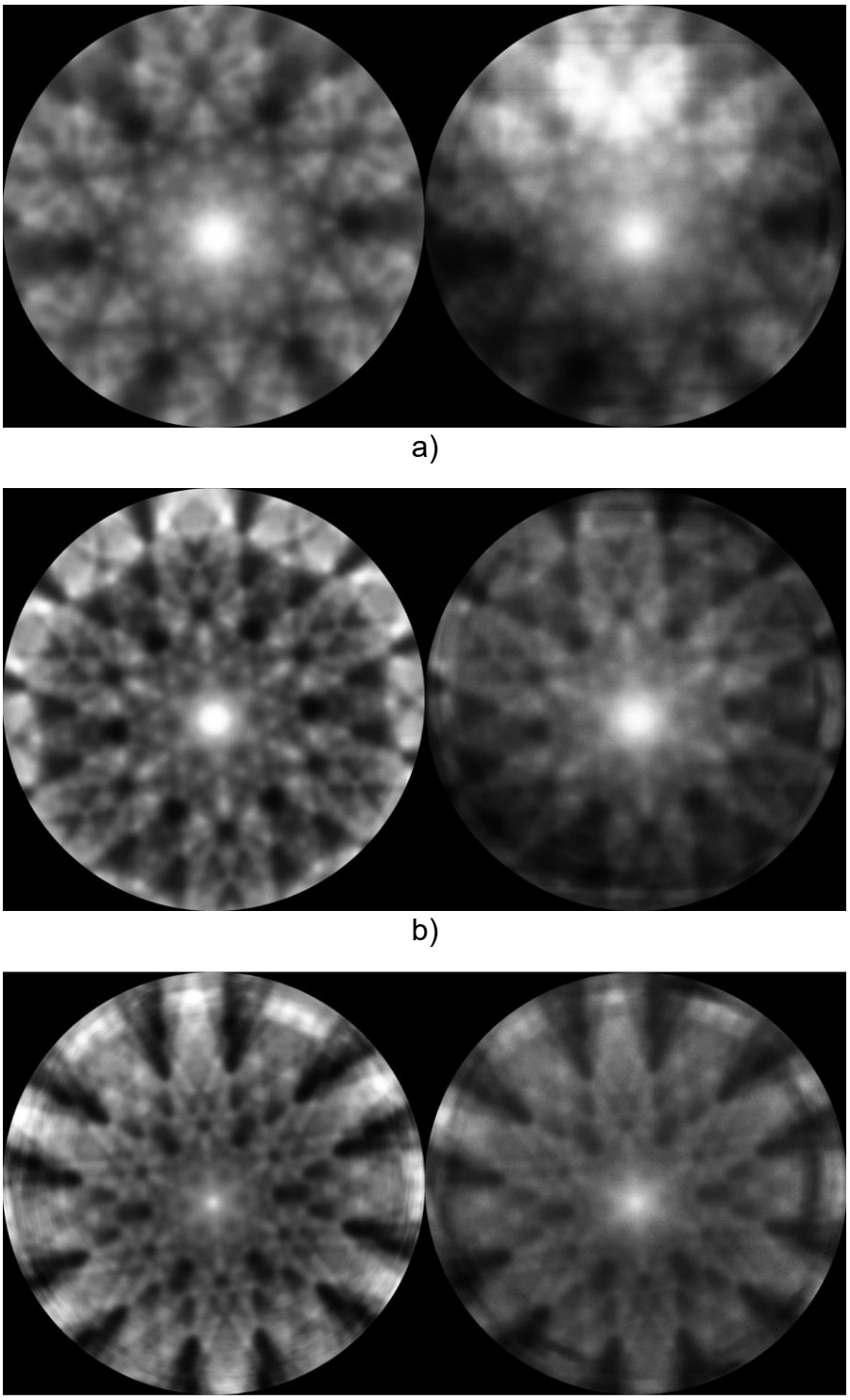

Fig. 2.2: *'Rocking beam'* ECP quality dependence on *HV* for *a*) *HV* = 5 kV, b) *HV* = 10 kV, and c) *HV* = 20 kV. The left ECP is from BSE signal while the right one is from SE signal. The angular range of the ECPs is ±11°.

Second, the effect of working distance (WD) on the width and sharpness of the edges of the channeling bands in the ECP was determined, as seen in Fig. 2.3. The best quality image is obtained for the lowest WD, which is ideal also for ECCI.

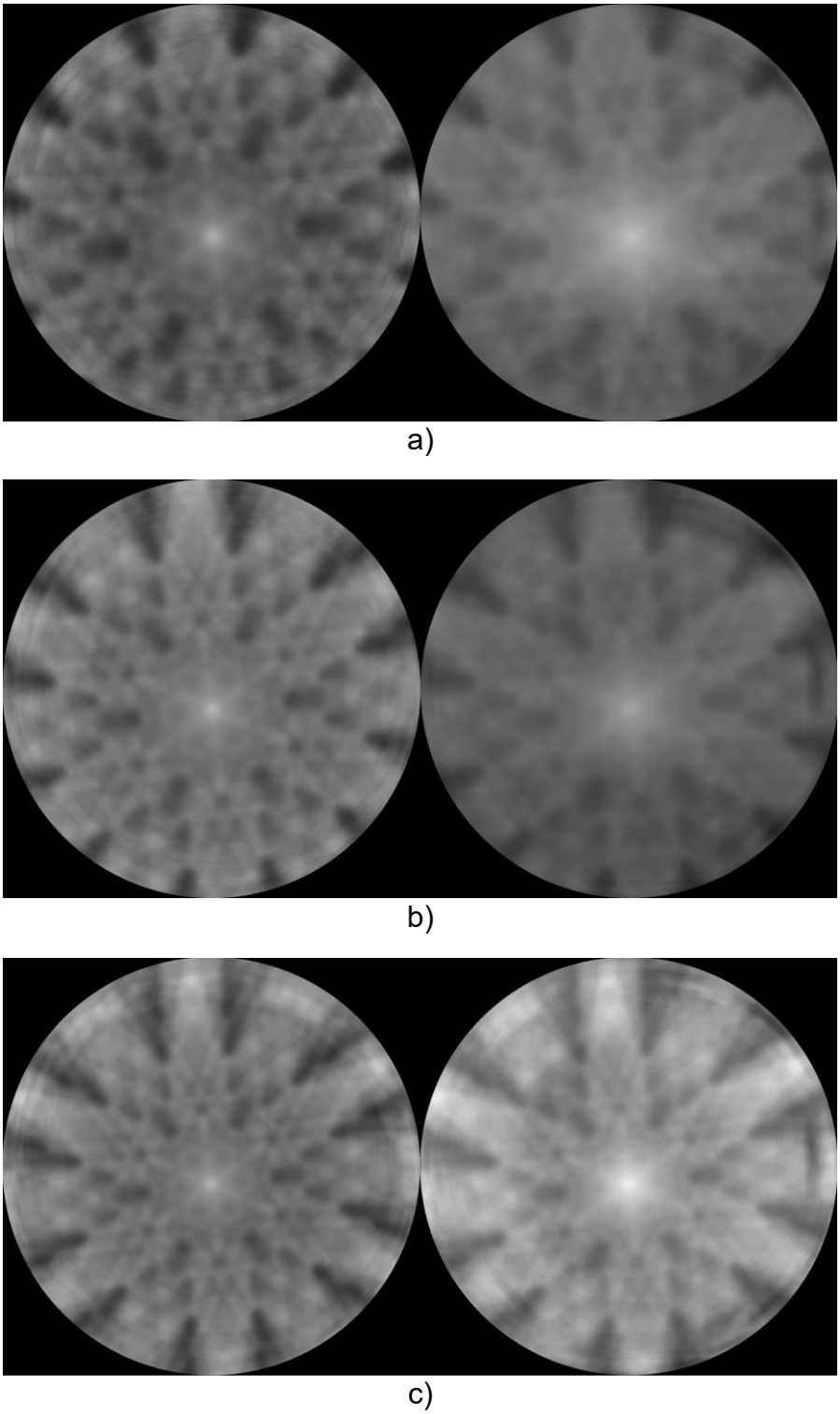

Fig. 2.3: *'Rocking beam'* ECP band width dependence on WD for a) WD = 15 mm, b) WD = 12 mm, and c) WD = 9 mm. The bands get narrower and sharper as the WD is decreased, thus it is easier to find the correct channeling condition for a lower WD. The left ECP is from BSE signal while the right one is from SE signal. The angular range of the ECPs is ±11°.

Third, the ideal imaging conditions from above, in addition to the other parameters as high probe current, slow scan times and/or frame/line integration to improve SNR are now established. With this knowledge, ECCI micrographs were taken, first, in cooperation with Ing. Martin Čalkovský, Ph.D from TFS on Apreo 2, because this SEM obtained very good micrographs, which are shown in Fig. 2.4.

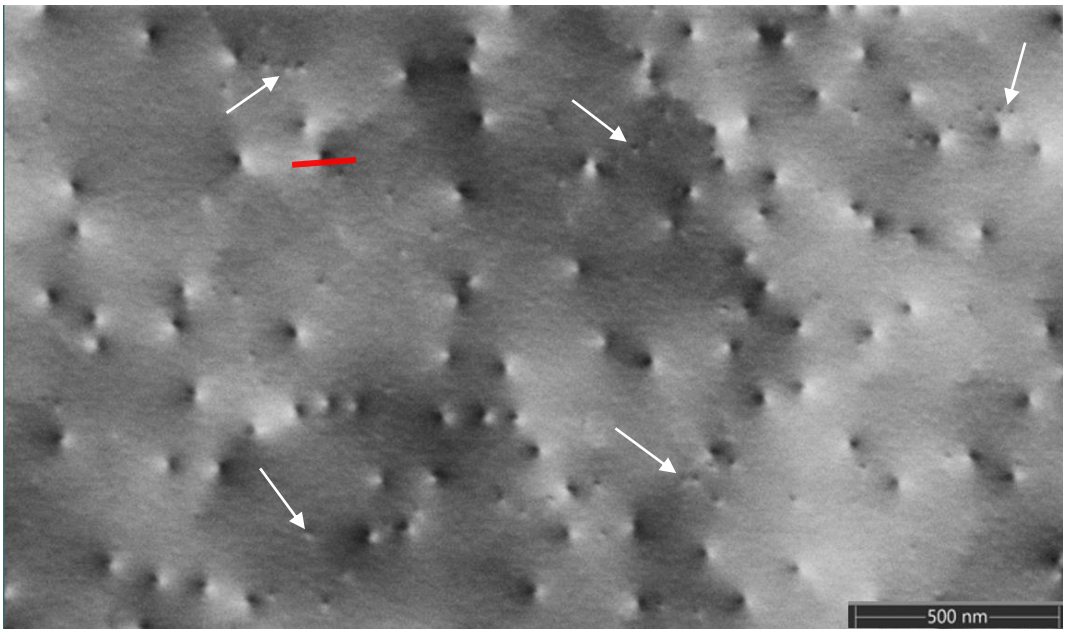

a)

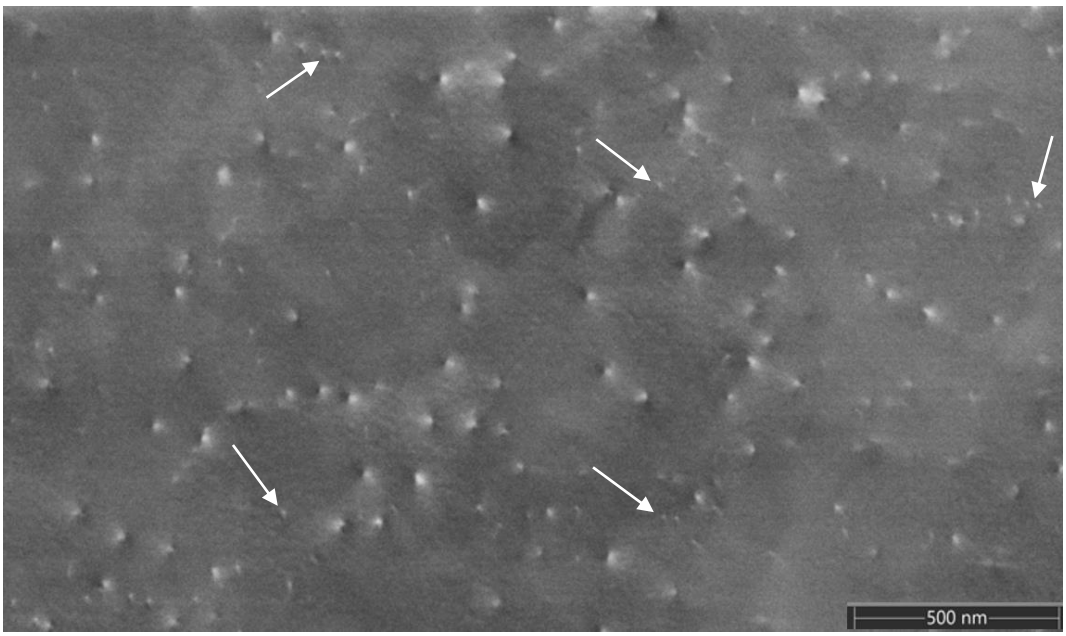

b)

Fig. 2.4: ECCI micrographs of the same position of our GaN sample for two channeling conditions ***g*** with opposite Miller indices. Most dislocations are screw/mixed (big spots), but some pure edge dislocations are highlighted by arrows. a) Channeling condition from the $\{11\bar{2}0\}$ family of planes and b) opposite channeling condition to a). See the 180° rotation of bright-dark contrast between a) and b), which is noticeable for the big spots. Courtesy of Martin Čalkovský (TFS).

It is sometimes also possible to know the precise diffraction condition ***g*** used for ECCI. This can be done, for example, by producing an EBSD pattern for a given sample and then simulating an EBSD pattern for 0° tilt (because EBSD is done at 70° tilt and ECP for 0° tilt, and there is some kind of reciprocity between these two techniques [21]). Since EBSD patterns are easily indexed by many computer programs, the specific diffraction condition ***g*** can then be established by comparing the simulated EBSD pattern with the measured ECP. Another option is to know the orientation of some of the edges of the sample, e.g. when the sample is cut from a wafer with a known orientation. Then, by aligning the *wide-field* ECP with the edge of a known orientation, it is possible to index the ECP from a known ECP map of a given crystal structure. Unfortunately, neither of these options was easily available to us, nor, frankly, really needed because our goal was not to find the Burgers vector of the TDs. As we know, this is not even really possible to do by ECCI due to the surface relaxation effects of TDs [24]. Therefore, the only thing that we can say about the diffraction condition used in Fig. 2.4. is that we used the $\{11\bar{2}0\}$ family of planes rather than the $\{01\bar{1}0\}$ family of planes. This is because the $\{11\bar{2}0\}$ family of planes does not have another set of planes directly underneath the edge of their band in the ECP, in comparison to the $\{01\bar{1}0\}$ family of planes, as can be seen in Fig. 1.11. Consequently, making the correct choice between these two families of planes should result in a better contrast of the TDs.

The typical bright-dark contrast of dislocations, which is achieved for ideal alignment of the optical axis with the edge of a channeling band, is represented in Fig. 2.5. It shows a graph of signal intensity variation along a red line over a screw/mixed dislocation from Fig. 2.4. For the opposite diffraction condition, the graph would just flip around representing a dark-bright contrast.

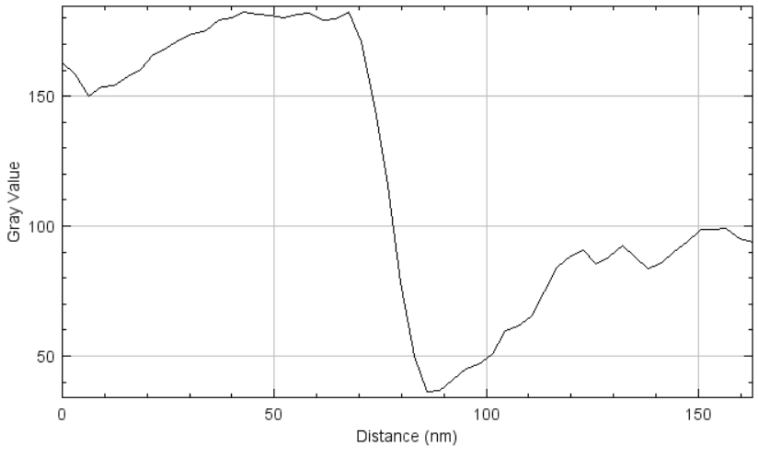

Fig. 2.5: Signal intensity variation along the red line in the ECCI micrograph in Fig. 2.4 a), representing the typical bright-dark contrast of TDs in ECCI.

An example of an ECCI micrograph from MIRA3 is seen in Fig. 2.6. The contrast is noticeably worse than for Fig. 2.4., but it is still good enough to see two types of contrast spots (edge and screw/mixed TDs). Additionally, the FoV is twice as large as in Fig. 2.4., causing the smaller spots to be harder to be identified. The focus and stigmators are ideally set up for the best resolution. Even the slightest misalignment from the ideal channeling condition results in a significantly worse contrast. Lastly, the brightness must be very low, and the contrast must be as high as possible to even be able to see the spots. The image quality was then improved in post-processing.

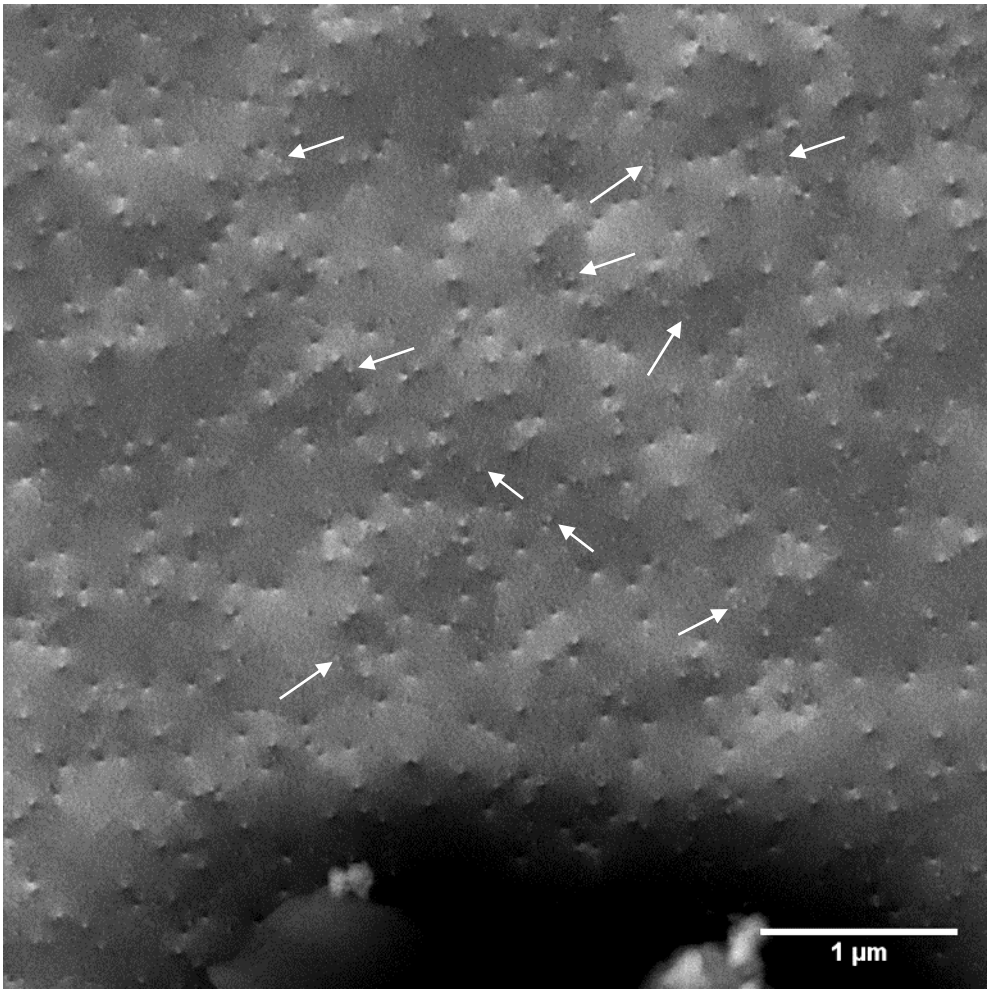

Fig. 2.6: One of the best ECCI micrographs obtained on MIRA SEM. Some edge TDs (highlighted by arrows), despite their size, are quite well visible. The other spots are screw/mixed TDs. On the bottom there is, on purpose, some contamination for easier localisation of the position when aligning the sample to the correct channeling condition.

2.3 Wet etching in KOH/NaOH eutectic alloy

Etching of our sample was done in KOH/NaOH eutectic alloy (denoted as E-etch), which has its phase diagram in Fig. 2.7. Specifically, both components were in solid (pellet) form, and we weighed them in the following amount:

$$m_{\mathrm{KOH}} = 4.07\ \mathrm{g}, \text{ and } m_{\mathrm{NaOH}} = 6.00\ \mathrm{g}. \tag{2.1}$$

Their molar masses *M* are:

$$M_{\mathrm{KOH}} = 56.11\ \mathrm{g/mol}, M_{\mathrm{NaOH}} = 40.00\ \mathrm{g/mol}. \tag{2.2}$$

Thus, the number of moles *n* of each component are:

$$\begin{aligned} n_{\mathrm{KOH}} &= \frac{m_{\mathrm{KOH}}}{M_{\mathrm{KOH}}} = \frac{4.07\ \mathrm{g}}{56.11\ \mathrm{g/mol}}\ 0.07\ \mathrm{mol}, \\ n_{\mathrm{NaOH}} &= \frac{m_{\mathrm{NaOH}}}{M_{\mathrm{NaOH}}} = \frac{6.00\ \mathrm{g}}{40.00\ \mathrm{g/mol}}\ 0.15\ \mathrm{mol}. \end{aligned} \tag{2.3}$$

Then, the mole fraction χ of each component is:

$$\chi_{\mathrm{KOH}} = \frac{n_{\mathrm{KOH}}}{n_{\mathrm{KOH}} + n_{\mathrm{NaOH}}} = \frac{0.07\ \mathrm{mol}}{0.07\ \mathrm{mol} + 0.15\ \mathrm{mol}} = 0.32,$$
$$\chi_{\mathrm{NaOH}} = \frac{n_{\mathrm{NaOH}}}{n_{\mathrm{KOH}} + n_{\mathrm{NaOH}}} = \frac{0.15\ \mathrm{mol}}{0.07\ \mathrm{mol} + 0.15\ \mathrm{mol}} = 0.68. \quad (2.4)$$

Finally, the mole percentage of each component is:

$$\mathrm{Mole\ \%\ KOH} = \chi_{\mathrm{KOH}} * 100\ \% = 0.32 * 100\ \% = 32\ \mathrm{mol\ \%},$$
$$\mathrm{Mole\ \%\ NaOH} = \chi_{\mathrm{NaOH}} * 100\ \% = 0.68 * 100\ \% = 68\ \mathrm{mol\ \%}. \quad (2.5)$$

The melting point of this eutectic mixture, according to Fig. 2.7., is around 230 °C.

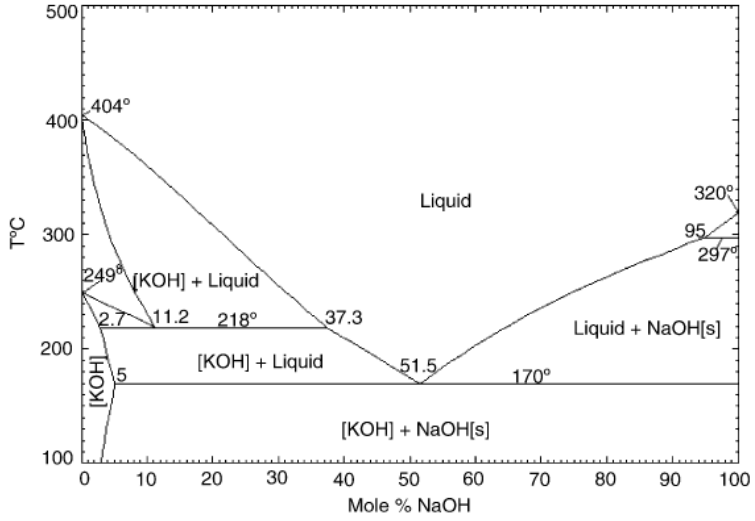

Fig. 2.7: Phase diagram of KOH/NaOH eutectic alloy. The eutectic point is at 51.5 mole % of NaOH in KOH, which then has a melting point of 170 °C. From [56].

After we weighed both components, we put them in the same glass beaker and then poured in about 10 ml of purified water to dissolve them. Additionally, after the components were already dissolved, the beaker was put on a heating plate, inside a fume hood, and heated up to around 200 °C to evaporate all the water. The heating plate was then heated up to 240 °C so that the eutectic was melted. The exact temperature of the eutectic was not determined as we did not have any means to do that, but we waited for 10 min after the heating plate reached 240 °C, and the eutectic was clearly in liquid form. During all the previous steps, the eutectic was regularly stirred so that it stayed homogeneous. After everything was ready, we held our sample with a pair of tweezers and submerged it into the molten eutectic for 30 seconds. Then, we immediately put the sample in another beaker filled with purified water for a while, to clear the surface from any remaining etchant.

Now, concerning the etching temperature and etching time used in the case of the eutectic mixture. The values we used were very different from the ones used in literature. To name a few: 450 °C for 3 min [57], 540 °C for 2 min and 3 min [52], 420 °C for 2 min [2], 200 °C for 3 min [50]. In the next paragraphs, our thinking process behind the choice of the etching parameters we used is described in detail.

Concerning the choice of the etching time first. We determined the ideal etching time for our samples from our previous etching experiments and

observations of the resulting etch pits in an SEM. For etching times above 30 s, larger areas of the sample surface were getting noticeably etched away. Therefore, to keep most of the sample surface unetched, we chose the etching time to be 30 s, for which the surface was kept relatively intact, of course, apart from the etch pits at TDs. Besides, as we already know, etching time should only impact the absolute size of the pits, and not the relative size differences between the pits corresponding to different types of TDs. However, using short etching times may cause, e.g. the small pits, corresponding to edge TDs, to be difficult to spot due to them not having enough time to grow [49]. On the other hand, etching for too long might cause overetching. Either way, we were mostly focused on observing the different sizes of pits for different TDs, and not with precisely counting the EPD. Therefore, we determined that it would not cause any issues to etch our samples just for 30 s, when the results we observed in the SEM were satisfying enough.

Now, concerning our choice of the etching temperature. Our heating plate had an upper limit of around 350 °C, so it would not be possible to achieve most of the temperatures used in the literature above, for the sake of comparison. The lower limit was set by the mole percentage of NaOH in the eutectic. While it was possible to reduce our temperature down to 170 °C, we did not attempt this because, due to our choice of etching time, it would again not be possible to exactly compare our results to the other studies. Additionally, the etching temperature can vary wildly depending on the sample (even for samples grown with the same growing method), e.g. (360-480) °C for HVPE-grown samples from different suppliers [53]. The etching temperature is the determining factor for which types of TDs can be etched, e.g. edge dislocations might not produce etch pits because they need a higher temperature [50]. However, we concluded that if we see good enough results in the SEM, then we would not tamper with the etching temperature.

The idea behind including etching in this thesis was to, maybe, correlate the size of the spots in ECCI with the size of the etch pits. To do this, some fiducial markers (patterns of FIB milled holes) were made on the sample. Then, ECCI was carried out at spots in the vicinity of these markers. Afterwards, the sample was etched, and we tried to observe the same spots in the SEM. Unfortunately, the etching was significant even at the markers, which made it very difficult to find the exact same spots. Additionally, the small FoV used for ECCI images (2.5-5) μm made the task even more difficult. Lastly, even for our relatively low etching time and temperature, some of the etch pits were very large (~1 μm – Fig. 2.10) so, ultimately, the correlation of ECCI with etching was impossible for us to do.

However, we still observed something interesting in the SEM post-etching. First, we tried to carry out ECCI and the result is seen in Fig. 2.8. Notice the etch pits, but also that there are still many visible TDs in the left BSE micrograph. This indicates that, indeed, our etching temperature might have been too low, as etch pits were not formed on many dislocations (probably mostly mixed and edge TDs).

Second interesting observation, which was seen specifically near the fiducial markers, is shown in Fig. 2.9. Notice that the pits do not have the same size near the milled holes as further away (>20 μm) from them. This observation is better illustrated by comparing Fig. 2.10 with Fig. 2.11. One logical explanation we have is that a lot of strain was induced in the vicinity of the holes during their milling by the focused ion beam. The strain was then relaxed by creating new dislocations (probably mostly nanopipes due to the size of the pits, as seen in Fig. 2.10). However, this explanation is not stated with any degree of certainty due to us being a little ignorant about this.

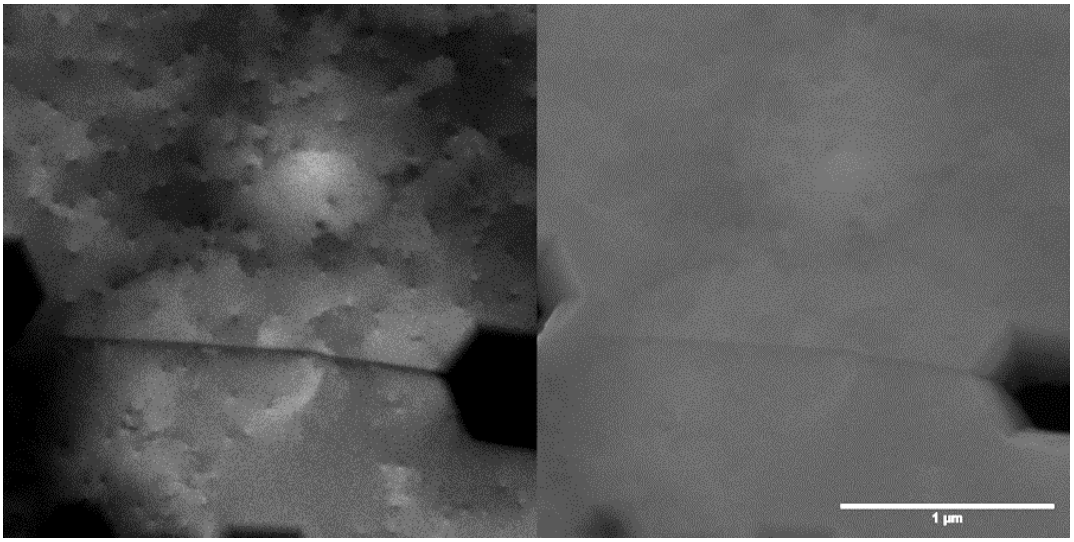

Fig. 2.8: ECCI micrograph done after etching (see etch pits). The left half is from BSE signal and the right half is from SE signal. Notice that there are still many unetched TDs visible in the BSE micrograph.

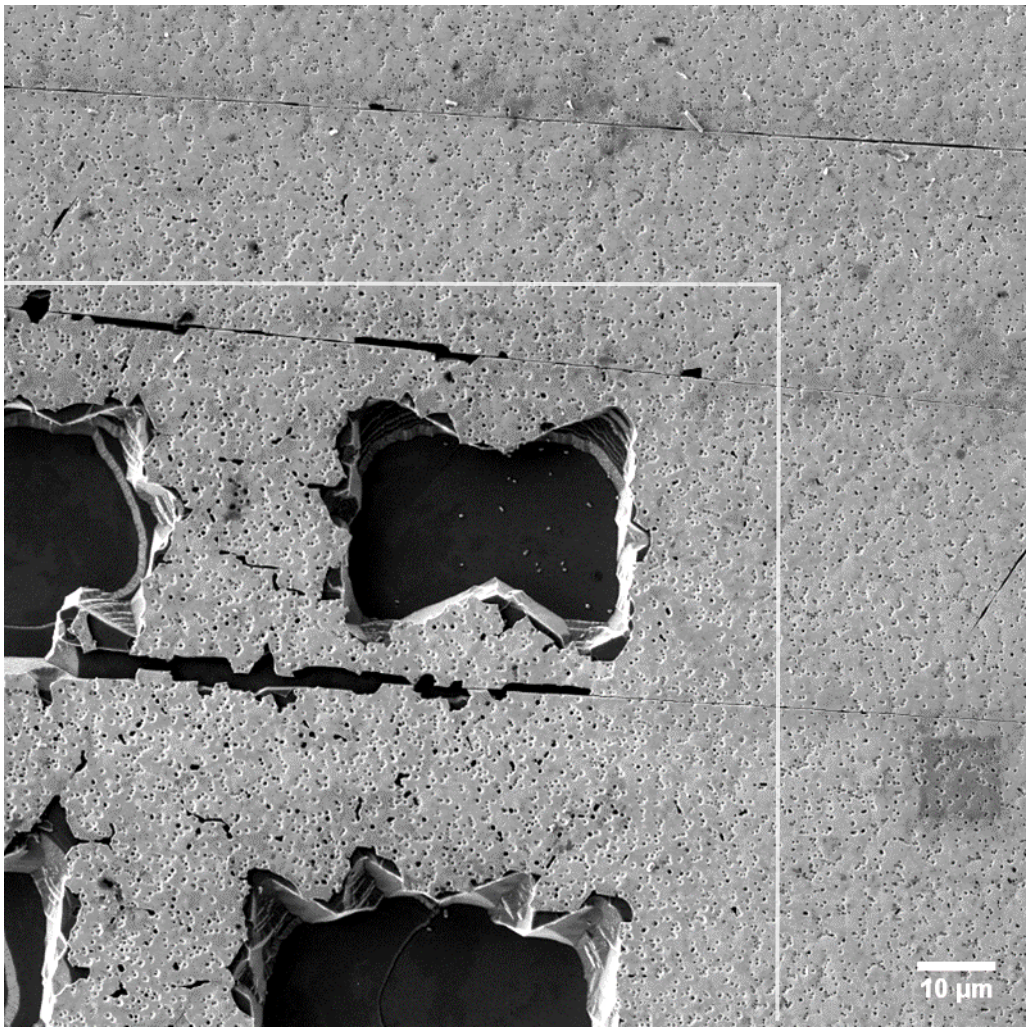

Fig. 2.9: SE micrograph of the etched sample. Notice the bigger etch pits in the immediate vicinity of the milled holes (up to ~20 µm away from the holes, as highlighted by the white lines), and smaller etch pits further away from them.

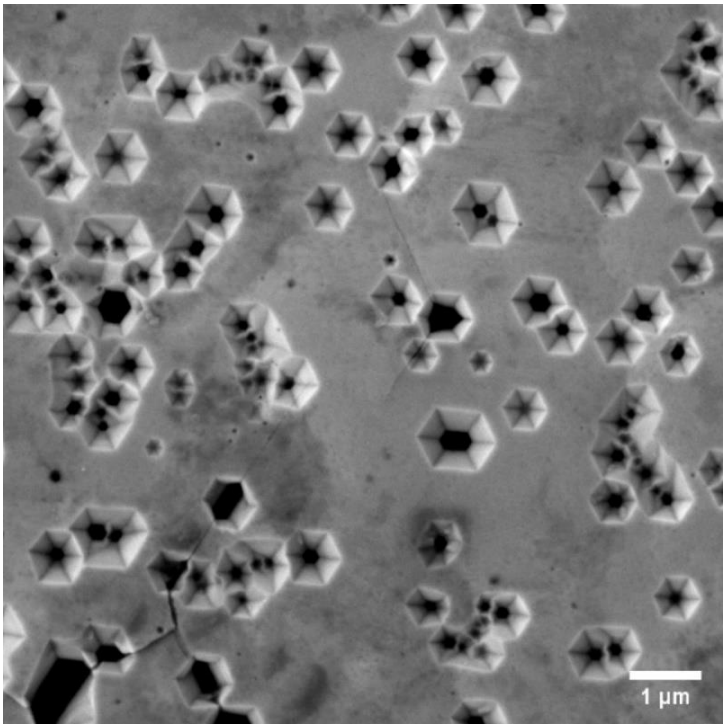

Fig. 2.10: SE micrograph taken near the milled holes in Fig. 2.9. The etch pits are way bigger than the ones in Fig. 2.11. It might be that the FIB milling resulted in the formation of dislocations (looks like mostly nanopipes, judging from the sizes of the pits, but this is not stated surely due to us being a bit ignorant about this topic).

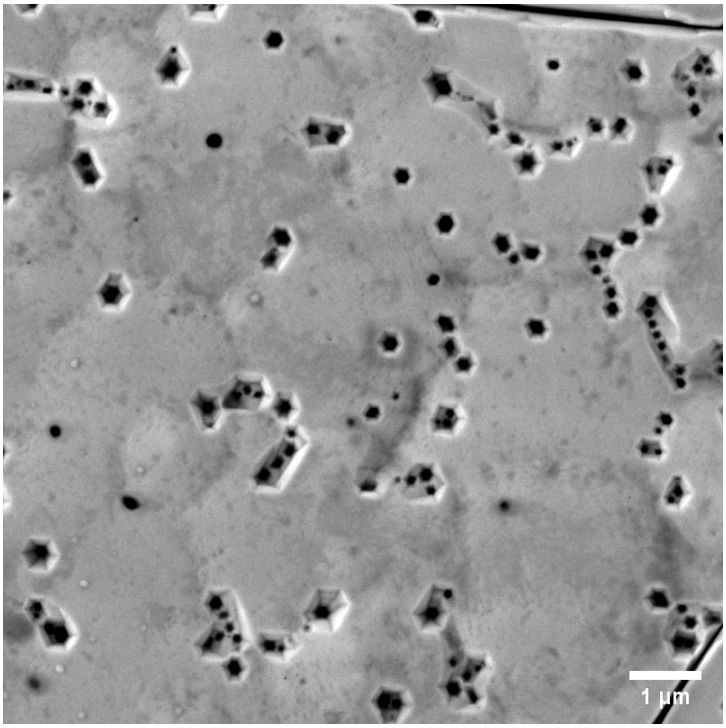

Fig. 2.11: SE micrograph taken further away from the milled holes in Fig. 2.9. The etch pits are way smaller than the ones in Fig. 2.10. Notice that almost all pits have relatively the same size (probably screw TDs) – most likely the etching temperature was not high enough for the etching of the other types of TDs (mixed and then edge TDs).

2.4 FIB lamella preparation

In the context of material science, a lamella is a thin, plate-like structure extracted from a sample for further examination. Mostly, the term is used when referring to an electron-transparent thin foil obtained from a sample to be able to analyse it in a TEM. Nowadays, the most common method of obtaining a lamella is by using a focused ion beam (FIB) in combination with the high-resolution imaging capabilities of SEM, as seen in Fig. 2.12. In this section, a short walk-through of the process of obtaining a lamella from our etched sample is presented.

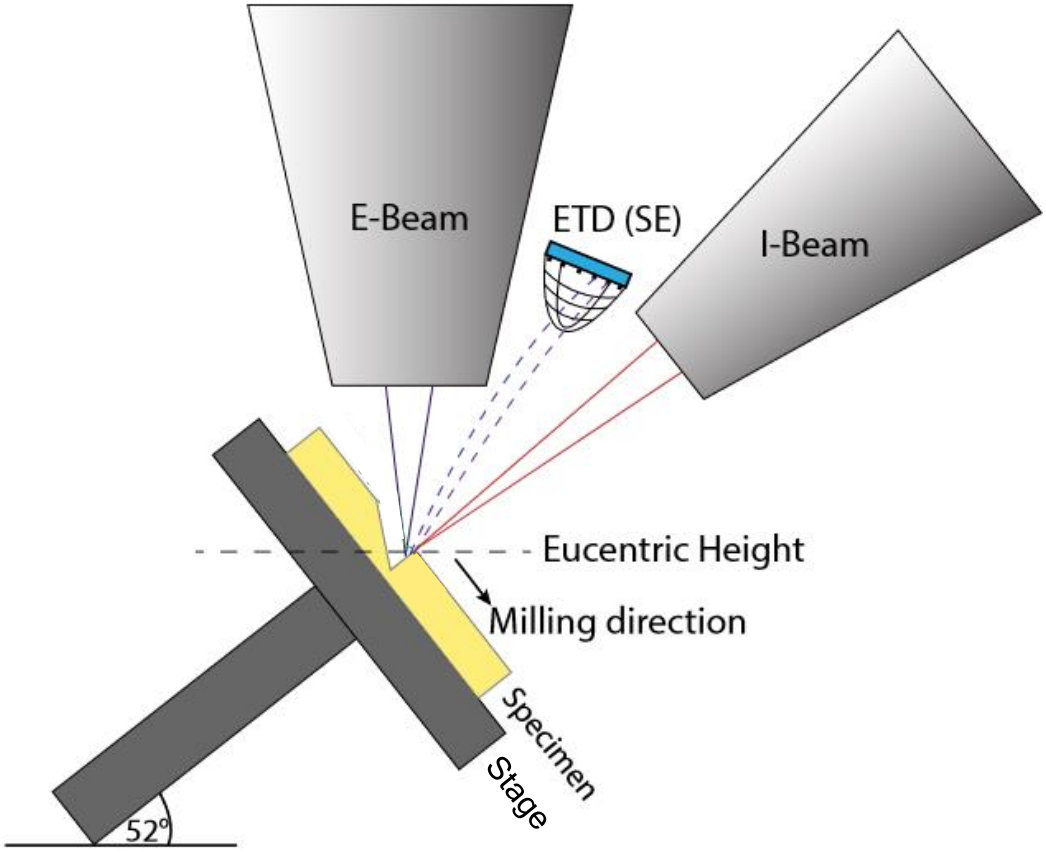

Fig. 2.12: A schematic of a FEI HELIOS dual-beam setup for FIB lamella preparation. The ion beam column is tilted by 52° away from the electron beam column. Using secondary electrons, collected by the Everhart-Thornley detector (ETD), micrographs can be made during milling by the ion beam. Eucentric height is the stage position, for which the view field does not change during tilting of the stage. Adapted from [58].

Specifically for our experiments (TEM diffraction-contrast imaging), it is advantageous to cut the lamella at a specific angle relative to the sample. To do this, we use the ECP formed in the *wide-field* mode of the MIRA3 SEM as shown in Fig. 2.13. The desired orientation is for the lamella to be perpendicular to the highlighted band as illustrated. Since the lamella is cut in the horizontal direction, the band should be vertical. In our case, a -30° rotation of the sample is needed to achieve this. As a result, the subsequent orientation of the sample during the TEM diffraction-contrast imaging will be easier because our starting position in the TEM diffraction pattern will be closer to a zone axis.

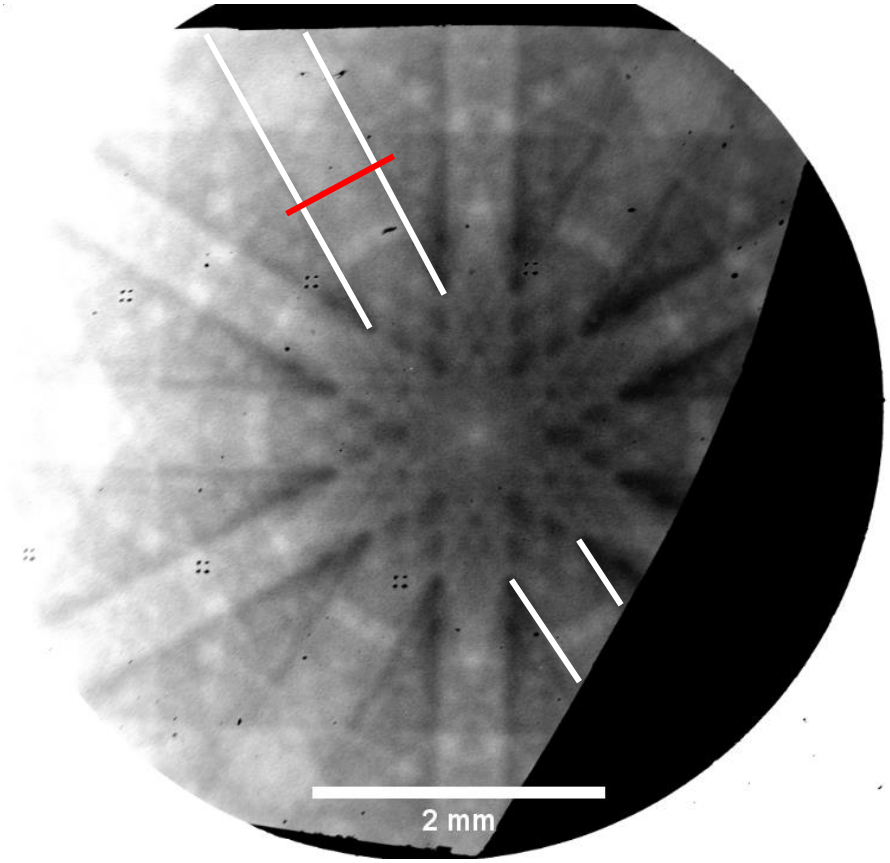

Fig. 2.13: *Wide-field* ECP used for the correct sample alignment in the subsequent lamella preparation. Desired orientation of the lamella (red line) is perpendicular to the highlighted band (white lines) as illustrated.

Concerning the lamella preparation, the sample holder for our microscope – FEI HELIOS – is shown in Fig. 2.14. The sample is attached by carbon tape to a pin stub, which in turn is fixed in the sample holder by a screw. Two pieces of copper foil tape are put on top of the sample to reduce charging inside the microscope, which could otherwise cause the sample to drift during the ion beam milling. Additionally, a copper grid is used, which is needed during the thinning of the lamella to a desired thickness and its subsequent transport to the TEM. This grid is held tight inside a row bar, which is also fixed to the sample holder by a screw. The sample holder, equipped with our sample and the Cu grid, is then transported through a loadlock into the microscope chamber, which is evacuated to allow the correct functioning of both the electron and the ion column.

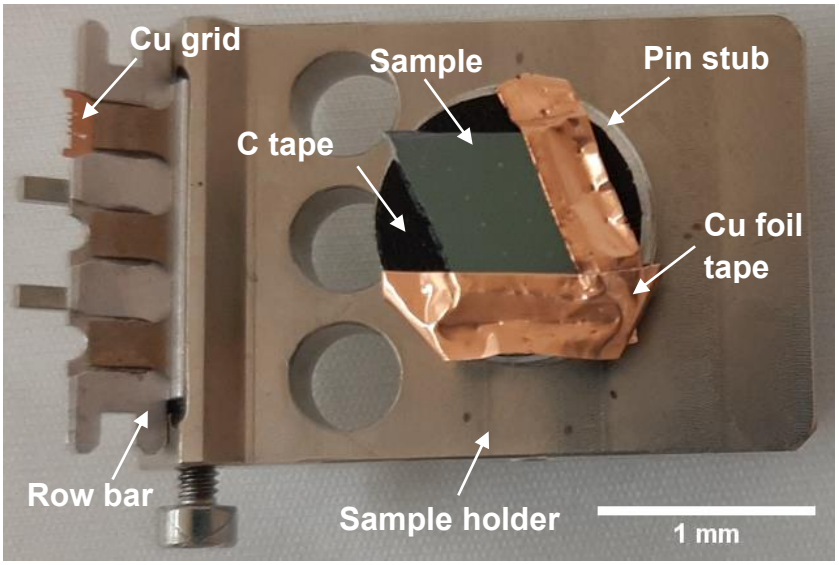

Fig. 2.14: Sample holder for lamella preparation in FEI HELIOS. On the right is our sample attached to a pin stub, fixed in the sample holder, by carbon tape. Copper foil tape is placed on top to reduce charging inside the microscope chamber. On the left, a copper grid, used for lamella thinning and transport, is held by a row bar.

The process always starts by establishing the ideal imaging parameters for both the electron and the ion beam. Firstly, the electron beam is focused on the surface of the sample to find the starting working distance, which is then, in our microscope, set to 4 mm. In our case, the sample is also rotated so that it is aligned as was described in Fig. 2.13. Secondly, the eucentric height should be determined. Eucentric height is the position of the stage in the *z*-axis, for which the view field does not change during tilting of the stage. Therefore, it is achieved accordingly, by centring on a reference spot on the sample, followed by tilting of the stage and adjusting the z-coordinate of the stage until the reference spot is centred on again. The stage is tilted in steps up to 52°, for which the ion beam is perpendicular to the sample surface as shown in Fig. 2.12. For this step, it is important to take care so that neither the sample nor the row bar collides with either of the columns. Thirdly, a coincidence point of the electron and the ion beam is found. This is done by finding a spot with the electron beam, followed by acquiring a single image with the ion beam. By utilizing the *beam shift* feature of the microscope, it is possible to move the ion beam to be centred on the same spot as the electron beam. This step is important so that it is later possible to observe the ion beam milling process with the electron beam. Moreover, there are two important things to mention here. First, since the focused ion beam is used for milling away material from the sample, it does exactly that – damages the sample. This is why only single images are done with the ion beam at a time (and the focusing of the ion beam is done away from the region of interest) – to prevent the deterioration of the sample surface due to the incident ions. This is especially important in our case when we are interested in a thin epitaxial layer right on the sample surface. Second, either the electron beam or the ion beam is used for creating an image on the computer screen, never both simultaneously, as was possible during ECCI with both BSE and SE signals. Although, it is, indeed, possible to mill with the ion beam while observing it with the electron beam (by using a much higher electron probe current to decrease interference from the ion beam).

As was mentioned above, the ion beam readily damages the sample

surface, especially for high beam currents used for milling of the sample. This is why it is necessary to protect the region, from which we want to make the lamella. To do this, firstly, electron beam induced deposition (EBID) of carbon, which is quite resistant to the Ga^+ ions from the ion source, is made at the chosen (15 × 2) μm^2 ROI, as shown in Fig. 2.15 a). Beam-induced deposition works by decomposing e.g. carbon precursor gas, which is introduced directly above the sample by a gas injection system (GIS). The beam of either electrons, or ions decomposes the gas into both volatile and non-volatile components. As a result of EBID, only carbon remains on the surface of the ROI as a few hundred nm thick layer. This layer is deposited to protect the surface during the next step of the process. Secondly, ion beam induced deposition (IBID) of a much thicker layer (few μm) of carbon is made on the same (15 × 2) μm^2 ROI as shown in Fig. 2.15 b). The IBID carbon layer is used as a protection of the lamella surface during the lift-out procedure and the final thinning of the lamella, both of which will be described in the next paragraphs.

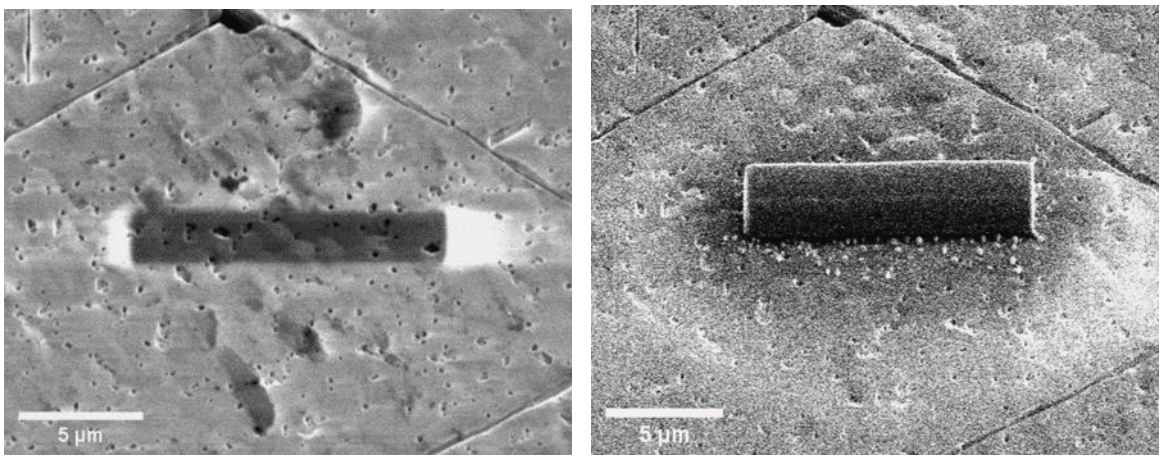

a) b)

Fig. 2.15: a) Electron beam induced deposition of carbon at our ROI and b) ion beam induced deposition of carbon on top of it.

Now that all the necessary steps mentioned above were taken care of, the process of extracting a lamella from our sample can begin. Firstly, rough milling of two trenches, one below and one above the ROI, is done with a Ga^+ ion beam of a high accelerating voltage (30 kV) and a high current (>9 nA). It is possible to observe the milling process by using about 3 times larger electron probe current than the ion beam current. The trenches are about 10 μm deep and they should be wider than the protected ROI on either side as shown in Fig. 2.16 a). Secondly, the ion beam current is lowered to ~2.5 nA to reduce the thickness of the ROI down to ~1 μm more precisely. This is done by tilting the sample by ±1.5° (to achieve grazing incidence angle for either trench) and by using a *'cleaning cross-section'* pattern, which extends slightly over both our ROI and the edge of a given trench. The result of this step is shown in Fig. 2.16 b). Thirdly, the stage is tilted back to 0° so that the ion beam sees the cross-section of the lamella and an undercut can be made. For this step, the ion beam current is lowered to 0.79 nA and about a 2 μm deep *U*-shaped pattern is milled under the lamella while keeping a single point of contact to the sample as shown in Fig. 2.17 a). Finally, the lift-out procedure is initiated to extract the lamella from the sample. This procedure begins by approaching the lamella with a nanomanipulator, which is inserted above the sample surface along with the GIS nozzle. The movement of the nanomanipulator

in the *x* and *y*-axis can be observed with the electron beam, while movement in the *z*-axis is seen with the ion beam. When the tip of the nanomanipulator is just touching the free edge of the lamella, IBID of tungsten is done to attach the lamella to the nanomanipulator. The ion beam current used for the IBID is set to not be too high, otherwise more material would be sputtered away than deposited. Once the deposition is complete, the single point of contact of the lamella to the sample can be milled away to free the lamella from the sample. The result of this procedure is shown in Fig. 2.17 b). At the end, the nanomanipulator is slowly moved away from the trench and then returned to its original position in the microscope along with the GIS nozzle.

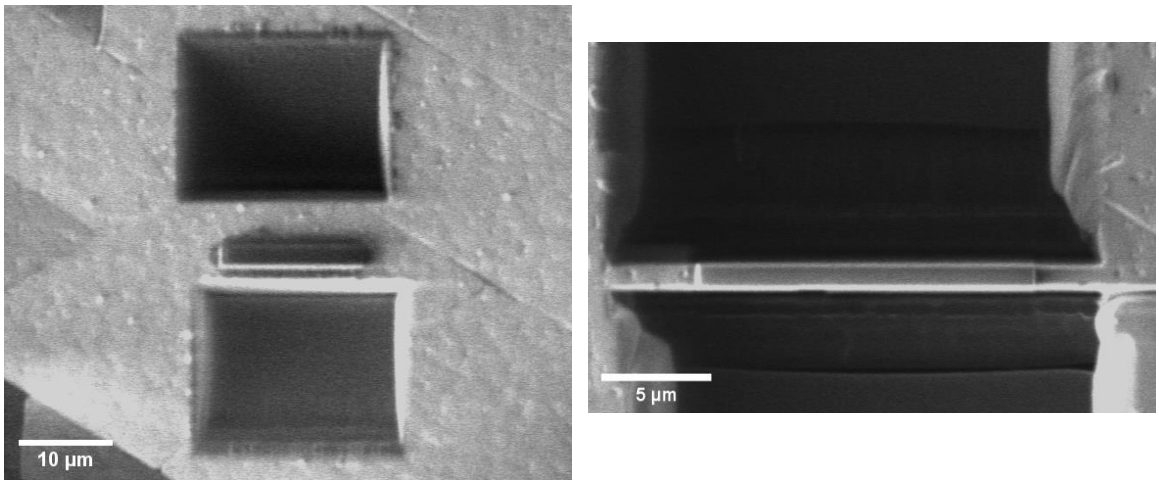

a) b)

Fig. 2.16: Ion beam micrograph of a) rough-milled trenches besides the ROI, and b) the final thickness of the lamella reduced down to ~1 µm.

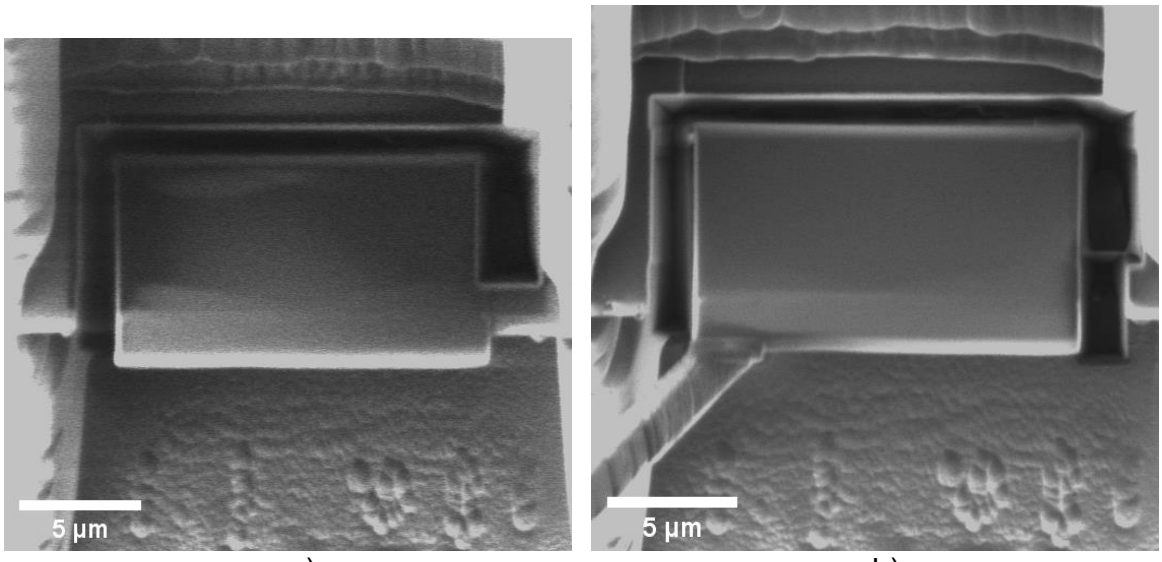

a) b)

Fig. 2.17: Ion beam micrograph of a) an undercut of the lamella with only a single point of contact to the sample kept on the right. b) Lift-out procedure, for which a nanomanipulator is attached to the lamella by IBID of tungsten followed by the removal of the final connection to the sample on the right side. The nanomanipulator can then transport the lamella to a Cu grid for further processing.

Now that we have extracted the lamella from the sample and attached it to a nanomanipulator, we can transport it to the copper grid. To do this, first, the Cu grid located on the row bar is moved under the electron beam column. Our used Cu grid has 4 'posts', to which the lamella can be attached. Therefore, we focus the electron beam on one of these posts and, again, establish the eucentric height and the coincidence point by a similar procedure as was mentioned above. Thus, we the stage is tilted to 52°, and now we insert the GIS nozzle and the nanomanipulator above the Cu grid. The nanomanipulator is moved so that the lamella gently touches the edge of the chosen post. Afterwards the IBID of W is initiated to attach the lamella to the post. Once it is finished, the nanomanipulator is cut-off from the other side of the lamella. Then, both the GIS nozzle and the nanomanipulator are returned to their default positions.

Now that the lamella is attached to the Cu grid, the final process – the thinning of the lamella so that it is electron transparent – can begin. First, the stage is tilted back to 0° so that the ion beam is incident on the face of the lamella with the deposited carbon layer. The starting thickness of our lamella is ~1 μm. The desired thickness, in our case, is somewhere from 150 nm up to 300 nm. The lamella is thinned in steps based on how thick it is. As a rule of thumb, the ion beam current in pA corresponds to the minimum thickness in nm, e.g. our first step will be to use an ion beam current of 790 pA to thin the lamella down to ~790 nm. To achieve this, we slightly tilt the lamella by ±1.2° so that the thinned side of the lamella is tilted more towards the ion beam and also so that the lamella is thinned evenly from both sides. Then, the *cleaning cross-section* is initiated for a certain time, which is the same for the second side of the lamella. After each step of thinning is done, the lamella can be tilted back to 0° to measure its thickness. Once the thickness reaches the minimum thickness for a given ion beam current, the ion beam current is reduced to the next available value. Then, the procedure is repeated for a smaller area further away from the attached edge of the lamella. Thickness of the lamella can be measured more accurately by the electron beam when the stage is tilted to 52°. Once again, it is also possible to observe the thinning process simultaneously by the electron beam, but usually a micrograph is taken only ever so often during it. If a lower thickness than ~200 nm is desired, lower acceleration voltages (5 kV and later even 2 kV, along with lower ion beam currents) are used. The ion beam micrograph, after the final thinning step was completed, is shown in Fig. 2.18. We achieved ~190 nm thickness of the lamella, which is ideal for our next experiments.

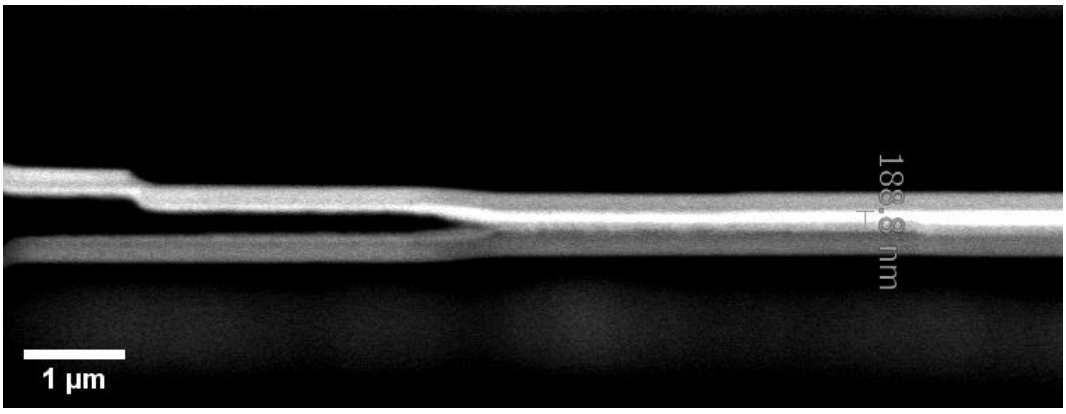

Fig. 2.18: Ion beam micrographs of the result of lamella thinning: ~190 nm lamella thickness was achieved.

2.5 TEM diffraction-contrast imaging

To reiterate, all micrographs in this section were taken, in my presence, by Ing. Eva Kolíbalová, Ph.D.

There are two main modes in any TEM: *image mode* and *diffraction mode*. *Image mode* is the standard mode for getting information about the sample in a relatively similar way as in optical microscopy. However, *diffraction mode* makes TEM especially useful for observing crystalline samples. *Diffraction mode* shows us a diffraction pattern (DP) based on the specific orientation of our sample. Each spot in the DP corresponds to a beam of electrons diffracted on a specific set of crystal planes, for which the (Bragg) diffraction condition is satisfied. The spots in the DPs (representing the different sets of crystal planes) can be identified and indexed either by a very skilled operator, or more easily by a computer program [59].

For TEM diffraction-contrast imaging, Kikuchi lines and maps such as the one shown in Fig. 2.19, are a vital tool for orientation and movement in the DP of crystalline samples. They are utilized to achieve the desired diffraction conditions needed for defect analysis [59]. These Kikuchi maps look quite similar to the channeling maps, part of one such map was seen in Fig. 1.11, obtainable by collecting many electron channeling patterns, taken for various combinations of tilt and rotation of the sample. Both of them can be indexed by some computer programs for subsequent quantitative analysis, e.g. finding out the Burgers vector of dislocations.

In our case, we focused mainly on the determination of the type of dislocations located under an etch pit. The process of doing this is explained in the next pages. All our TEM micrographs were taken at 300kV.

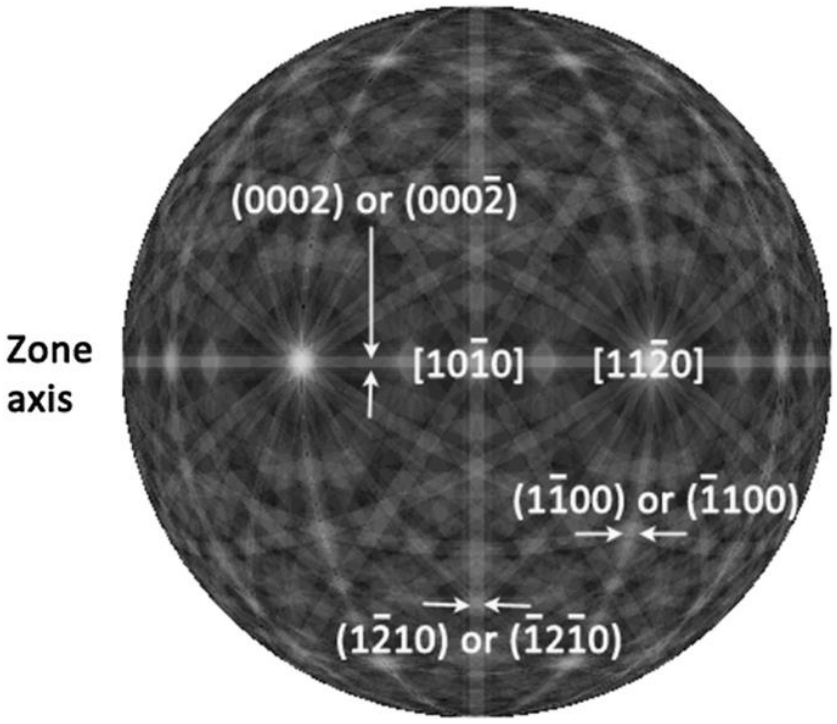

Fig. 2.19: Spherical Kikuchi map of GaN. From [60].

After doing all the necessary alignments of the electron beam, setting the excitations of the lenses, etc., we focused the beam on our ROI – etch pit in the GaN layer of the lamella. Then, we spread the beam to give nearly parallel illumination, and switched to the *diffraction mode* to visualize the resulting selected area diffraction pattern (SADP) [59]. Then, we oriented our sample so that the optical axis would be parallel to a zone axis, as seen in Fig. 2.20. This is done by following a Kikuchi line until you get to an intersection of many Kikuchi lines, which is, by definition, the zone axis. Movement in the SADP is done by utilizing a double-tilt specimen holder. This holder allows tilting of the sample in 2 axes – *α* and *β*. Utilizing *α*-tilt causes up-and-down movement while *β*-tilt results in a left-and-right movement in the SADP. Fortunately, due to the way our lamella was cut, which was described near the beginning of the previous section, we did not have to tilt the sample that much from its starting position.

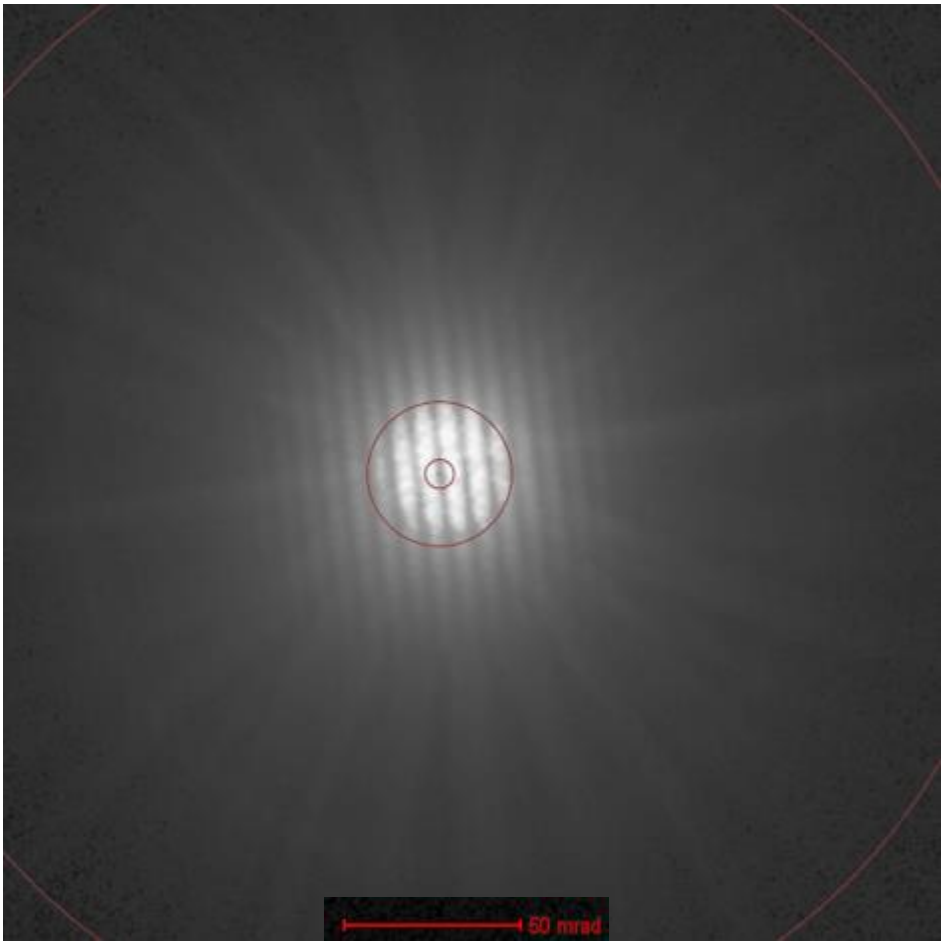

Fig. 2.20: Selected area diffraction pattern illustrating the alignment of the optical axis with a zone axis (intersection of the Kikuchi lines) of the lamella. The parts of the red circle along the edges are from the TEM software.

Then, we wanted to find out, which zone axis we are dealing with. This is done by increasing the camera length (the distance between the sample and the detector), which helps us to see a smaller part of the SADP. By comparing the observed arrangement of the spots in the SADP, seen in Fig. 2.21 a), with a simulated DP, seen in Fig. 2.21 b), we were able to identify the zone axis to be: $[10\bar{1}0]$. This is the same zone axis as was seen in Fig. 2.19. Therefore, we now

know exactly which diffraction conditions we can obtain by simply moving vertically or horizontally away from the zone axis, along the specific Kikuchi lines.

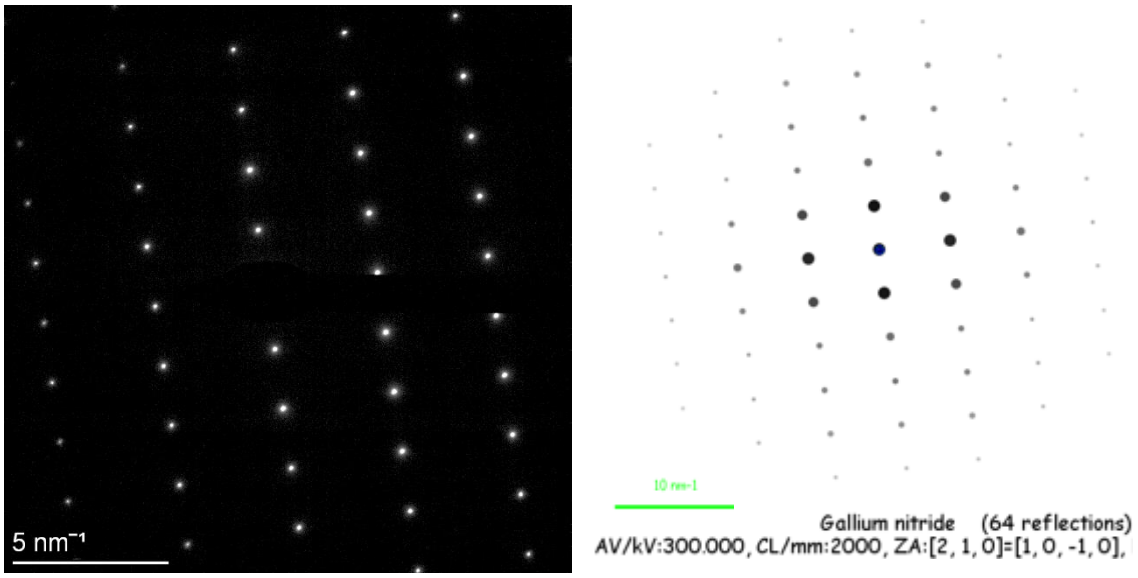

a) b)

Fig. 2.21: a) Observed selected area diffraction pattern from our GaN lamella, in which every spot corresponds to a satisfied (Bragg) diffraction condition for a certain set of crystal planes. The most intense zero order diffracted beam is not visible due to a beam blocker. b) Simulated diffraction pattern for GaN, which can be indexed by the simulating program. From this program, we established that this DP appearance, therefore also a), corresponds to a $[10\bar{1}0]$ zone axis (the same as is in the centre of Fig. 2.19.

Now that we have our optical axis aligned with a zone axis, we can take a micrograph with the beam near the zone axis. In this case, as the electron beam propagates through the lamella, it interacts with all kinds of crystal planes. Therefore, all types of dislocations are visible since a dislocation is visible precisely when a plane, which is distorted by the dislocation, diffracts the electrons that are used for imaging. And because no diffraction condition is isolated, there is a set of planes distorted by each type of dislocations. Such micrograph is seen in Fig. 2.22. On the very top, we see the deposited carbon layer. In the middle of the top part of the micrograph, we can see the etch pit. Underneath it are all the different types of dislocations, which cannot be characterized just from a single micrograph, but will be identified later. The dislocations do not appear very sharp partly due to the difficulties we encountered in finding the correct focus, since the lamella is relatively thick compared to the usual thicknesses. On the bottom of the micrograph, a small part of the AlN buffer layer is visible.

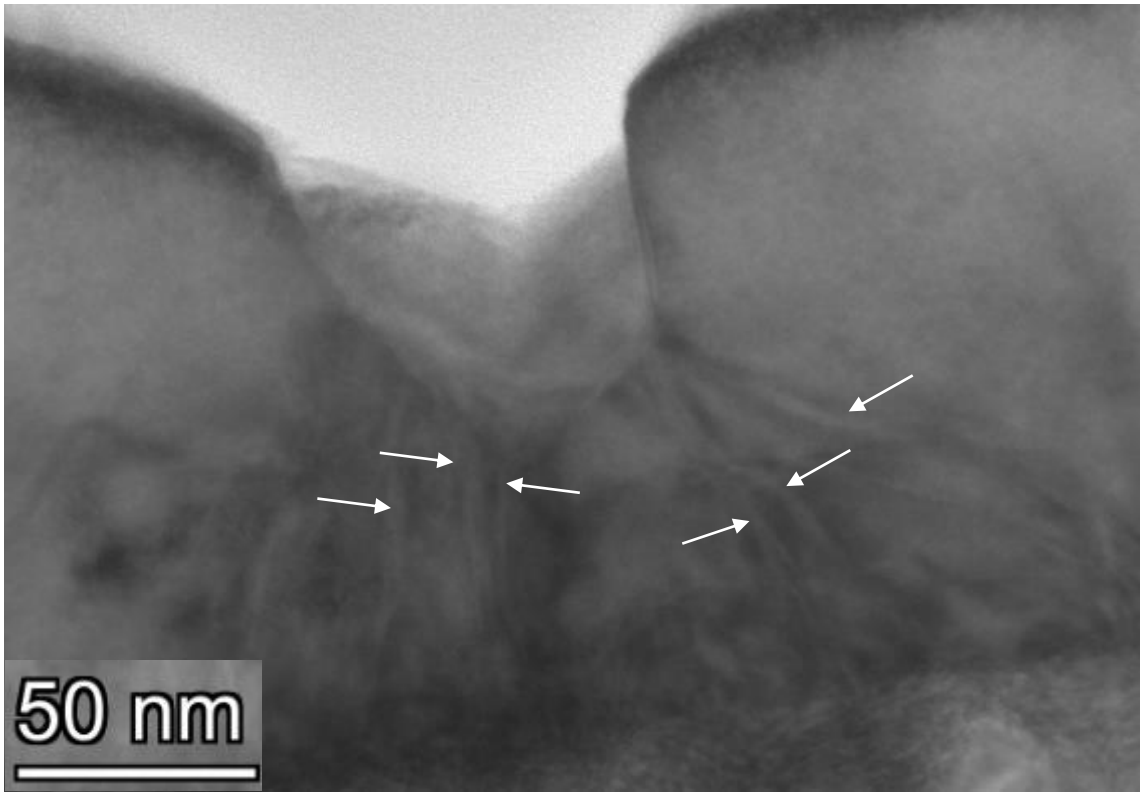

Fig. 2.22: TEM micrograph near the $[10\bar{1}0]$ zone axis. All types of dislocations, highlighted by arrows, are visible.

There can be a specific diffraction condition ***g***, which would make some type of dislocations turn invisible. This occurs depending on the satisfaction of the invisibility criteria mentioned in the 1.3.3 section of this thesis: $\boldsymbol{g} \cdot \boldsymbol{b} = 0$ and $\boldsymbol{g} \cdot (\boldsymbol{b} \times \boldsymbol{u}) = 0$, where ***g*** is the diffraction vector, ***b*** is the Burgers vector of the dislocation, and ***u*** is the dislocation line element. In our analysis, we focused on the first, most commonly used, invisibility criterion. Of course, it is possible that the first criterion is satisfied while the second one is not, resulting in residual contrast of some dislocations, but due to the already not ideal contrast of the dislocations, it is unlikely that we could see such dislocations in our micrographs.

To try to identify the dislocations in Fig. 2.22, we moved down along the vertical Kikuchi line $(\bar{1}2\bar{1}0)$, by tilting the sample along the *α*-axis, also seen in Fig. 2.19. For usual mass-thickness contrast, any diffracted beam can be used to form good quality micrographs. However, in TEM diffraction-contrast imaging, there is something known as a *'two-beam condition'*, which has to be utilized to get ideal diffraction contrast. In a *'two-beam condition'*, there is only one strong (high intensity) diffracted beam. Our setting of such a *'two-beam condition'* is seen in Fig. 2.23 a). Additionally, we tried to further improve the contrast of the following TEM micrographs, by inserting an objective aperture into the path of the electron beam to isolate only a few diffracted beams, as seen in Fig. 2.23 b).

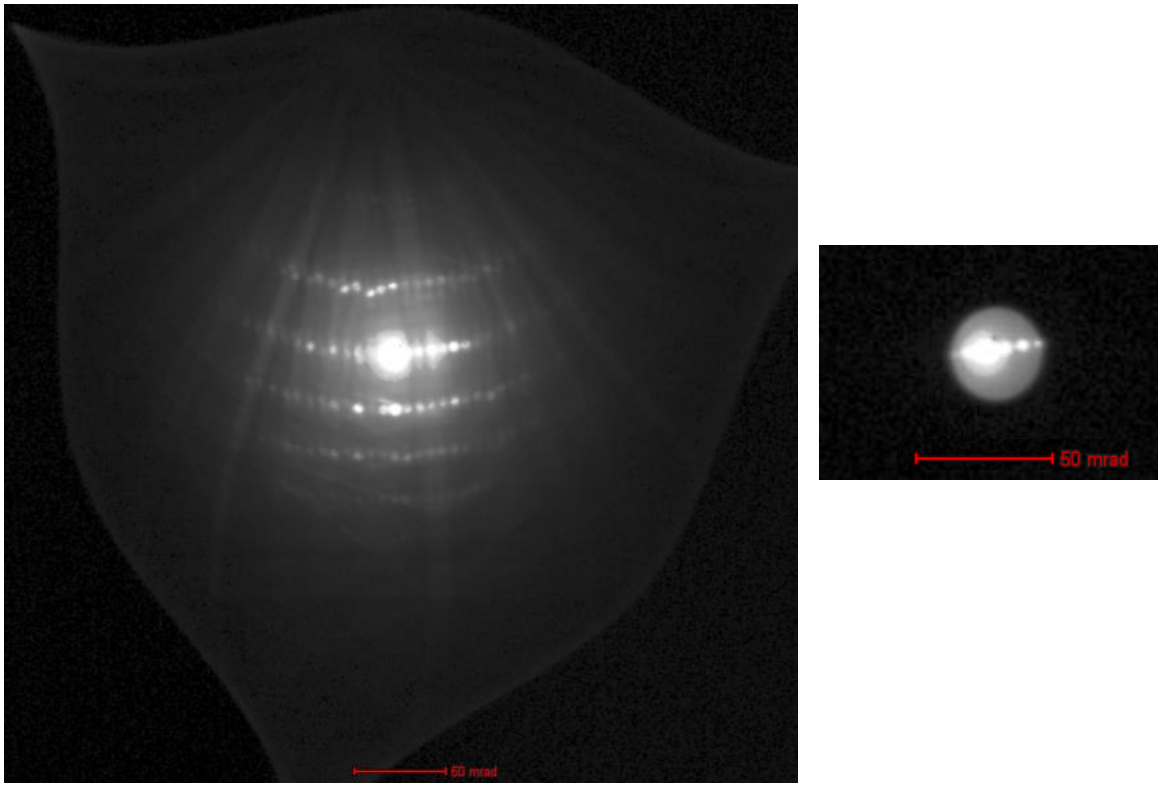

a) b)

Fig. 2.23: a) Position in the SADP after moving away from the zone axis, seen on top, down along the $(\bar{1}2\bar{1}0)$ Kikuchi line to set a two-beam diffraction condition. b) Isolation of a few diffracted beams around the most intense one to try to achieve better contrast in the following TEM micrograph.

The TEM micrograph taken under the first diffraction condition $\boldsymbol{g} = (\bar{1}2\bar{1}0)$ is seen in Fig. 2.24. To say something about what we see in this figure (and even about what we do NOT see), first, we need to recall the Burgers vector $\boldsymbol{b}$ of edge: $\frac{1}{3}\langle\bar{1}2\bar{1}0\rangle$, screw: $\langle 0001\rangle$, and mixed dislocations: $\frac{1}{3}\langle 11\bar{2}3\rangle$. By applying the invisibility criterion: $\boldsymbol{g} \cdot \boldsymbol{b} = 0$, we can simply calculate that, for $\boldsymbol{g} = (\bar{1}2\bar{1}0)$, screw dislocations will be invisible while edge and mixed dislocations will be visible. Therefore, the only dislocation that remained somewhat visible in Fig. 2.24, when compared to Fig. 2.22, is probably an edge dislocation (depends on if it is visible for the second diffraction condition, then it would most likely be a mixed dislocation).

To achieve the second *'two-beam condition'*, we returned back to the zone axis and from there utilized *β*-tilt to move away from the zone axis along the horizontal Kikuchi line, also seen in Fig. 2.19, to the left. The result is seen in Fig. 2.25 a), in which we see that there are multiple diffracted beams of the same highest intensity. Nonetheless, this can also be roughly considered a *'two-beam condition'*, especially when we, again, isolate the most intense diffracted beams as shown in Fig. 2.25 b).

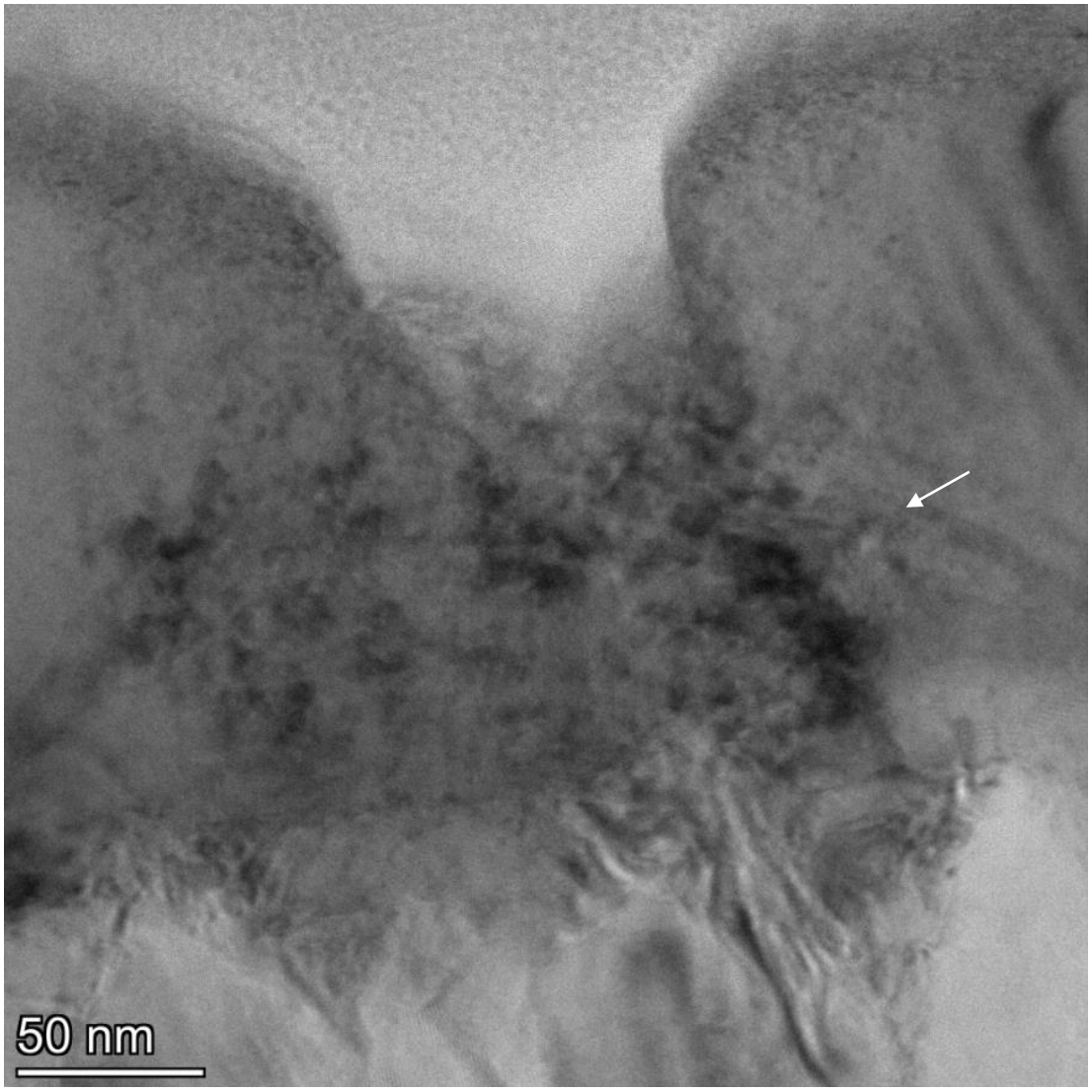

Fig. 2.24: Diffraction condition $\boldsymbol{g} = (\bar{1}2\bar{1}0)$, for which screw dislocations (with a Burgers vector $\boldsymbol{b} = \langle 0001 \rangle$) are invisible. Only edge/mixed dislocations can be visible. When compared to Fig. 2.22, only one dislocation, highlighted by an arrow, under the pit seems to be an edge dislocation. The very black parts around the pit are inadvertent beam damage caused by us during the setting of ideal imaging conditions.

The TEM micrograph taken under the second diffraction condition $\boldsymbol{g} = (0002)$ is seen in Fig. 2.26. By now applying the invisibility criterion: $\boldsymbol{g} \cdot \boldsymbol{b} = 0$, we can, calculate that, for this $\boldsymbol{g}$, the opposite to the first diffraction condition is true, namely that edge dislocations will be invisible while screw and mixed dislocations will be visible. By comparison of this figure with the TEM micrograph taken near the zone axis (Fig. 2.22), we see that the remaining five dislocations, which were invisible in Fig. 2.24, are screw dislocations. Finally, the sixth dislocation, that was visible in Fig. 2.24, but is now invisible is, most likely, indeed an edge dislocation.

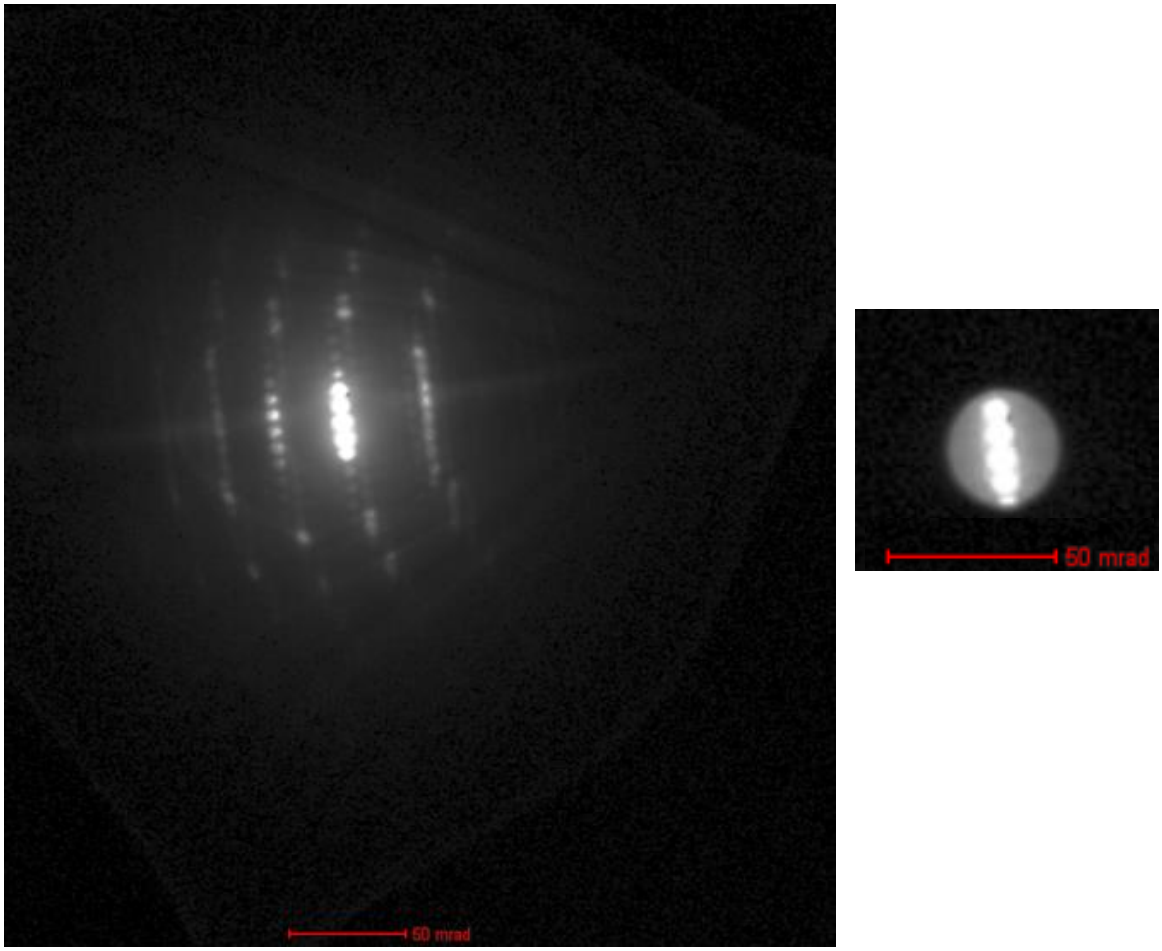

a) b)

Fig. 2.25: a) Position in the SADP after moving away from the zone axis, seen on the right, to the left along the (0002) Kikuchi line to set a two-beam diffraction condition. b) Isolation of the most intense diffracted beams to try to achieve better contrast in the following TEM micrograph.

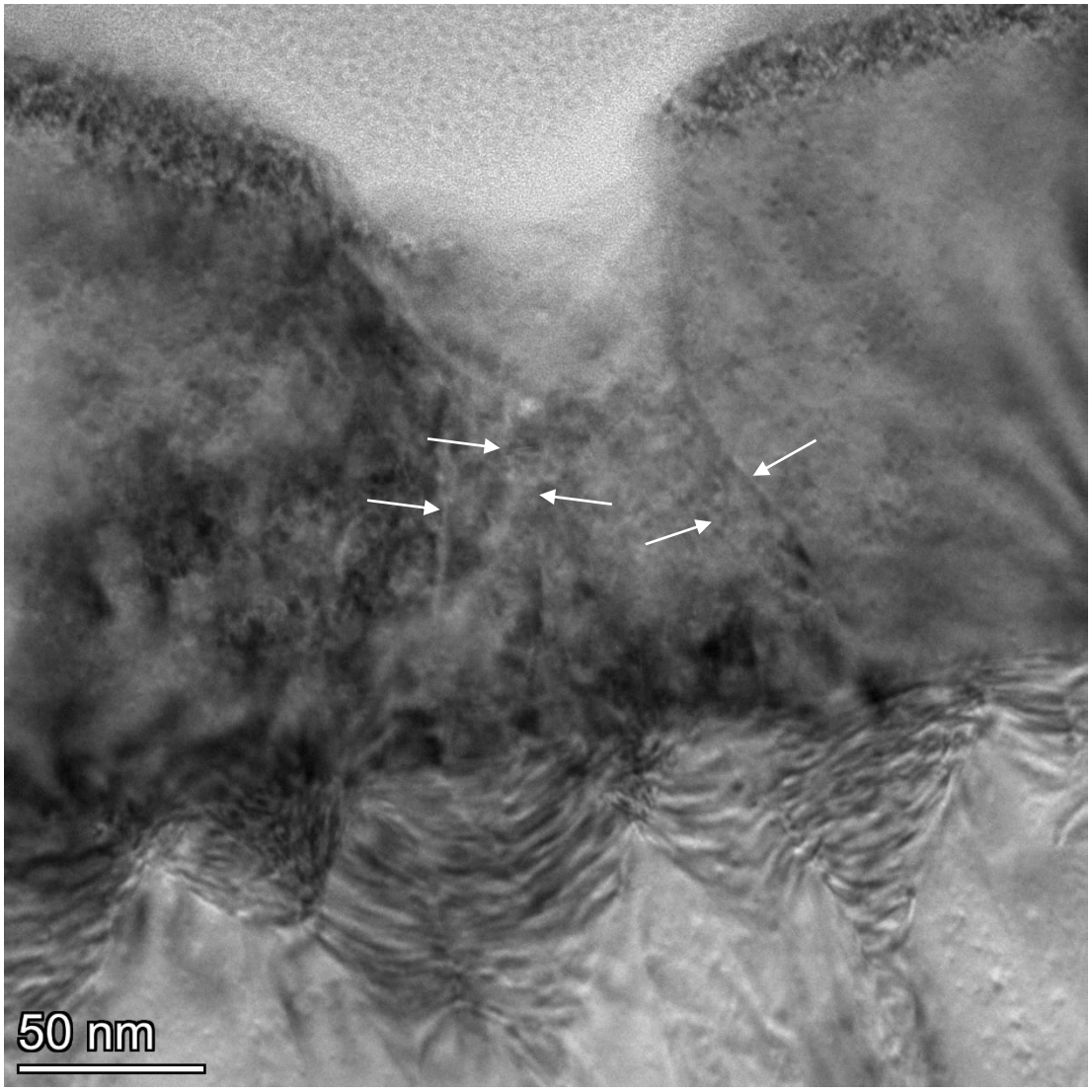

Fig. 2.26: Diffraction condition ***g*** = (0002), for which edge dislocations (with a Burgers vector $\frac{1}{3}\langle\bar{1}2\bar{1}0\rangle$) are invisible. Only screw/mixed dislocations, highlighted by arrows, are visible under the etch pit. The very black parts around the pit are inadvertent beam damage caused by us during the setting of ideal imaging conditions.

Conclusion

GaN is a very exciting material for the semiconductor industry, however, it also has some issues. GaN is grown mostly heteroepitaxially, and due to the large lattice and thermal expansion coefficient mismatch of GaN with its common substrates, a lot of strain is generated during its growth. The relaxation of this strain in GaN layers results in the creation of many threading dislocations, which can negatively impact the performance of devices made from GaN. Therefore, in this thesis, we decided to focus on the localisation and analysis of threading dislocations in GaN, which could provide the information needed to lower the threading dislocation density in GaN by improving its growing methods.

Threading dislocations are dislocations parallel to the *c*-axis in GaN that extend from the substrate interface throughout the epitaxial layer up to its surface. They can be studied by many different techniques, out of which we chose three complementary ones to focus on.

The first technique is electron channeling contrast imaging. It is a diffraction-based imaging technique in SEM. Its main advantage is that it is non-destructive and that it can study bulk specimens without much sample preparation. By using ECCI, we were able to differentiate screw/mixed TDs from edge TDs based on the size of the spots in the ECCI micrographs.

The second technique we used is defect-selective etching in KOH/NaOH eutectic mixture at high temperatures. Its advantage is that it can be used to study larger areas and more quickly than is the case for ECCI. Additionally, it does not require much apart from the chemicals themselves and a basic SEM. Therefore, this technique can be used by virtually any laboratory technician in their daily work. Etching of wurtzite GaN in molten bases results in the formation of hexagonal etch pits of different sizes, which should correspond to the different types of TDs. Using this technique, we were able to observe features of different sizes, as for ECCI, but we are unsure of their significance. To get the most out of this technique, further etching procedures focused on the determination of an ideal etching temperature and etching time, depending on the desired information, would have to be done.

The last technique we used is TEM diffraction-contrast imaging. The biggest advantage of TEM is that it can be used for quantitative analysis, e.g. finding the Burgers vector of TDs. However, this technique is the most operator dependent as it, first, requires the preparation of a thin lamella of good quality from the specimen. Second, it requires the ability to operate a TEM and the knowledge of diffraction conditions and invisibility criteria to characterize the TDs. Thus, to carry it out, we first prepared a lamella from our sample by FIB. The sample we used was etched in the eutectic mixture to try to gain some additional information of what type of TDs were located under an etch pit. We were successful in obtaining micrographs for two diffraction conditions, in addition to a micrograph near a zone axis. By utilizing invisibility criteria, we were able to isolate screw/mixed dislocations for one diffraction condition and edge dislocations for the other.

To conclude, we tried to explain the importance of studying threading dislocations in GaN. To study them, we focused on three techniques, each of which can be used independently to obtain similar information about TDs, but they can also be used complementarily. The choice between them depends on the abilities and requirements of the operator. Overall, we were successful in fulfilling the goals of this thesis and even tried something more with the inclusion of wet etching.

References

[1] MENEGHINI, Matteo. et al. GaN-based power devices: Physics, reliability, and perspectives. *J. Appl. Phys*. 2021, vol. 130, 18, 181101. ISSN 1089-7550. Available from: https://doi.org/10.1063/5.0061354

[2] MACHT, Lukasz. *Extended defects in GaN: Selective etching and optical properties*. Dissertation, Supervisor Prof. Dr. P.K. Larsen. Nijmegen, NL: Radboud University Nijmegen, 2005.

[3] KIM, S.T. et al. Preparation and properties of free-standing HVPE grown GaN substrates. *Journal of Crystal Growth*. 1998, vol. 194, 1, p. 37-42. ISSN 0022-0248. Available from: https://doi.org/10.1016/S0022-0248(98)00551-X

[4] VORONENKOV, Vladislav. et al. Reactor materials for high purity HVPE GaN growth: a thermodynamic analysis. In: *Journal of Physics Conference Series*. 1410. Saint Petersburg: IOP Publishing, 2019, 012004. ISSN 1742-6596. Available from: https://doi.org/10.1088/1742-6596/1410/1/012004.

[5] SETERA, Brett and CHRISTOU, Aristos. Threading dislocations in GaN high-voltage switches. *Microelectronics Reliability*. 2021, vol. 124, 114336. ISSN 0026-2714. Available from: https://doi.org/10.1016/j.microrel.2021.114336

[6] PICARD, Yoosuf N. et al. Dislocation Identification and Mapping in GaN by Electron Channeling Contrast Imaging. *Microscopy and Microanalysis*. 2012, vol. 18, S2, p. 718-719. ISSN 1431-9276. Available from: https://doi.org/10.1017/S1431927612005442

[7] NARITA, Tetsuo a KACHI, Tetsu. *Characterization of Defects and Deep Levels for GaN Power Devices*. Melville, New York: AIP Publishing, 2020. ISBN 978-0-7354-2269-8.

[8] HUANG, D. et al. Comparative study of Ga- and N-polar GaN films grown on sapphire substrates by molecular beam epitaxy. *J. Vac. Sci. Technol. B*. 2002, vol. 20, 6, p. 2256-2264. ISSN 2166-2754. Available from: https://doi.org/10.1116/1.1518969

[9] CARRASCON, Rosalia D. et al. Hot-Wall MOCVD for High-Quality Homoepitaxy of GaN: Understanding Nucleation and Design of Growth Strategies. *Crystal Growth & Design*. 2022, vol. 22, 12, p. 7021-7030. ISSN 1528-7505. Available from: https://doi.org/10.1021/acs.cgd.2c00683

[10] HULL, D. and BACON, D.J. Defects in Crystals. In: *Introduction to Dislocations*. Fifth Edition. Butterworth-Heinemann, 2011, p. 1-20. ISBN 978-0-08-096672-4.

[11] ANDERSON, Peter M.; HIRTH, John P. a LOTHE, Jens. *Theory of Dislocations*. 3rd ed. Cambridge: Cambridge University Press, 2017. ISBN 978-0-521-86436-7.

[12] VACEK, Petr. *Extended defects in Ga and Al nitrides*. Dissertation, Supervisor doc. Roman Gröger. Brno: CEITEC Brno University of Technology, 2021.

[13] REIMER, Ludwig. *Scanning Electron Microscopy: physics of image formation and microanalysis*. Second completely revised and updated edition. Springer Series in Optical Sciences, 45. Berlin: Springer, 1998. ISBN 978-3-642-08372-3.

[14] EGERTON, Ray F. The Scanning Electron Microscope. In: EGERTON, Ray F. *Physical Principles of Electron Microscopy*. New York: Springer, 2005, p. 125-153. ISBN 978-0387-25800-3.

[15] GOLDSTEIN, Joseph I.; NEWBURY, Dale E. and MICHAEL, Joseph R. *Scanning Electron Microscopy and X-Ray Microanalysis*. 4th ed. New York, NY: Springer, 2018. ISBN 978-1-4939-6674-5.

[16] DEITZ, Julia I. et al. Electron Channeling Contrast Imaging for Rapid III-V Heteroepitaxial Characterization. *J. Vis. Exp*. 2015, 101, e52745. ISSN 1940-087X. Available from: https://dx.doi.org/10.3791/52745

[17] COATES, D. G. Kikuchi-like Reflection Patterns obtained with the Scanning Electron Microscope. *Philosophical Magazine*. 1967, vol. 16, 144, p. 1179-1184. ISSN 0031-8086. Available from: https://doi.org/10.1080/14786436708229968

[18] BOOKER, G. R. et al. Some comments on the interpretation of the 'kikuchi-like reflection patterns' observed by scanning electron microscopy. *Philosophical Magazine*. 1967, vol. 16, 144, p. 1185-1191. ISSN 0031-8086. Available from: https://doi.org/10.1080/14786436708229969

[19] PICARD, Yoosuf N. A Review of Electron Channeling Contrast Imaging for Non-Destructive Defect Analysis of Crystalline Solids. *Microscopy and Microanalysis*. 2018, vol. 24, S1, p. 630-631. ISSN 1435-8115. Available from: https://doi.org/10.1017/S1431927618003641

[20] SIMKIN, B. A. and CRIMP, M. A. An experimentally convenient configuration for electron channeling contrast imaging. *Ultramicroscopy*. 1999, vol. 77, 1-2, p. 65-75. ISSN 0304-3991. Available from: https://doi.org/10.1016/S0304-3991(99)00009-1

[21] KAMALADASA, Ranga J. and PICARD, Yoosuf N. Basic Principles and Application of Electron Channeling in a Scanning Electron Microscope for Dislocation Analysis. In: *Microscopy: Science, Technology, Applications and Education*. 3. Badajoz, Spain: Formatex, 2010, p. 1583-1590. ISBN 978-84-614-6191-2.

[22] HAN, Han. et al. Crystalline defect analysis in epitaxial $Si_{0.7}Ge_{0.3}$ layer using site-specific ECCI-STEM. *Micron*. 2021, vol. 150, 103123. ISSN 0968-4328. Available from: https://doi.org/10.1016/j.micron.2021.103123

[23] CZERNUSZKA, J.T. et al. Electron Channelling Contrast Imaging (ECCI) of Dislocations in Bulk Specimens. *MRS Proceedings*. 1990, vol. 209, p. 289-292. ISSN 1946-4274. Available from: https://doi.org/10.1557/PROC-209-289

[24] KAMALADASA, Ranga J. et al. Identifying threading dislocations in GaN films and substrates by electron channelling. *Journal of Microscopy*. 2011, vol. 244, 3, p. 311-319. ISSN 0022-2720. Available from: https://doi.org/10.1111/j.1365-2818.2011.03538.x

[25] JOY, David C.; NEWBURY, Dale E. and DAVIDSON, David L. Electron channeling patterns in the scanning electron microscope. *J. Appl. Phys*. 1982, vol. 53, 8, p. R81-R122. ISSN 0021-8979. Available from: https://doi.org/10.1063/1.331668

[26] *Electron channelling contrast imaging (ECCI)*. Online. Semiconductor Spectroscopy and Devices. c2020. Available from: https://ssd.phys.strath.ac.uk/techniques/scanning-electron-microscopy/electron-channelling-contrast-imaging-ecci/. [cit. 2024-05-07].

[27] DLUHOŠ, Jiří; SEDLÁČEK, Libor and MAN, Jiří. Application of electron channeling contrast imaging in study of polycrystalline materials and visualization of crystal lattice defects. In: *Conference proceedings: 21st International Conference on Metallurgy and Materials METAL 2012*. Ostrava: Tanger, 2012, p. 216-220. ISBN 978-80-87294-29-1. ISSN 2694-9296. Available from: https://www.confer.cz/metal/2012

[28] GUYON, Julien. et al. Sub-micron resolution selected area electron channeling patterns. *Ultramicroscopy*. 2015, vol. 149, p. 34-44. ISSN 0304-3991. Available from: https://doi.org/10.1016/j.ultramic.2014.11.004

[29] WILKINSON, Angus J. and HIRSCH, Peter B. Electron diffraction based techniques in scanning electron microscopy of bulk materials. *Micron*. 1997, vol. 28, 4, p. 279-308. ISSN 0968-4328. Available from: https://doi.org/10.1016/S0968-4328(97)00032-2

[30] CRIMP, Martin A. Scanning electron microscopy imaging of dislocations in bulk materials, using electron channeling contrast. *Microscopy research and technique*. 2006, vol. 69, p. 374-381. ISSN 1097-0029. Available from: https://doi.org/10.1002/jemt.20293

[31] STICKLER, Christian. SEM-ECC imaging and SAC-Patterns - Procedures for the nondestructive characterization of microstructures and for revealing the global dislocation arrangement. *Practical Metallography*. 2001, vol. 38, 10, p. 566-590. ISSN 2195-8599. Available from: https://doi.org/10.1515/pm-2001-381004m

[32] NARESH-KUMAR, G. et al. Electron channeling contrast imaging studies of nonpolar nitrides using a scanning electron microscope. *Applied Physics Letters*. 2013, vol. 102, 14, 142103. ISSN 0003-6951. Available from: https://doi.org/10.1063/1.4801469

[33] NARESH-KUMAR, G. et al. Rapid Nondestructive Analysis of Threading Dislocations in Wurtzite Materials Using the Scanning Electron Microscope. *Physical Review Letters*. 2012, vol. 108, 13, 135503. ISSN 0031-9007. Available from: https://doi.org/10.1103/PhysRevLett.108.135503

[34] CRIMP, M. A.; SIMKIN, B. A. and NG, B. C. Demonstration of the g · b x u = 0 edge dislocation invisibility criterion for electron channelling contrast imaging. *Philosophical Magazine Letters*. 2001, vol. 81, 12, p. 833-837. ISSN 0950-0839. Available from: https://doi.org/10.1080/09500830110088755

[35] MORAM, M. A. et al. On the origin of threading dislocations in GaN films. *Journal of Applied Physics*. 2009, vol. 106, 7, 073513. ISSN 0021-8979. Available from: https://doi.org/10.1063/1.3225920

[36] DATTA, R. et al. Growth and characterisation of GaN with reduced dislocation density. *Superlattices and Microstructures*. 2004, vol. 36, 4, p. 393-401. ISSN 0749-6036. Available from: https://doi.org/10.1016/j.spmi.2004.09.003

[37] PICARD, Yoosuf N. et al. Resolving the Burgers vector for individual GaN dislocations by electron channeling contrast imaging. *Scripta Materialia*. 2009, vol. 61, 8, p. 773-776. ISSN 1359-6462. Available from: https://doi.org/10.1016/j.scriptamat.2009.06.021

[38] ZHUANG, D. and EDGAR, J.H. Wet etching of GaN, AlN, and SiC: a review. *Materials Science and Engineering: R: Reports*. 2005, vol. 48, 1, p. 1-46. ISSN 0927-796X. Available from: https://doi.org/10.1016/j.mser.2004.11.002

[39] PEARTON, S. J. et al. GaN: Processing, defects, and devices. *Journal of Applied Physics*. 1999, vol. 86, 1, p. 1-78. ISSN 0021-8979. Available from: https://doi.org/10.1063/1.371145

[40] SHINTANI, Akira and MINAGAWA, Shigekazu. Etching of GaN Using Phosphoric Acid. *Journal of The Electrochemical Society*. 1976, vol. 123, 5, p. 706-713. ISSN 1945-7111. Available from: https://dx.doi.org/10.1149/1.2132914

[41] STOCKER, D. A.; SCHUBERT, E. F. and REDWING, J. M. Crystallographic wet chemical etching of GaN. *Applied Physics Letters*. 1998, vol. 73, 18, p. 2654-2656. ISSN 0003-6951. Available from: https://doi.org/10.1063/1.122543

[42] KOZAWA, Takahiro. et al. Dislocation Etch Pits in GaN Epitaxial Layers Grown on Sapphire Substrates. *Journal of The Electrochemical Society*. 1996, vol. 143, 1, p. L17-L19. ISSN 1945-7111. Available from: https://dx.doi.org/10.1149/1.1836377

[43] ROUVIERE, J. L. et al. Polarity determination for GaN films grown on (0001) sapphire and high-pressure-grown GaN single crystals. *Applied Physics Letters*. 1998, vol. 73, 5, p. 668-670. ISSN 0003-6951. Available from: https://doi.org/10.1063/1.121942

[44] YOUTSEY, C.; ROMANO, L. T. and ADESIDA, I. Gallium nitride whiskers formed by selective photoenhanced wet etching of dislocations. *Applied Physics Letters*. 1998, vol. 73, 6, p. 797-799. ISSN 0003-6951. Available from: https://doi.org/10.1063/1.122005

[45] VISCONTI, P. et al. Investigation of defects and surface polarity in GaN using hot wet etching together with microscopy and diffraction techniques. *Materials Science and Engineering B*. 2002, vol. 93, 1-3, p. 229-233. ISSN 1873-4944. Available from: https://doi.org/10.1016/S0921-5107(02)00011-9

[46] VISCONTI, P. et al. Investigation of Defects and Polarity in GaN Using Hot Wet Etching, Atomic Force and Transmission Electron Microscopy and Convergent Beam Electron Diffraction. *Physica status solidi (b)*. 2001, vol. 228, 2, p. 513-517.

ISSN 0370-1972. Available from: https://doi.org/10.1002/1521-3951(200111)228:2<513::AID-PSSB513>3.0.CO;2-Y

[47] ROSNER, S. J. et al. Correlation of cathodoluminescence inhomogeneity with microstructural defects in epitaxial GaN grown by metalorganic chemical-vapor deposition. *Applied Physics Letters*. 1997, vol. 70, 4, p. 420-422. ISSN 0003-6951. Available from: https://doi.org/10.1063/1.118322

[48] VISCONTI, P. et al. Dislocation density in GaN determined by photoelectrochemical and hot-wet etching. *Applied Physics Letters*. 2000, vol. 77, 22, p. 3532-3534. ISSN 0003-6951. Available from: https://doi.org/10.1063/1.1329330

[49] CHEN, J. et al. Measurement of threading dislocation densities in GaN by wet chemical etching. *Semiconductor Science and Technology*. 2006, vol. 21, 9, p. 1229-1235. ISSN 0268-1242. Available from: https://dx.doi.org/10.1088/0268-1242/21/9/004

[50] WEYHER, J.L. et al. Recent advances in defect-selective etching of GaN. *Journal of Crystal Growth*. 2000, vol. 210, 1, p. 151-156. ISSN 0022-0248. Available from: https://doi.org/10.1016/S0022-0248(99)00669-7

[51] YOUTSEY, C. et al. Smooth n-type GaN surfaces by photoenhanced wet etching. *Applied Physics Letters*. 1998, vol. 72, 5, p. 560-562. ISSN 0003-6951. Available from: https://doi.org/10.1063/1.120758

[52] IVANTSOV, Vladimir and VOLKOVA, Anna. A Comparative Study of Dislocations in HVPE GaN Layers by High-Resolution X-Ray Diffraction and Selective Wet Etching. *ISRN Condensed Matter Physics*. 2012, vol. 2012, 3, 184023. ISSN 2356-7872. Available from: https://doi.org/10.5402/2012/184023

[53] WEYHER, J.L. et al. Orthodox etching of HVPE-grown GaN. *Journal of Crystal Growth*. 2007, vol. 305, 2, p. 384-392. ISSN 0022-0248. Available from: https://doi.org/10.1016/j.jcrysgro.2007.03.030

[54] WEYHER, J. L. and MACHT, L. Defects in wide band-gap semiconductors: selective etching and calibration by complementary methods. *Eur. Phys. J. Appl. Phys*. 2004, vol. 27, 1-3, p. 37-41. ISSN 1286-0050. Available from: https://doi.org/10.1051/epjap:2004092

[55] HONG, S. K. et al. Origin of hexagonal-shaped etch pits formed in (0001) GaN films. *Applied Physics Letters*. 2000, vol. 77, 1, p. 82-84. ISSN 0003-6951. Available from: https://doi.org/10.1063/1.126884

[56] DESSUREAULT, Y; SANGSTER, J and PELTON, AD. Evaluation critique des données thermodynamiques et des diagrammes de phases des systèmes AOH-AX, ANO3-AX, ANO3-BNO3, AOH-BOH où A, B = Li, Na, K et X = Cl, F, NO3, OH. *J. Chim. Phys*. 1990, vol. 87, p. 407-453. ISSN 0021-7689. Available from: https://doi.org/10.1051/jcp/1990870407

[57] MICHAŁOWSKI, Paweł P. et al. 3D Depth Profile Reconstruction of Segregated Impurities using Secondary Ion Mass Spectrometry. *Journal of*

Visualized Experiments. 2020, 158, e61065. ISSN 1940-087X. Available from: https://doi.org/10.3791/61065

[58] VAŘEKA, Karel. *Correlative tomography*. Master's thesis, Supervisor Ing. Petr Bábor, Ph.D. Brno: Brno University of Technology, Faculty of Mechanical Engineering, Institute of Physical Engineering, 2021.

[59] WILLIAMS, David B. and CARTER, C. Barry. *Transmission Electron Microscopy: A Textbook for Materials Science*. 2nd ed. New York, NY: Springer, 2009. ISBN 978-0-387-76500-6.

[60] SUN, Cheng. et al. Analysis of crystal defects by scanning transmission electron microscopy (STEM) in a modern scanning electron microscope. *Advanced Structural and Chemical Imaging*. 2019, vol. 5, 1, p. 3. ISSN 2198-0926. Available from: https://doi.org/10.1186/s40679-019-0065-1

List of abbreviations

0D	zero-dimensional
1D	one-dimensional
2D	two-dimensional
3D	three-dimensional
AE	Auger electron
AFM	atomic force microscopy
BSE	back-scattered electron
BUT	Brno University of Technology
CEITEC	Central European Institute of Technology
DD	dislocation density
DP	diffraction pattern
EBID	electron beam induced deposition
EBSD	electron backscatter diffraction
ECCI	electron channeling contrast imaging
ECP	electron channeling pattern
EPD	etch pit density
ETD	Everhart-Thornley detector
FEG	field emission gun
FIB	focused ion beam
FME	Faculty of Mechanical Engineering
FoV	field of view
GIS	gas injection system
HCP	hexagonal close-packed
HV	high voltage
HVPE	hydride vapor phase epitaxy
IBID	ion beam induced deposition
ID	inversion domain
IPE	Institute of Physical Engineering
LED	light-emitting diode
MBE	molecular beam epitaxy
MOCVD	metalorganic chemical vapor deposition
PE	primary electron
PEC	photoelectrochemical
PMT	photomultiplier tube
ROI	region of interest
SACP	selected area channeling pattern
SADP	selected area diffraction pattern
SE	secondary electron
SEM	scanning electron microscope(y)
SNR	signal-to-noise ratio
TEM	transmission electron microscope(y)
TFS	Thermo Fisher Scientific
TD	threading dislocation
TDD	threading dislocation density
UHV	ultra-high vacuum
UV	ultraviolet
WD	working distance